공학박사 학위논문

High-Performance Solar Cells via Compositional and Surface Defect Engineering of Hybrid Organic-Inorganic Perovskites

조성 및 표면 제어를 통한 유·무기 복합 페로브스카이트 태양전지 성능향상에 관한 연구

2019년 2월

서울대학교 대학원
재료공학부
황 태 현

Ph.D. Thesis

High-Performance Solar Cells via Compositional and Surface Defect Engineering of Hybrid Organic-Inorganic Perovskites

Taehyun Hwang

February 2019

Department of Materials Science and Engineering

Seoul National University

Abstract

Despite the upsurge of global energy demand, energy supply relies on fossil fuels, petroleum, and nuclear fusion energy. It brings the secondary issues of greenhouse gas emission and radioactive wastes with the concerns on the climate change and global warming. Therefore, the exploration of alternative energy sources for the electricity generation is inevitable for the next generation. Among many renewable energy resources, solar energy presents huge benefits and the installed capacity has been scaled up, designing the path toward the terawatt-scale photovoltaics. Photovoltaic device is the electrical device that directly converts the solar energy into electricity. Maximum utilization of solar irradiance is essential to meet the energy demand for human activity. It requires the realization of efficient and stable photovoltaic device through the low cost and commercially practical fabrication using the earth abundant materials.

Solar cell using thin-film semiconductor of superior optoelectronic property has been vastly studied, and the next-generation photovoltaics utilizing multiple carrier generation is further explored. Among many candidates for photovoltaic material, class of hybrid organic-inorganic metal halide perovskite is demonstrated to be promising due to its inherent excellent properties suited for the photon absorption and charge generation without significant recombination. The achievement of high photon-to-current conversion efficiency provides the viability for the practical operation in real life as well as the feasibility of applications into various functional devices beyond photovoltaics.

In this thesis, methylammonium (MA)- and formamidinium (FA)-based lead halide perovskites and their solar cells are studied with the investigation of characteristic features enabling for the efficient and stable photovoltaic performance. Considering the use of submicrometer-thick perovskite film, comprehensive analyses on the microscopic to nanoscopic features for the microstructural and defect properties are performed. Compositional tuning of hybrid perovskite enables for the understanding on the bulk

properties and the post-deposition treatment allows to characterize the impacts of surface and interfacial properties on the photovoltaic performance. It is aimed to find the critical factors which have direct impacts on perovskite solar cell as well as to provide the perspective that might lead to the further performance enhancement.

In chapter 1, basic working principle of solar cell is introduced to figure out the potential causes that impose the limitation on the performance improvement. The fundamental but essential features enabled for the conspicuous growth of perovskite solar cells are briefly overviewed to establish the strategies and to resolve the bottlenecks limiting the performance.

In chapter 2, the role of ionic defects is investigated through the compositional and thermal-annealing controls of perovskites. Assumed that the microstructural differences to have distinctive effects on the cell performance, $MAPbI_3$, $(FA_{0.83}MA_{0.17})Pb(I_{0.83}Br_{0.17})_3$, and $(Cs_{0.10}FA_{0.75}MA_{0.15})Pb(I_{0.85}Br_{0.15})_3$ perovskites (abbreviated as MA, FAMA, and CsFAMA, respectively) are systematically compared. Micro-/nanoscopic features are comprehensively analysed to unravel the origins that are directly correlated to the cell performance. It is revealed that CsFAMA has lower number of electronic traps compared to MA and FAMA. In addition, the change of open-circuit voltage of solar cell shows the correlation to the variation of trap state during the stability test. Even though the similar degradation rate of power-conversion efficiency is commonly observed in all perovskites, FAMA and CsFAMA cells distinctively exhibit negligible change of open-circuit voltage, and these cells simultaneously exhibit the trap-state shift toward the bandedge. It is concluded that triple-cation perovskite has a merit as the long-term stable photovoltaics, which is supported by its characteristic electronic trap states.

In chapter 3, post-deposition treatment is further utilized for the passivation of surface defect and high-quality interface of perovskite. Motivated from various significant impacts of point-defect and electronic-trap on the cell performance, shallow and deep electronic traps enabling for the performance improvement are investigated with the surface properties. Research on the benign and potential detrimental effects by the

post-deposition treatment is expected to inspire the strategy for the further performance enhancement. The MACl solution is exploited since the chlorine is vastly debated regarding its roles, thereby the post-deposition treatment can rationally exclude the Cl effect on microstructural evolution of perovskite grains. Photovoltaic performance demonstrates that it is improved in $(Cs_{0.05}FA_{0.79}MA_{0.16})Pb(I_{0.84}Br_{0.16})_3$, while $MAPbI_3$ cells suffer from the deterioration. Double-sided effects of MACl treatment are supposed on the trap formation and passivation, and the characterization of shallow/deep electronic traps present the evidence for the opposite result depending on the perovskite composition. It is revealed that additional deep-trap formation limits the improvement in $MAPbI_3$, while the reduction of traps result in the enhancement for $(Cs_{0.05}FA_{0.79}MA_{0.16})Pb(I_{0.84}Br_{0.16})_3$. From the improved resistance to chemical reaction and defect-tolerance property, triple-cation perovskites provide the viability for the further performance enhancement.

Keywords: solar cells, hybrid organic-inorganic lead halide perovskites, compositional engineering, $CH_3NH_3PbI_3$, Cs-substituted triple-cation perovskites, post-deposition treatment, CH_3NH_3Cl, defect passivation, electronic trap, 1/*f* electrical noise, capacitance, recombination

Student Number: 2012-23934

Table of Contents

List of Figures

Chapter 1.

Chapter 2.

Chapter 3.

List of Tables

Chapter 2.

Chapter 3.

Chapter 1. Overview of Perovskite Solar Cells

1.1. Introduction to Solar Cells

The operational principle of solar cell is based on the photovoltaic effect. The conversion of photon into electrical charges results in the conversion of solar energy into electricity. Power-conversion efficiency (η) is defined as the ratio between the maximum power output of solar cell and the incident power of solar energy. It is determined by three quantities, which are short-circuit current density (J_{sc}), open-circuit voltage (V_{oc}), and fill factor (FF). J_{sc} is a measure of a charge generation and the subsequent transport to the external circuit. For the high J_{sc}, material should satisfy the balance between the extinction of incident photon and the concomitant photocarrier extraction, and the material of low bandgap energy has a merit by reducing the spectrum loss below the bandgap energy. For the high V_{oc}, wide bandgap material is required to obtain the high quasi-fermi level splitting between e^- and h^+, which inevitably leads to the photocurrent loss by the forbidden excitation in bandgap. Accordingly, the optimal bandgap between 1.2 and 1.3 eV is expected to have η above 30% in a single-junction solar cell. Many semiconductors are promising and approach the efficiency limit that is predicted from the detailed balance between photon absorption (e^- and h^+ generation) and emission (recombination) [1].

Energy loss mechanisms in solar cell are shown in Fig. 1-1 [1]. Recombination besides the one in an ideal *pn* diode cause the additional energy loss, hampering the realization of efficiency limit. The real photovoltage and photocurrent are less than the expected values, which are predicted from the assumptions that the recombination is via the radiative emission (Shockley-Queisser limit) [2]. Entropy terms contribute to the photovoltage loss that V_{oc} of less than 0.3-0.4V compared to the bandgap energy is obtained

for the high-quality materials such as GaAs, crystalline Si, and hybrid perovskite. The radiative recombination efficiency is a critical factor, and high luminescence accompanies the increase of η of solar cell in general as shown in Fig. 1-2 [3]. Therefore, the strategy for enhancing the luminescence efficiency could be applied in a similar manner for improving η of solar cells.

Reduction of additional recombination paths also leads to the improvement of *FF*, which is defined as the ratio of the maximum power of the solar cell to the product of J_{sc} and V_{oc}. To improve *FF*, series resistance should be minimized while the shunt resistance must be maximized, which can be inferred from the following ideal one-diode equation:

$$J(V) = J_{ph} - J_0 exp\left[\frac{e(V + J(V)R_s}{nk_BT}\right] - \frac{V + J(V)R_s}{R_{sh}},$$

where J_{ph} is photogenerated current density, J_0 is dark saturation current density, R_s is series resistance, R_{sh} is shunt resistance, and n is ideality factor, respectively. The series resistance is related to the transport property of materials and interfaces (e.g., mobility of photoactive material and charge-transport materials, contact resistance), and both shunt resistance and saturation current are the measure of the unwanted recombination such as the leakage current under forward bias through defective structures.

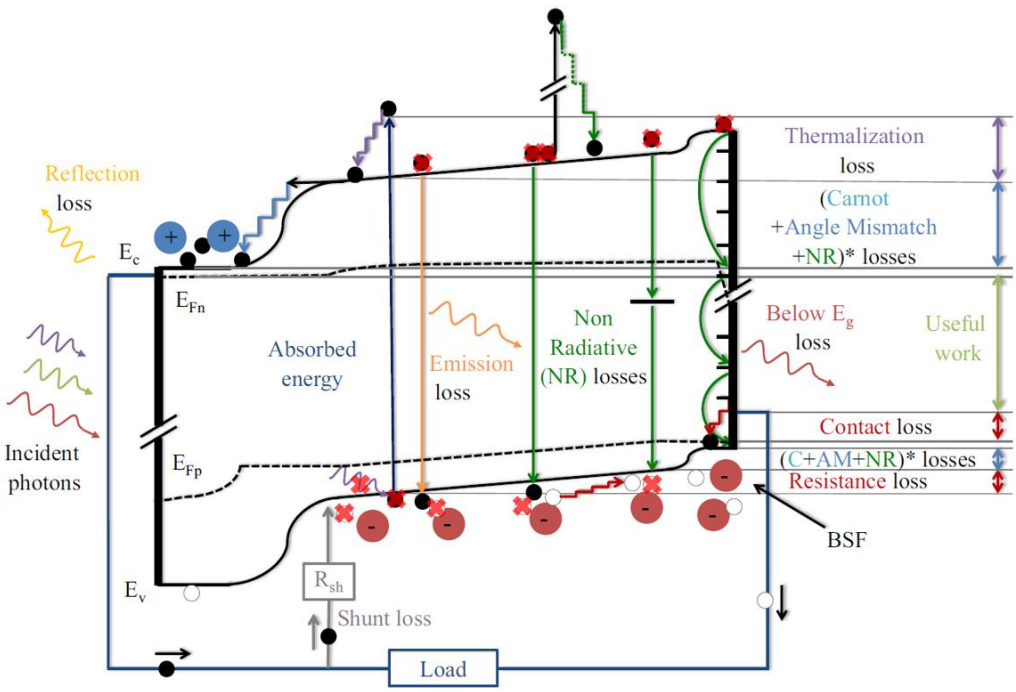

Fig. 1-1. (Color) Energy loss mechanism in a *p*-n junction. From Ref. [1].

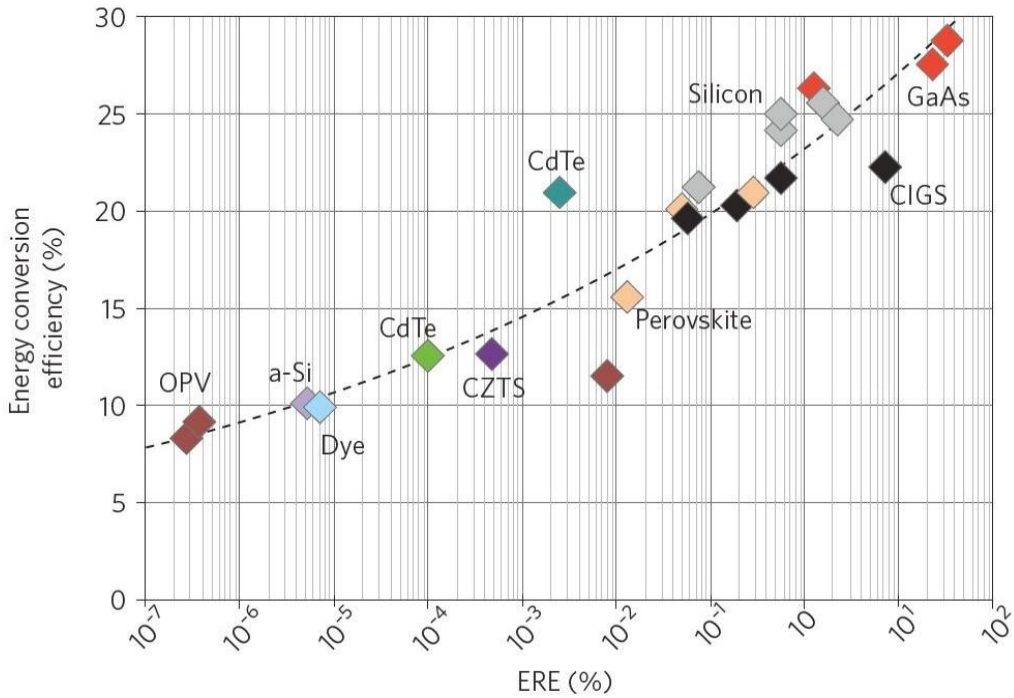

Fig. 1-2. (Color) General relation between external radiative efficiency (ERE) and energy conversion efficiency of solar cell in various photovoltaic materials. From Ref. [3].

1.2. Hybrid Perovskites and Photovoltaic Applications

Class of hybrid organic-inorganic halide perovskites for photovoltaic application normally has the composition of $(CH_3NH_3,(NH_2)_2CH,Rb,Cs)Pb(I,Br,Cl)_3$. $CH_3NH_3PbI_3$ (= $MAPbI_3$) is the most widely researched material since the revisit in 2009 [4]. It has a 3-dimensional structure, i.e. the corner-sharing of PbI_6 octahedron with the intercalation of $CH_3NH_3^+$, and it has an optical bandgap energy of about 1.6 eV. One of merits of hybrid perovskite is the facile film deposition via solution process. Precursor is prepared by dissolving constituent compounds (e.g., MAI and PbI_2 for $MAPbI_3$) in a common solvent. Complex is produced in a solution by the intercalation of solvent molecule (e.g., DMSO and DMF in common) into the layered-structure of PbI_2 with the ionization of organic salt. The intermediate complex is then uniformly coated on the substrate through the spin coating. The intermediate crystalline phase (e.g., PbI_2-DMSO-MAI) transforms into the polycrystalline hybrid perovskite during the thermal-annealing, which drives the evaporation of excess constituents (e.g., solvent) and the solid-state grain coarsening. The anti-solvent of precursor (e.g., chlorobenzene) is normally dripped during the spin coating to improve the perovskite quality, resulting in the compact and pinhole-free thin-film with the uniform coverage on the substrate [5].

Solution deposition presents the facile compositional variation through the proper mixing of organic salts and inorganic compounds, enabling for the wide range of solid solution with the microstructural and bandgap engineering. $((NH_2)_2CH)PbI_3$ (= $FAPbI_3$) is another common hybrid perovskite, which is simply assessed by substituting MAI into FAI in a precursor. It has an approximately 0.1 eV lower bandgap energy than $MAPbI_3$. Its polymorphism hinders the application of photoactive phase since the non-photoactive

phase is thermodynamically stable at room temperature. Compositional mixing with other materials having similar crystal structure and lattice constant is confirmed to stabilize the photoactive phase at room temperature. Phase stabilization is supported by the configurational entropic gain [6]. Various monovalent cations and halide anion are incorporated, for instance, $MAPbBr_3$ and $CsPbI_3$ are widely applied in many literatures. The substitutional mixing should consider the compromise between the crystalline phase and the bandgap energy. The increase of $CsPbI_3$ content in $(FAPbI_3)_{1-x}(CsPbI_3)_x$ results in the reduction of lattice constant and the increase of bandgap energy. Actually, the formation of non-photoactive phase is reduced by incorporating $CsPbI_3$, while the high content will inevitably leads to the absorption loss due to the blue-shift of bandgap. Similar trend is observed in $MAPbBr_3$ mixing in $(FAPbI_3)_{1-x}(MAPbBr_3)_x$. The composition of $(FAPbI_3)_{0.83}(MAPbBr_3)_{0.17}$ demonstrates the high device performance, and the additional Cs (and/or Rb) incorporation (triple- or quadruple-cation perovskite) further improves the performance, and the reasons for the enhancement will be discussed in the following sections [7]. Compositional mixing of $FAPbI_3$ and the following changes of both lattice constant and the bandgap energy are summarized in Fig. 1-3.

The superior intrinsic properties such as high absorption coefficient ($>10^4$ cm^{-1}), low defect density (Urbach energy of ~15 meV with defect density of $\sim10^{16}$ cm^{-3} in polycrystalline film) [8], and ambipolar charge transport property (mobility of ~60 cm^2 V^{-1} s^{-1}) [9], etc. support the high power-conversion efficiency, and optical and electrical properties are shown in Fig. 1-4. Low exciton binding energy (a few tens of meV) allows the free carrier formation, and the light effective mass of both e^- and h^+ and the low phonon-electron scattering result in the high charge mobility. Theoretical studies predict that dominant point defects generate shallow trap levels and grain boundaries do

not generate deep states in the bandgap of $MAPbI_3$. Sharp absorption edge and low Urbach tail suggest that no optically active states are present in the bandgap, and low defect density is supported by V_{oc} which approaches to the bandgap energy as can be compared to GaAs for high-quality material and amorphous Si in the opposite case.

Solar cell consists of layer-by-layer structure, where hybrid perovskite is in the middle between each selective contacts (Fig. 1-4). Criteria for the good selective contact are the favorable energy level alignment with hybrid perovskite and high charge mobility that it does not limit the photovoltaic performance. Fast charge transfer at the interface with the suppressed back transfer is required for the maximum extraction of photocarrier. Two types of architecture are commonly used, i.e. *n-i-p* (normal) and *p-i-n* (inverted) structure. Nanostructured electrode can also be applied, but the most cells adopt the planar or common mesoporous layer, probably due to the efficient light-harvesting property of hybrid perovskite itself. For the normal structure, light penetrates into the *n*-type layer while it is the *p*-type in the inverted structure. Wide bandgap oxide semiconductor or polymer is used as an *n*-type in the normal (e.g., TiO_2 and SnO_2) and *p*-type in the inverted structure (e.g., NiO, PEDOT:PSS). Small or polymeric molecular solution is used as *p*-type layer in the normal (e.g., Spiro-OMeTAD and PTAA) and *n*-type in the inverted structure (e.g., PCBM). For the upper layer deposition on hybrid perovskite, it certainly requires the solvent that is inactive to perovskite since the vulnerability to the polar solvent causes the decomposition into PbI_2 (e.g., H_2O, alcohol, acetone, acetonitrile, etc.). Selective contact also provides the physical barrier by hampering the diffusion of atmospheric reactive elements, and therefore the protective property is additionally required to reduce the degradation rate of hybrid perovskite.

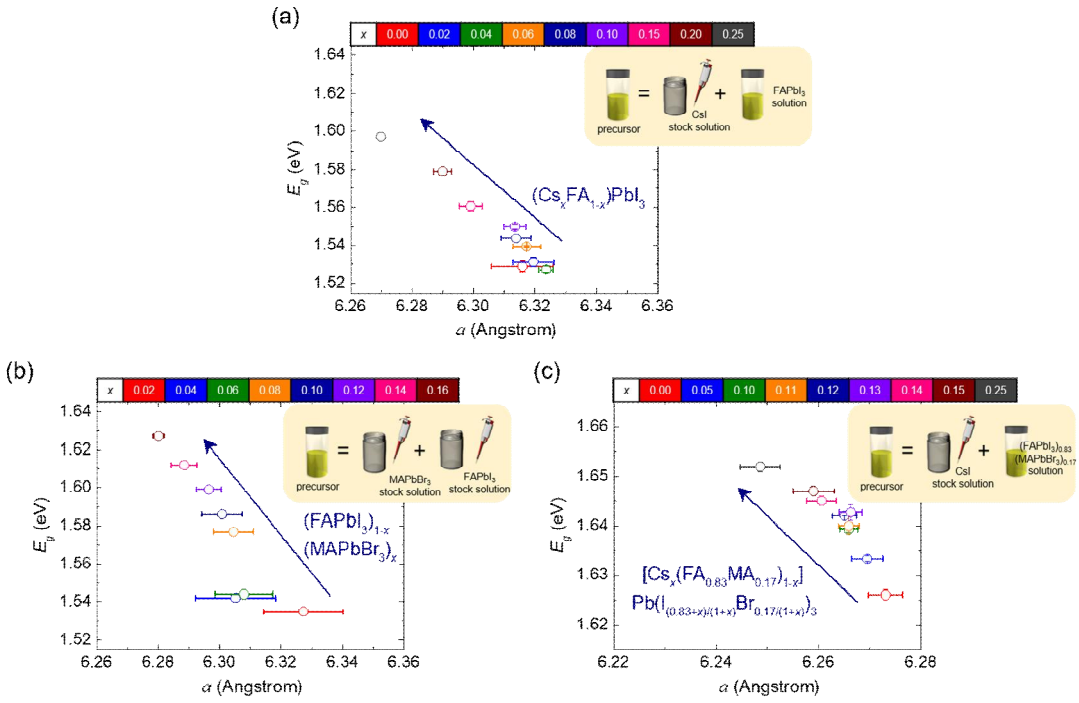

Fig. 1-3. (Color) Effects of compositional mixing of $FAPbI_3$ on lattice constant and bandgap energy. (a) $CsPbI_3$ in $FAPbI_3$. (b) $MAPbBr_3$ in $FAPbI_3$. (c) Cs incorporation in $(FAPbI_3)_{0.83}(MAPbBr_3)_{0.17}$. Lattice parameter is obtained by fitting the film diffraction (space group: *Pm3m*), and bandgap energy is obtained by fitting the film absorbance using Tauc equation, respectively.

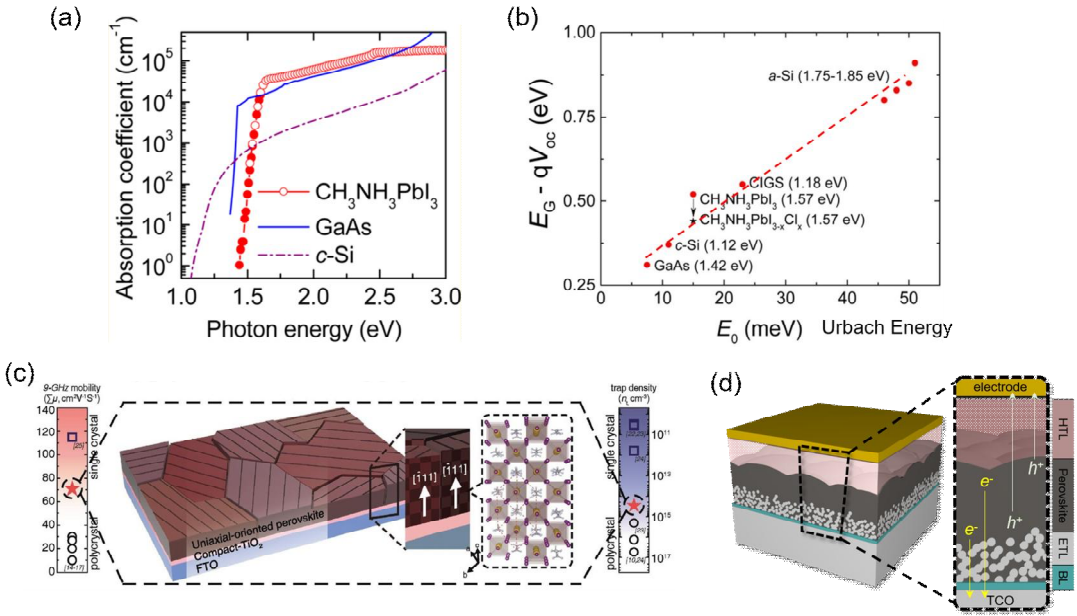

Fig. 1-4. (Color) (a) Absorption coefficient and (b) relation between Urbach energy and E_g - V_{oc} of various photovoltaic materials. From Ref. [8]. (c) Charge mobility and trap density of hybrid perovskites. From Ref. [9]. (d) Solar cell architecture (normal structure).

1.3. Microscopic Features of Perovskite for Efficient Solar Cells

Thickness of perovskite film should be enough to fully absorb the incident photon and simultaneously satisfy the charge extraction at the electrode, i.e., e^- which is generated near the *n*-type contact (for instance, *n-i-p* structure) must travel toward the opposite interface of *p*-type contact without recombination for the collection and vice versa for h^+. Normally, 400 nm to about 1 μm-thick perovskite film is used [10]. Since charge has to pass the grain boundary in the polycrystalline film, various attempts have been focused on the deposition of enlarged perovskite grains having high crystallinity. While some evidences support the benign effects of grain boundary (e.g., the band bending and subsequent charge separation [11]), the complex character of grain boundary (e.g., amorphous structure [12]) brings the difficulty on the systematic control for the effective utilization.

For the grain growth, intermediate phase engineering is utilized to induce the enlarged grains via the oriented attachment during the grain growth, providing the high charge mobility and low electronic trap density [9]. Grain coarsening through the prolonged thermal-annealing results in the micrometer-sized grains, with the much grain growth on the hydrophobic than the hydrophilic substrate [13]. Hydrophobic substrate provides the low nucleation rate, and thereby the control of nucleation and diffusion rate through the rational selection of substrate and precursor enables for the single-crystal solar cell [14]. For the thermal-annealing, it should be cautious that the prolonged annealing might cause the loss the constituent elements such as MAI and MACl, which ultimately leads to the decomposition into PbI_2. Meanwhile, PbI_2 is known to have both benign and detrimental effects on the cell performance [15]. For example, the excess PbI_2 formed at

the perovskite grain boundary (self-induced passivation) reduces the photocarrier recombination, and it is proposed to originate from the energy level alignment of PbI_2 at interface for blocking the recombination [16]. However, PbI_2 is a non-photoactive material (bandgap energy of 2.3 eV) with the conduction (valence) band to be upper (lower) level than that of $MAPbI_3$, forming the energy barrier and thereby hampering the charge transfer. It is commonly considered as an impurity, and therefore the careful control of PbI_2 content with the grain boundary character is essential for the nonstoichiometric film-based efficient cell. For the grain growth, Ostwald ripening is also utilized through the reconstruction reaction by dissolution and recrystallization of perovskite [17]. Effect of enlarged grains on the photovoltaic performance with the strategies for reducing electronic traps are shown in Fig. 1-5 [18,19].

Perovskite degradation can be reduced through the grain growth. Hybrid perovskite is vulnerable to H_2O due to the hygroscopic nature of organic molecule with the possibility of hydrogen bond formation. $MAPbI_3$ readily decomposes into PbI_2, and the reaction mechanism is revealed [20]. Hydration of hybrid perovskite proceeds through the two steps, where the first reaction is the formation of monohydrate ($CH_3NH_3PbI_3 \cdot H_2O$) which can be reversibly transformed into the original $CH_3NH_3PbI_3$ under the dry condition. Further incorporation of H_2O results in the irreversible formation of dihydrate $(CH_3NH_3)_4PbI_6 \cdot 2H_2O$ and PbI_2. It seems likely that the irreversibility of monohydrate-to-dihydrate reaction is due to the formation of separate solid-phase of PbI_2, and also H_2O further dissolves organic cation in dihydrate that it decomposes into PbI_2. The summarized reaction mechanism is as follow [20]:

$$4CH_3NH_3PbI_3 + 4H_2O \leftrightarrow 4(CH_3NH_3PbI_3 \cdot H_2O)$$

$$\rightarrow (CH_3NH_3)_4PbI_6 \cdot 2H_2O + 3PbI_2 + 2H_2O$$

$$\rightarrow 4CH_3NH_3I + 4PbI_2 + 4H_2O.$$

Under the humid condition, the universal scalability of stability improvement as the grain size increase implies that grain boundary plays a critical role on the hydration reaction.

The grain-boundary-mediated degradation is also observed under the O_2 environment [21]. As the $CH_3NH_3PbI_3$ particle size increases, the superoxide formation is diminished. The degradation reaction under O_2 is proposed as follow:

$$4CH_3NH_3PbI_3 + O_2 \rightarrow 2H_2O + 4CH_3NH_2 + 4PbI_2 + 2I_2.$$

The reduction of partial vapor pressure of product (e.g., I_2 gas) can reduce the free energy of reaction, thereby the reaction can be thermodynamically stable. For the case of $FAPbI_3$, the improved stability is expected since the deprotonation is less favored for FA than MA cation [22]. In that sense, the enlarged grains not only provide the short-term efficiency of solar cell by reducing the electronic traps, but also present the long-term stability by suppressing the material degradation. Even so, the complete suppression is not realized through the grain growth, and the additional encapsulation for blocking the diffusion of reactive species is required for the high durability.

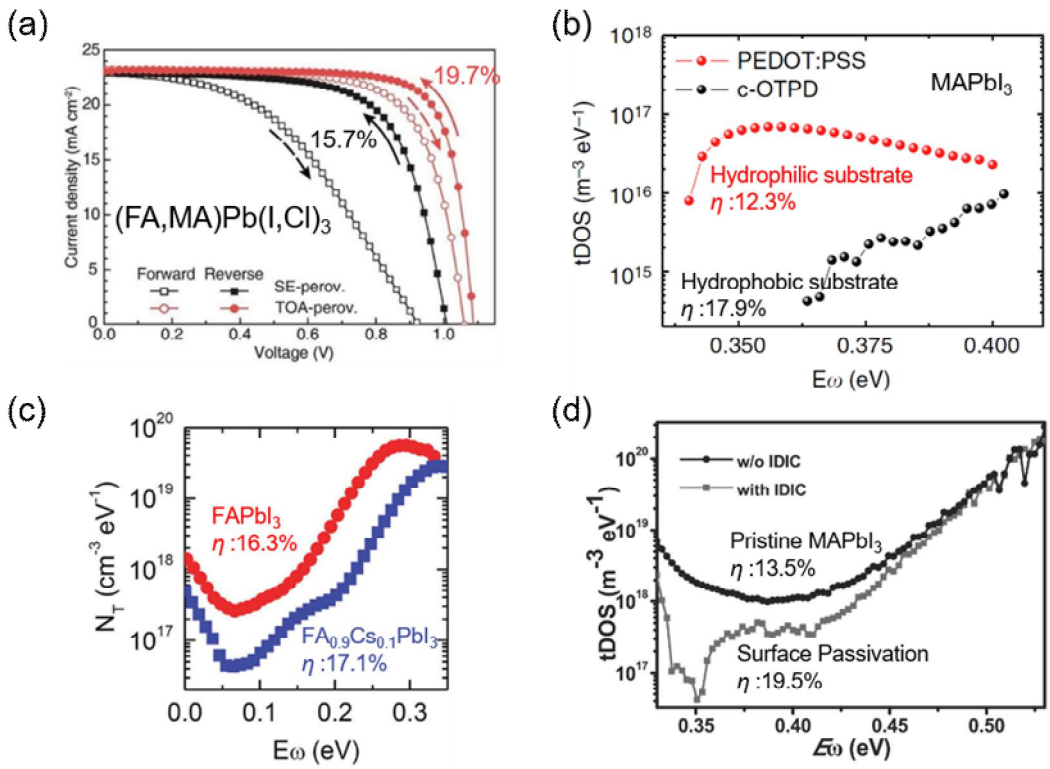

Fig. 1-5. (Color) (a) *J-V* comparison between the common solvent engineering (SE-perov.) and oriented attachment for the enlarged grain (TOA-perovs.) method. From Ref. [9]. (b) Effect of $MAPbI_3$ grain size on trap density of state (tDOS) (PEDOT:PSS substrate for 300 nm grains and c-OTPD for 800 nm grains, respectively). From Ref. [13]. (c) Effect of Cs doping in $FAPbI_3$ on tDOS. From Ref. [18]. (d) Surface passivation of $MAPbI_3$ using conjugated Lewis base (IDIC). From Ref. [19].

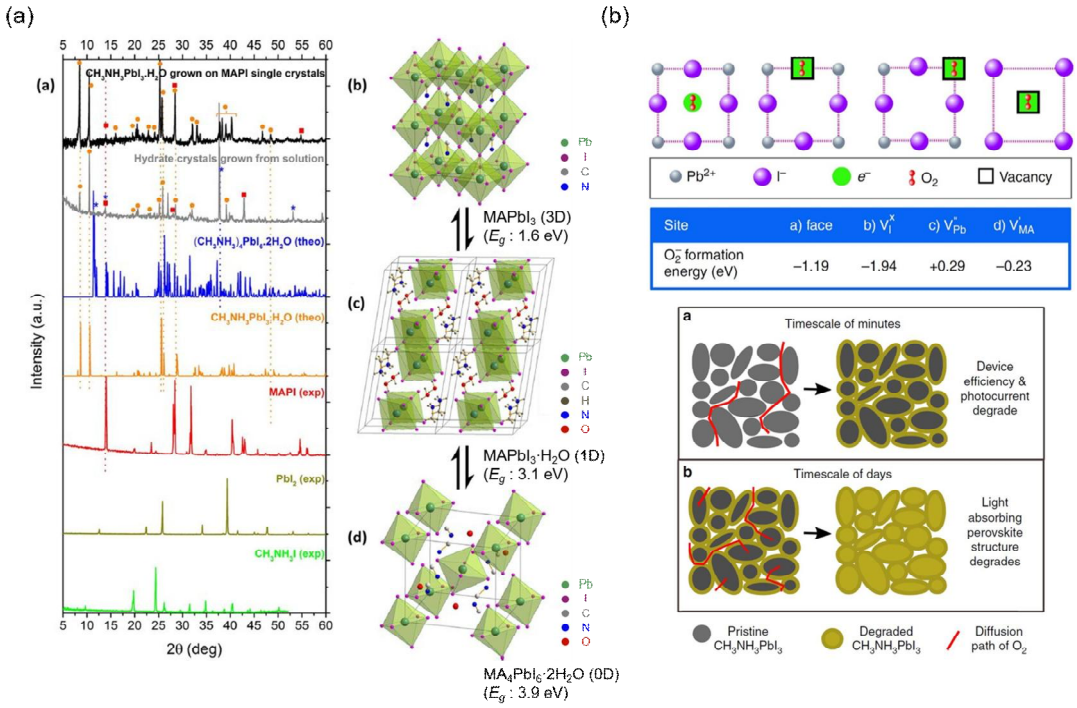

Fig. 1-6. (Color) (a) $MAPbI_3$ degradation under H_2O, with monohydrate and dihydrate crystal structure. From Ref. [20]. (b) Proposed mechanism of grain-boundary-mediated $MAPbI_3$ degradation under O_2. From Ref. [21].

1.4. Nanoscopic Features and Their Impacts on Performance

Previous studies highlight that both fine grains and high defect density cause the perovskite degradation. The degradation should be understood in aspect of point defects as well as microstructural properties. Theoretical studies predict various kinds of point defects and their energy levels in bandgap [23]. The formation energy of intrinsic defect changes depending on the chemical potential of constituent element, and therefore, the perovskite growth condition has a significant impact on the dopant type (i.e. *p*-type, intrinsic, or *n*-type perovskite). (For example, the Pb vacancy, I and CH_3NH_3 interstitials are predicted to have low formation energies, where Pb vacancy and I interstitial are the *p*-type dopant and CH_3NH_3 interstitial is the *n*-type dopant, respectively [23].) Experimental results support the change of dominant defects depending on the growth condition. Annealing temperature of perovskite has an influence on the doping property of $MAPbI_3$, where *p*-type to intrinsic to *n*-type is sequentially varied as the temperature increases [24]. When the sequential deposition is applied (dipping of the pre-coated PbI_2 in a MAI solution), the low annealing temperature results in the excess iodine (or Pb vacancy) that *p*-type character is obtained. As the temperature increases, the excess MAI evaporates that opposite case of iodine deficiency (Pb rich) causes the change to *n*-type. In addition, the post-treatment using I_2 vapor is demonstrated to increases the work function of $MAPbI_3$ with the reduction of ionic conductivity, probably cause the I interstitial or the vacancy [25]. It is difficult to pinpoint the dominant defect in different experiments, and even so, many computational and experimental studies provide the evidences of methylammonium- and iodine-related defects (vacancy and interstitial) [26].

Iodine vacancy is proposed to mediate the perovskite degradation reaction [21].

Ab initio simulations provide that iodine vacancy is the preferred site for the formation of superoxide from O_2 molecule, and the smaller size of O_2 (bond length of 342 pm) compared to iodide ion (Shannon ionic diameter of 440 pm) supports the above hypothesis. Actually, the reduction of defects by MAI post-treatment on $MAPbI_3$ improves the material stability, supporting the atomic-vacancy-mediated degradation. The detrimental effect of O_2 on electrical property is also observed. The electronic doping by O_2 adsorption is demonstrated through the surface work function change after the O_2 injection in $MAPbBr_3$ [27]. The reversible adsorption and desorption at grain boundary modifies the electric field between adjacent grains, and the retention to the original performance is confirmed after the removal of O_2. Furthermore, the additional electronic trap formation under O_2 is demonstrated in $MAPbI_3$ [28]. It is expected to be attributed to the capture of electrons in trap states coming from O_2 chemisorbed on $MAPbI_3$ as shown in Fig. 1-7, and the exact mechanism needs to be further examined. The degradation could be related to the generation of high trap densities by the adsorption of O_2.

The exploration about the merits on the small ion addition in perovskite which does not satisfy the tolerance factor for the perovskite structure has attractive attentions, and the typical example is the role of chlorine in $MAPbI_3$ [29,30]. (Ionic radii are provided for a reference; FA^+ 253 pm, MA^+ 217 pm, Cs^+ 167 pm, Rb^+ 152 pm, K^+ 138 pm, Ag^+ 115 pm, Na^+ 102 pm, Cu^+ 77 pm, Li^+ 76 pm, I-220 pm, Br^- 196 pm, and Cl^- 181 pm, respectively. Monovalent cation that is incorporated into perovskite in various literatures is also compared.) By changing the precursor from PbI_2 to $PbCl_2$, the microstructural evolution to the defect chemistry are modified with the significant cell performance change. Due to the ionic size difference between chlorine and iodine, Cl content in the $MAPbI_3$ structure is predicted to be less than 3-4% (i.e., Cl/I ratio) [31]. In addition, chlorine is facile to

evaporate during the thermal-annealing. It is confirmed by *in-situ* examination of x-ray absorption near edge structure (XANES) spectra that the Cl to Pb atomic ratio decreases as annealing time increases [32]. The extended x-ray absorption fine structure (EXAFS) studies the environment of Pb coordination in $MAPbI_3(Cl)$ depending on the precursor molar ratio (including MAI : $PbCl_2$ = 3:1). It is revealed that the highest Pb-I coordination (which is to be 6) results in the preferential growth along *c*-axis of a tetragonal $MAPbI_3$ while others having iodine vacancy (even chlorine at low molar ratio) is correlated to the lack of crystalline order along the *c*-axis [33]. The abnormal grain growth is further revealed that addition of extra MACl in precursor ($MAI+PbI_2$) results in the micrometer-sized grains which far exceed the film thickness [34]. It is supported by the interfacial Cl on TiO_2 substrate that lead to the stronger interaction coupling between $MAPbI_3$ and TiO_2 [35].

Besides the nanostructural change, the diffusion of constituent ion in perovskite is proposed to play a key role in solar cell performance. The addition of small ion is comprehensively studied, i.e., LiI, NaI, KI, RbI, and CsI in perovskite precursor [36]. For the optimized cells, KI is demonstrated to be superior compared to the counterpart (without KI). Although the change of lattice constant is minute (e.g., 6.277 ± 0.002 Å for the without KI, and 6.293 ± 0.001 Å for 10 μmol KI), the reduced trap density by KI incorporation results in the performance improvement with the negligible hysteresis. The increased lattice parameter underlines that potassium ion might be placed at the interstitial site rather than substitutional site. Supported from computational calculation, the Frenkel defect formation ($I_I \rightarrow I_i^- + V_I^+$) is limited by the hindrance of iodine migration from the lattice site to the interstitial site by the interstitial K as shown in Fig. 1-8. Since Frenkel defect can be formed under the excess electron from the theoretical calculation, the

reduction of electron accumulation at the cathode might minimize the defect formation with the hysteresis behavior of perovskite solar cells. Another role of KI addition is suggested [37]. The reduction of vacancy defect by excess halide results in the passivation of nonradiative recombination pathways, leading to high photoluminescence efficiency. It is observed that KI addition leads to the immobilization of K-rich, halide-sequestered species at the grain boundary and surface, inhibiting the ion migration and suppressing the nonradiative recombination.

In summary, the impacts of both microstructural properties and point defects on both the temporal evaluation and the long-term stability of the perovskite solar cell are overviewed, highlighting the necessity for the comprehensive analyses of microscopic and nanoscopic features. In this thesis, the compositional engineering of hybrid perovskite is performed, and its effects on microstructures and electronic traps are characterized. It is aimed to find the critical factor that has a significant influence on the short- and long-term solar cell performance. Utilizing the merits of compositional mixing, the additional defect passivation is performed through the post-deposition treatment for the further performance improvements. The flowchart for the design of efficient perovskite solar cell is illustrated in Fig. 1-9.

(a)

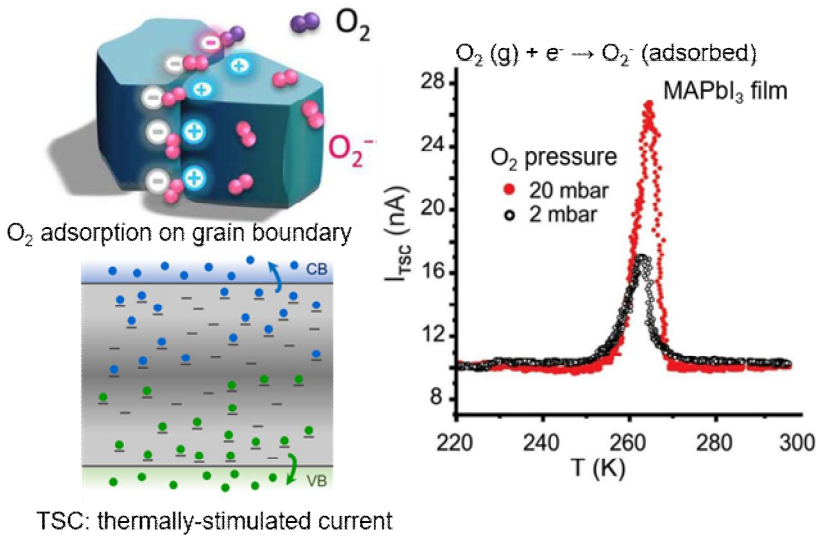

(b)

		2 mbar		20 mbar	
		N_t (cm^{-3})	Ea (eV)	N_t (cm^{-3})	Ea (eV)
$MAPbI_3$	Trap 1	9.14×10^{16}	0.18	2.16×10^{16}	0.12
	Trap 2	4.75×10^{16}	0.49	7.29×10^{16}	0.52
	Trap 3	…	…	7.59×10^{16}	1.42
$MAPbI_2Br$	Trap 1	2.82×10^{16}	0.25	1.52×10^{17}	0.45
	Trap 2	2.30×10^{16}	0.95	2.21×10^{17}	1.03
	Trap 3	…	…	9.01×10^{16}	1.25
$MAPbI_2Cl$	Trap 1	…	…	4.11×10^{17}	0.07

Fig. 1-7. (Color) (a) Effect of O_2 adsorption on the thermally-stimulated current for $MAPbI_3$ thin film. (b) Trap states of $MAPbI_3$, $MAPbI_2Br$, and $MAPbI_2Cl$ (precursor ratio) depending on the oxygen partial pressure. Schematic image (left upper image) in (a) from Ref. [27], and others (except left lower image in (a)) from Ref. [28], respectively.

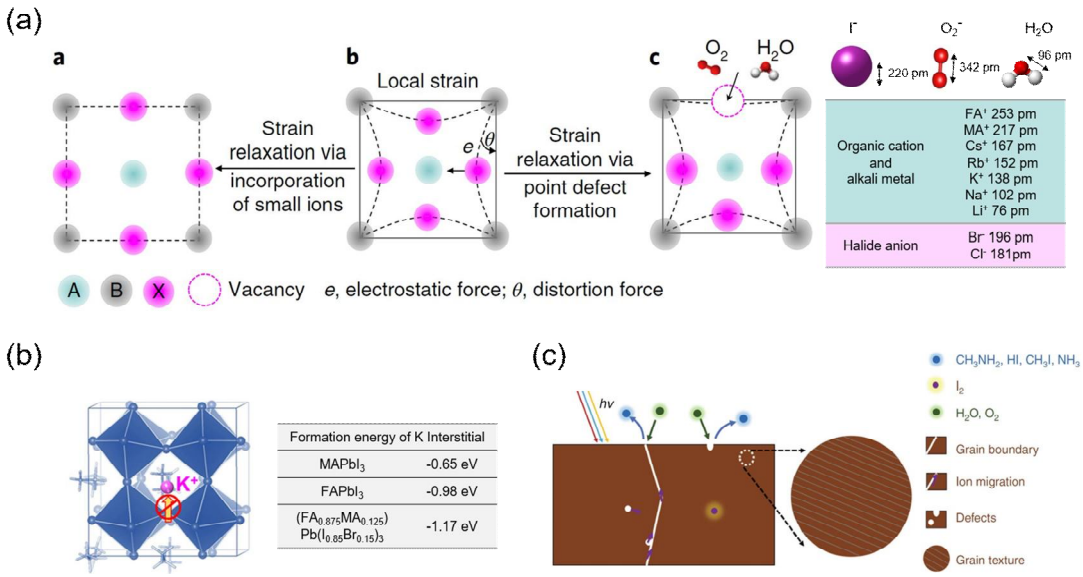

Fig. 1-8. (Color) (a) Proposed mechanism of the strain relaxation by small ion incorporation. From Ref. [29]. (b) Effect of KI addition on Frenkel defect formation. Table for the predicted formation energies of K interstitial on various compositional perovskites. From Ref. [36]. (c) Film degradation mechanism via defects. From Ref. [10].

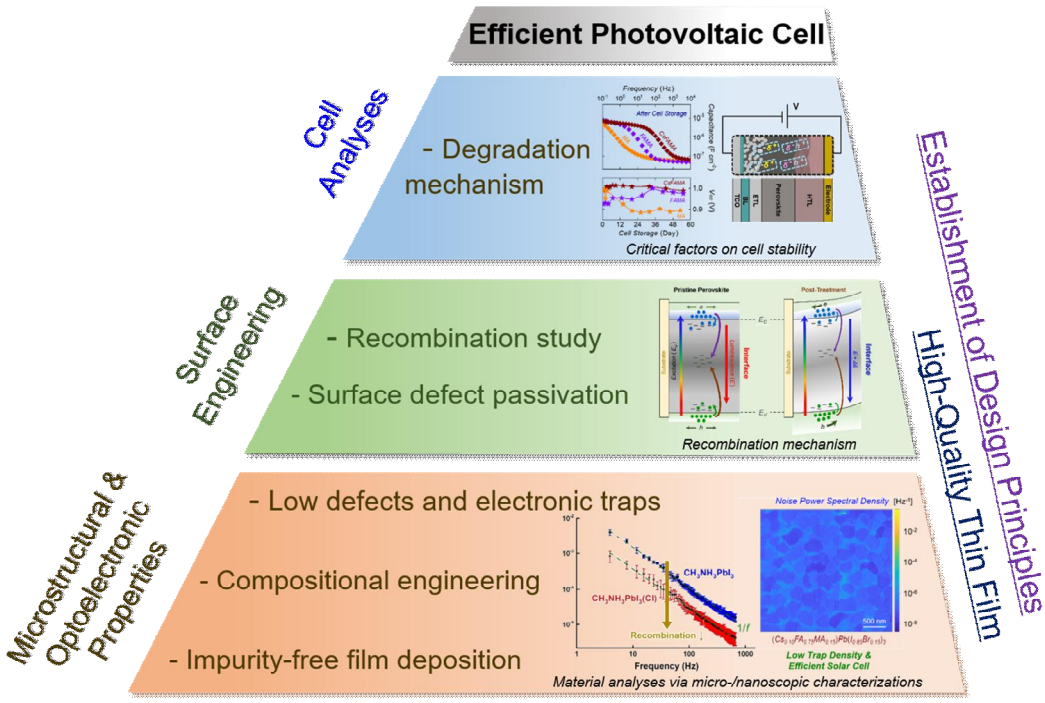

Fig. 1-9. (Color) Flowchart for the design of efficient perovskite solar cells.

1.5. References

1. Dupre, O.; Vaillon, R.; Green, M. A. Physics of the Temperature Coefficients of Solar Cells. *Sol Energ. Mater. Sol. C.* **2015**, *140*, 92-100.
2. Vossier, A.; Gualdi, F.; Dollet, A.; Ares, R.; Aimez, V. Approaching the Shockley-Queisser Limit: General Assessment of the Main Limiting Mechanisms in Photovoltaic Cells. *J. Appl. Phys.* **2015**, *117*, 015102.
3. Green, M. A.; Bremner, S. P. Energy Conversion Approaches and Materials for High-Efficiency Photovoltaics. *Nat. Mater.* **2017**, *16*, 23-34.
4. Kojima, A.; Teshima, K.; Shirai, Y.; Miyasaka, T. Organometal Halide Perovskites as Visible-Light Sensitizers for Photovoltaic Cells. *J. Am. Chem. Soc.* **2009**, *131*, 6050-6051.
5. Jeon, N. J.; Noh, J. H.; Kim, Y. C.; Yang, W. S.; Ryu, S.; Seok, S. I. Solvent Engineering for High-Performance Inorganic-Organic Hybrid Perovskite Solar Cells. *Nat. Mater.* **2014**, *13*, 897-903.
6. Yi, C.; Luo, J.; Meloni, S.; Boziki, A.; Ashari-Astani, N.; Gratzel, C.; Zakeeruddin, S. M.; Rothlisberger, U.; Gratzel, M. Entropic Stabilization of Mixed A-Cation ABX_3 Metal Halide Perovskites for High Performance Perovskite Solar Cells. *Energy Environ. Sci.* **2016**, *9*, 656-662.
7. Saliba, M.; Matsui, T.; Donamski, K.; Seo, J.-Y.; Ummadisingu, A.; Zakeeruddin, S. M.; Correa-Baena, J.-P.; Tress, W. R.; Abate, A.; Hagfeldt, A.; Gratzel, M. Incorporation of Rubidium Cations into Perovskite Solar Cells Improves Photovoltaic Performance. *Science* **2016**, *354*, 206-209.

8. Wolf, S. D.; Holovsky, J.; Moon, S.-J.; Loper, P.; Niesen, B.; Ledinsky, M.; Haug, F.-J.; Yum, J.-H.; Ballif, C. Organometallic Halide Perovskites: Sharp Optical Absorption Edge and Its Relation to Photovoltaic Performance. *J. Phys. Chem. Lett.* **2014**, *5*, 1035-1039.
9. Kim, D. H.; Park, J.; Li, Z.; Yang, M.; Park, J.-S.; Park, I. J.; Kim, J. Y.; Berry, J. J.; Rumbles, G.; Zhu, K. 300% Enhancement of Carrier Mobility in Uniaxial-Oriented Perovskite Films Formed by Topotactic-Oriented Attachment. *Adv. Mater.* **2017**, *29*, 1606831.
10. Liu, Z.; Qiu, L.; Juarez-Perez, E. J.; Hawash, Z.; Kim, T.; Jiang, Y.; Wu, Z.; Raga, S. R.; Ono, L. K.; Liu, S.; Qi, Y. Gas-Solid Reaction Based over One-Micrometer Thick Stable Perovskite Films for Efficient Solar Cells and Modules, *Nat. Commun.* **2018**, *9*, 3880.
11. Kim, D.; Kim, G. Y.; Ko, C.; Pae, S. R.; Lee, Y. S.; Gunawan, O.; Ogletree, D. F.; Jo, W.; Shin, B. Effects of Postsynthesis Thermal Conditions on Methylammonium Lead Halide Perovskite: Band Bending at Grain Boundaries and Its Impacts on Solar Cell Performance. *J. Phys. Chem. C.* **2016**, *120*, 21330-21335.
12. Wang, Q.; Chen, B.; Liu, Y.; Deng, Y.; Bai, Y.; Dong, Q.; Huang, J. Scaling Behavior of Moisture-Induced Grain Degradation in Polycrystalline Hybrid Perovskite Thin Films. *Energy Environ. Sci.* **2017**, *10*, 516-522.
13. Bi, C.; Wang, Q.; Shao, Y.; Yuan, Y.; Xiao, Z.; Huang, J. Non-Wetting Surface-Driven High-Aspect-Ratio Crystalline Grain Growth for Efficient Hybrid Perovskite Solar Cells. *Nat. Commun.* **2015**, *6*, 7747.

14. Chen, Z.; Dong, Q.; Liu, Y.; Bao, C.; Fang, Y.; Lin, Y.; Tang, S.; Wang, Q.; Xiao, X.; Bai, Y.; Deng, Y.; Huang, J. Thin Single Crystal Perovskite Solar Cells to Harvest Below-Bandgap Light Absorption. *Nat. Commun.* **2017**, *8*, 1890.
15. Jacobsson, T. J.; Correa-Baena, J.-P.; Anaraki, E. H.; Philippe, B.; Stranks, S. D.; Bouduban, M. E. F.; Tress, W.; Schenk, K.; Teuscher, J.; Moser, J.-E.; Rensmo, H.; Hagfeldt. Unreacted PbI_2 as a Double-Edged Sword for Enhancing the Performance of Perovskite Solar Cells. *J. Am. Chem. Soc.* **2016**, *138*, 10331-10343.
16. Chen, Q.; Zhou, H.; Song, T.-B.; Luo, S.; Hong, Z.; Duan, H.-S.; Dou, L.; Liu, Y.; Yang, Y. Controllable Self-Induced Passivation of Hybrid Lead Iodide Perovskites toward High Performance Solar Cells. *Nano Lett.* **2014**, *14*, 4158-4163.
17. Yang, M.; Zhang, T.; Schulz, P.; Li, Z.; Li, G.; Kim, D. H.; Guo, N.; Berry, J. J.; Zhu, K.; Zhao, Y. Facile Fabrication of Large-Grain $CH_3NH_3PbI_{3-x}Br_x$ Films for High-Efficiency Solar Cells via CH_3NH_3Br-Selective Ostwald Ripening. *Nat. Commun.* 2016, **7**, 12305.
18. Lee, J.-W.; Kim, D.-H.; Kim, H.-S.; Seo, S.-W.; Cho, S. M.; Park, N.-G. Formamidinium and Cesium Hybridization for Photo- and Moisture-Stable Perovskite Solar Cell. *Adv. Energy Mater.* **2015**, *5*, 1501310.
19. Lin, Y.; Shen, L.; Dai, J.; Deng, Y.; Wu, Y.; Bai, Y.; Zheng, X.; Wang, J.; Fang, Y.; Wei, H.; Ma, W.; Zeng, X. C.; Zhan, X.; Huang, J. π-Conjugated Lewis Base: Efficient Trap-Passivation and Charge-Extraction for Hybrid Perovskite Solar Cells. *Adv. Mater.* **2017**, *29*, 1604545.
20. Leguy, A. M. A.; Hu, Y.; Campoy-Quiles, M.; Alonso, M. I.; Weber, O. J.; Azarhoosh, P.; Schilfgaarde, M. v.; Weller, M. T.; Bein, T.; Nelson, J.; Docampo, P.,

Barnes, P. R. F. Reversible Hydration of $CH_3NH_3PbI_3$ in Films, Single Crystals, and Solar Cells. *Chem. Mater.* **2015**, *27*, 3397-3407.

21. Aristidou, N.; Eames, C.; Sanchez-Molina, I.; Bu, X.; Kosco, J.; Islam, M. S.; Haque, S. A. Fast Oxygen Diffusion and Iodide Defects Mediate Oxygen-Induced Degradation of Perovskite Solar Cells. *Nat. Commun.* **2017**, *8*, 15218.
22. Senocrate, A.; Acarturk, T.; Kim, G. Y.; Merkle, R.; Starke, U.; Gratzel, M.; Maier, J. Interaction of Oxygen with Halide Perovskites. *J. Mater. Chem. A* **2018**, *6*, 10847-10855.
23. Yin, W.-J.; Shi, T.; Yan, Y. Unusual Defect Physics in $CH_3NH_3PbI_3$ Perovskite Solar Cell Absorber. *Appl. Phys. Lett.* **2014**, *10*, 063903.
24. Song, D.; Cui, P.; Wang, T.; Wei, D.; Li, M.; Cao, F.; Yue, X.; Fu, P.; Li, Y.; He, Y.; Jiang, B.; Trevor, M. Managing Carrier Lifetime and Doping Property of Lead Halide Perovskite by Postannealing Processes for Highly Efficient Perovskite Solar Cells. *J. Phys. Chem. C* **2015**, *119*, 22812-22819.
25. Zohar, A.; Levine, I.; Gupta, S.; Davidson, O.; Azulay, D.; Milo, O.; Balberg, I.; Hodes, G.; Cahan, D. What is the Mechanism of $MAPbI_3$ p-doping by I_2? Insights from Optoelectronic Properties. *ACS Energy Lett.* **2017**, *2*, 2408-2414.
26. Hwang, T.; Lee, B.; Kim, J.; Lee, S.; Gil, B.; Yun, A. J.; Park, B. From Nanostructural Evolution to Dynamic Interplay of Constituents: Perspectives for Perovskite Solar Cells. *Adv. Mater.* **2018**, 1704208.
27. Yuan, Y.; Li, Tao; Wang, Q.; Xing, J.; Gruverman, A.; Huang, J. Anomalous Photovoltaic Effect in Organic-Inorganic Hybrid Perovskite Solar Cells. *Sci. Adv.* **2017**, *3*, e1602164.

28. Gordillo, G.; Otalora, C. A.; Reinoso, M. A. Trap Center Study in Hybrid Organic-Inorganic Perovskite Using Thermally-Stimulated Current (TSC) Analyses. *J. Appl. Phys.* **2017**, *122*, 075304.

29. Saidaminov, M. I.; Kim, J.; Jain, A.; Quintero-Bermudez, R.; Tan, H.; Long, G.; Tan, F.; Johnston, A.; Zhao, Y.; Voznyy, O.; Sargent, E. H. Suppression of Atomic Vacancies via Incorporation of Isovalent Small Ions to Increase the Stability of Halide Perovskite Solar Cells in Ambient Air. *Nat. Energy* **2018**, *3*, 648-654.

30. Hwang, T.; Cho, D.; Kim, J.; Kim, J.; Lee, S.; Lee, B.; Kim, K. H.; Hong, S.; Kim, C.; Park, B. Investigation of Chlorine-Mediated Microstructural Evolution of $CH_3NH_3PbI_3(Cl)$ Grains for High Optoelectronic Responses. *Nano Energy* **2016**, *25*, 91-99.

31. Colella, S.; Mosconi, E.; Fedeli, P.; Listorti, A.; Gazza, F.; Orlandi, F.; Ferro, P.; Besagni, T.; Rizzo, A.; Calestani, G.; Gigli, G.; Angelis, F. D.; Mosca, R. $MAPbI_{3-x}Cl_x$ Mixed Halide Perovskite for Hybrid Solar Cells: The Role of Chloride as Dopant on the Transport and Structural Properties. *Chem. Mater.* **2013**, *25*, 4613-4618.

32. Pool, V. L.; Gold-Parker, A.; McGehee, M. D.; Toney, M. F. Chlorine in $PbCl_2$-Derived Hybrid-Perovskite Solar Absorbers. *Chem. Mater.* **2015**, *27*, 7240-7243.

33. McLeod, J. A.; Wu, Z.; Sun, B.; Liu, L. The Influence of the I/Cl Ratio on the Performance of $CH_3NH_3PbI_{3-x}Cl_x$-based Solar Cells: Why is CH_3NH_3I : $PbCl_2$ = 3:1 the "magic" ratio? *Nanoscale* **2016**, *8*, 6361-6368.

34. Lee, B.; Hwang, T.; Lee, S.; Shin, B.; Park, B. Microstructural Evolution of Hybrid Perovskites Promoted by Chlorine and Its Impact on the Performance of Solar Cell. *Sci. Rep.* **submitted**.

35. Mosconi, E.; Ronca, E.; Angelis, F. D. First-Principles Investigation of the TiO_2/Organohalide Perovskites Interface: The role of Interfacial Chlorine. *J. Phys. Chem. Lett.* **2014**, *5*, 2619-2625.

36. Son, D.-Y.; Kim, S.-G.; Seo, J.-Y.; Lee, S.-H.; Shin, H.; Lee, D.; Park, N-.G. Universal Approach toward Hysteresis-Free Perovskite Solar Cell via Defect Engineering. *J. Am. Chem. Soc.* **2018**, *140*, 1358-1364.

37. Abdi-Jalebi, M.; Andaji-Garmaroudi, Z.; Cacovich, S.; Stavrakas, C.; Phillippe, B.; Richter, J. M.; Alsari, M.; Booker, E. P.; Hutter, E. M.; Pearson, A. J.; Lilliu, S.; Savenije, T. J.; Rensmo, H.; Divitini, G.; Ducati, C.; Friend, R. H.; Stranks, S. D. Maximizing and Stabilizing Luminescence from Halide Perovskites with Potassium Passivation. *Nature* **2018**, *555*, 497-501.

Chapter 2.

Electronic Traps and its Correlations to Perovskite Solar-Cell Performance via Compositional and Thermal-Annealing Controls

2.1. Introduction

Organic-inorganic lead halide perovskites demonstrate remarkable optical and semiconducting properties that hybrid perovskites are applied in various optoelectronic devices, especially on solar cells. Currently, solar cells mark the power-conversion efficiency over 23%, which is enabled by the defect engineering of perovskite and the development of charge-transport materials [1]. Polycrystalline characters of perovskite films face the challenges in that understanding how the micro-/nanoscopic features in both perovskite and interface correlate to the photovoltaic parameters is the main interest to improve the solar cell efficiency [2].

Approaches for the thermodynamic limit of solar cell efficiency have been widely dealt, and strong luminescence is one of a necessity for minimizing the deficit between the bandgap energy and open-circuit voltage [3-9]. The microstructural control for micron-sized grains results in intense photoluminescence and improved photovoltaic

---

*The work presented in Chap. 2 is submitted to *ACS Applied Materials and Interfaces* entitled,
"Electronic Traps and its Correlations to Perovskite Solar-Cell Performance via Compositional and Thermal-Annealing Controls"
Taehyun Hwang, Alan Jiwan Yun, Jinhyun Kim, Duckhyung Cho, Sangyeon Kim, Seunghun Hong, and Byungwoo Park*

performance in polycrystalline perovskite thin films [10-13]. The effectiveness of grain boundary passivation for increasing radiative recombinations and photocarrier lifetimes underscores the grain growth (or low-angle grain boundary) for high performance [11,14,15]. Also, grain-boundary-mediated perovskite and solar cell degradations are pointed to bottleneck the long-term stability. Deteriorations of cell performance are correlated to the irreversible reactions originating from the diffusion of atmospheric chemicals into the film interior [16,17]. Point defects are also suggested to accelerate the degradation by vacancy-assisted decomposition, while incorporation of small ions for reducing local strains can result in improved stability [18]. Accordingly, reduced defects in both bulk films and interfaces lead to the state-of-the-art solar cells with a substantial luminescence yield [5,19-21]. Improvement mechanisms commonly suggest the dominant roles by lattice and interfacial defects: defect density, local strains induced by lattice vacancy, ionic/vacancy diffusion, and consequent electronic traps for carrier recombination and chemical reactions [5,17-20,22].

Defect reduction by molecular and atomic species emphasizes that electronic traps are controllable variables enabling for a high performance. Passivating elements include both constitutional ions such as I_3^-, MAI (MA: methylammonium) and extrinsic species for bonding (incorporating) with (into) the atomic vacancies [17-21,23]. Dominant defect species are suggested as interstitials and vacancies with shallow electronic levels near the bandedges, and antisite defects are expected to have deep levels at the interfaces [2,19,24]. To reduce the defects and traps, complex mixing for $(Rb_aCs_bMA_cFA_d)Pb(I_xBr_y)_3$ (FA: formamidinium) is demonstrated to be effective with the formation of photoactive structures [21]. Optimal cation/anion composition reduces the trap densities with the shift toward shallow levels with facilitating fast crystallization, achieving high-quality grains

[21,25]. Smaller ion addition such as K^+, Cd^{2+}, and Cl^- also improves the cell performance even though the tolerance factor for the perovskite structure is not quite satisfactory [5,18,20,26,27]. High defect-formation energies by lattice contraction and proper ionic size to fit into the interstitial sites support the validity of small ion incorporation for reducing defect formation [18,20]. Overall, the proposed mechanisms give a message that defect/electronic-trap engineering in both semiconductor films and interfaces is the key for efficient performance.

Besides the high efficiency, correlations between defects and photovoltaic performance should be addressed for achieving a long-term operational stability of solar cells under ambient environments. Normally, perovskite decomposition is preceded by its vulnerable properties to H_2O, and iodide-vacancy-mediated O_2^- formation accelerates the PbI_2 formation under photoexcitation [16,17]. The scaling behavior of perovskite stability improvement along the grain size increase proposes the necessity of grain growth and thereby defect reduction [17,28]. In addition to chemical reactions for defective micro-/nanostructures, the effects of light irradiance on electronic traps should be addressed considering the potential of defect and trap annihilation by photocarriers (e.g., decrease of nonradiative recombination under illumination) [29,30]. Also, interfacial charge accumulation (photocarriers and/or mobile ions) and consequent surface recombination are suggested to be considerable in determining a photovoltaic efficiency [31-33]. Potential defect formation which is mediated by accumulated charges and consequent irreversible chemical reactions at the interfaces further emphasizes the perception about the role of interfacial properties on both efficiency and stability [20,34]. Consequently, tracing the defect and trap variations is to be essential for establishing the correlations to the photovoltaic performance changes.

In chapter 2, the underlying factors for enabling efficient and stable performance of perovskite solar cells are studied through a simple thermal-annealing control of perovskites. $MAPbI_3$, $(FA_{0.83}MA_{0.17})Pb(I_{0.83}Br_{0.17})_3$, and $(Cs_{0.10}FA_{0.75}MA_{0.15})Pb(I_{0.85}Br_{0.15})_3$ perovskites (abbreviated as MA, FAMA, and CsFAMA, respectively) are examined based on the defect and microstructural differences, which have influences on photovoltaic performance including ion migration. Micro-/nanoscopic features are comprehensively analysed for the optoelectronic properties to unravel the origins that are directly correlated to the cell performance. Photoconductive noise microscopy is utilized to characterize the electronic traps of perovskite films, and the trapping/detrapping capacitance of solar cells are additionally analysed to understand the effects of trap states on photovoltaic parameters. It is revealed that CsFAMA has the lower number of shallow/deep-level electronic traps compared to MA and FAMA, via the analyses of $1/f$ noises and capacitances. Also, the change of V_{oc} is correlated to the variation of trap states during the shelf-life test for two months: FAMA and CsFAMA cells exhibiting negligible change of V_{oc} show trap-state shift toward the bandedge although the power-conversion efficiencies are clearly reduced. It is discussed on the origins that affect the solar-cell performance through the characterizations of both shallow/deep traps and mobile defects.

2.2. Experimental Methods

2.2.1. Perovskite Film Deposition

- $MAPbI_3$: Precursor is prepared by dissolving 1.2 M MAI (Greatcell Solar Limited, GSL) and 1.2 M PbI_2 (Tokyo Chemical Industry, TCI) in a mixture of *n*,*n*-dimethylformamide (Sigma-Aldrich) and dimethylsulfoxide (Sigma-Aldrich) with the volume ratio of 9:1 solution. Spin-coating is programmed as 1000 rpm for 10 s (ramp for 5 s) followed by 3000 rpm for 20 s (ramp for 1 s) with chlorobenzene (Sigma-Aldrich) drip of 300 μL at 5 s after the start of the second spin step.

- $(FA_{0.83}MA_{0.17})Pb(I_{0.83}Br_{0.17})_3$ and $(Cs_{0.10}FA_{0.75}MA_{0.15})Pb(I_{0.85}Br_{0.15})_3$: 1.0 M FAI (GSL), 1.0 M PbI_2, 0.2 M MABr (GSL), and 0.2 M $PbBr_2$ (TCI) are dissolved in the same solvent with the volume ratio of 4:1 solution. For Cs mixing, 0.7 M CsI (TCI) stock solution (volume ratio of 4:1) is added to the precursor of 1.0 M FAI, 1.1 M PbI_2, 0.2 M MABr, and 0.2 M $PbBr_2$, where 10% excess PbI_2 is used for stoichiometric composition. Same deposition condition is used except chlorobenzene drip at 5 s before the end of the second spin step.

All the precursors are used after the filtration by PTFE membrane filter (pore size: 500 nm). The annealing temperature is fixed to 100°C in a hot plate calibrated using a thermocouple, and the time is controlled between 1 and 60 min. Every procedure is performed in a N_2 glove box.

2.2.2. Solar Cell Fabrication

Conventional mesoporous TiO_2-based *n-i-p* structures are used. F:SnO_2 (FTO) (Wooyang GMS) is wet-cleaned under sonication in deionized water, acetone, isopropanol, and ethanol, and the substrate is used after UV-O_3 treatment for 15 min. TiO_2 blocking

layer is prepared by two steps: a compact layer is spin-coated using 150 and 300 mM solutions of titanium diisopropoxide *bis*(acetylacetonate) (Sigma-Aldrich) in 1-butanol (Sigma-Aldrich) at 2500 rpm for 20 s (ramp for 1 s). The substrate is dried after each coating step at 125°C for 20 min with 500°C for 30 min sintering at the last. A porous layer is spin-coated using diluted TiO_2 paste (30NR-D, GSL) of 150 mg/mL in anhydrous ethanol (Daejung) at 4000 rpm for 10 s (ramp for 2 s) followed by 500°C for 30-min annealing. The substrate is transferred into a glove box, and then perovskite and hole-transport layer are spin-coated. Hole-transport material is prepared by dissolving spiro-OMeTAD (Lumtec) in chlorobenzene of 72.3 mg/mL with the additives of 4-*tert*-butylpyridine (Sigma-Aldrich), bis(trifluoromethane)sulfonimide lithium salt (Sigma-Aldrich), and FK209 (GSL) (molar ratio of 1.00 : 3.33 : 0.54 : 0.10). An Au electrode is thermally evaporated, and active area for solar cell measurement is determined from the mask (0.09 cm^2).

2.2.3. Solar Cell Shelf-Life Test

The as-fabricated cells are stored under ambient laboratory conditions (24°C set with the average relative humidity of 50%) for stability test [35]. All cells are stored in the same dark box to prevent light-induced effects (e.g., halide segregation and phase separation) and to maintain the identical environmental conditions. Solar cells are measured and stored repetitively for several weeks. While the stability test using maximum power-point tracking is more realistic for the actual application, the unencapsulated cells under ambient test conditions degrade irreversibly in a few days, which is known to originate from H_2O and superoxide by photoexcitation, resulting in PbI_2 and byproducts [16,17]. In that sense, shelf-life test has merits in observing the

variations of cell parameters over a long term.

2.2.4. Dissolution of Hole-Transport Material

Prior to removing the hole-transport layer, the Au electrode is peeled-off using an ordinary tape (e.g., Kapton tape). The hole-transport layer is eliminated based on the reverse step of deposition, i.e., dipping the solar cell in chlorobenzene (20 mL) for 1-2 min at room temperature. Chlorobenzene is dried under N_2 gas flow and additional thermal treatment is excluded.

2.2.5. Characterization

The crystal structure is examined by x-ray diffraction (D8 Advance: Bruker), and film morphology is observed by using a field-emission scanning electron microscope (Merlin Compact: Zeiss). Its lateral grain size is analyzed using the electron microscopy images and ImageJ software. Surface chemical analyses are performed by x-ray photoelectron spectroscopy (Sigma probe: Thermofisher Scientific) without additional sputtering. An UV-visible spectrophotometer (V770: Jasco) is utilized with the integrating sphere, and absorption coefficient is determined from film absorptance (= 100% - reflectance - transmittance), where perovskite is deposited on mesoporous TiO_2/FTO. Steady-state and time-resolved photoluminescence spectra (LabRAM HR Evolution: Horiba, FL920: Edinburgh Instruments, respectively) are measured using $\lambda_{excitation}$ = 514 and 472.4 nm lasers, respectively. For photoluminescence, perovskite is deposited on a glass substrate (Eagle XG: Corning).

A photoconductive noise microscopy method is utilized to obtain photocurrent and noise maps showing the spatial distribution of photocurrents and electrical noises in the perovskite films, as our previous report [36]. Briefly, a perovskite film is deposited on

compact TiO_2/FTO. Then, the FTO substrate is grounded, and the short-circuit photocurrent through the nanoscale conducting probe (which is directly contacted to the film surface) is measured (illumination of 100 mW/cm^2). By scanning the probe over the film surface during the measurement, spatial map of photocurrent generation is obtained. In addition, the current-noise power spectral density (PSD) could be imaged via the photoconductive noise microscopy, applying a bias of 0.4 V between the FTO and the conducting probe under dark. A topography map could be obtained simultaneously with the photocurrent and noise maps [36]. Image processing for grain boundary elimination in photocurrent and noise maps is based on the edge detection using Sobel method in MATLAB with modification for clear distinction among domains. Besides electron image analyses for grain size determination, grain size is additionally confirmed using image processing tools after grain boundary elimination. For photocurrent and noise determination in each grain, values are averaged over all the pixels in each grain which are enclosed by grain boundaries detected in Sobel method. Photocurrent density-voltage (*J-V*) curves are obtained by the solar cell measurement system (K3000: McScience) with a solar simulator (Xenon lamp, air mass 1.5 at 100 mW/cm^2). *J-V* is obtained under the scan rate of 100 mV/s (unless otherwise noted) in the voltage between -0.1 V and 1.2 V without preconditioning of bias and light. External quantum efficiency is measured using incident-to-photon conversion efficiency system (K3100: McScience). Impedance is measured using a potentiostat (Zive SP1: WonATech) in the frequency range between 10 mHz and 100 kHz with an AC amplitude of 10 mV under dark. Prior to the impedance measurement, solar cells are fully relaxed under dark and short-circuit conditions until the voltage drops under a few millivolt [37].

2.3. Results and Discussion

2.3.1. Solar Cell Performance (Efficiency and Stability)

Based on the improved optoelectronic and photovoltaic properties via micron-sized perovskite grains, thermal annealing is chosen over the variables for the grain growth (e.g., intermediate phase control, hydrophobicity control of substrate, etc.[10,12,13]), while preventing the mediation of other factors such as decomposition, pin-hole formation, and roughness changes. Solar cells are compared between $MAPbI_3$ (MA), $(FA_{0.83}MA_{0.17})Pb(I_{0.83}Br_{0.17})_3$ (FAMA), and $(Cs_{0.10}FA_{0.75}MA_{0.15})Pb(I_{0.85}Br_{0.15})_3$ (CsFAMA), and *J-V* curves from different annealing are plotted in Figs. 2-1 and 2-2 (photovoltaic parameters in Table 2-1).

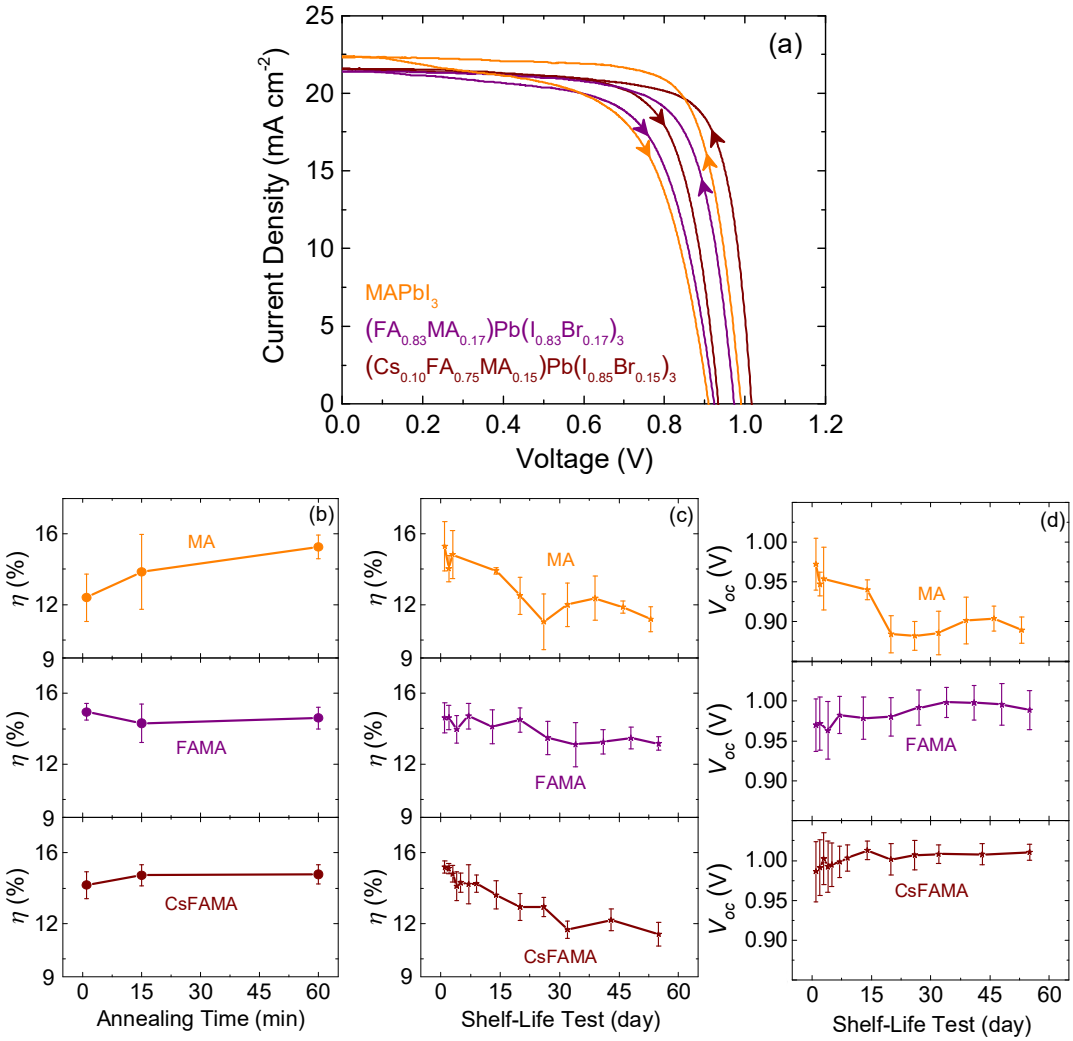

Fig. 2-1. (Color) Photovoltaic performance with compositional and thermal-annealing controls. (a) Best solar cells in $MAPbI_3$ (≡ MA), $(FA_{0.83}MA_{0.17})Pb(I_{0.83}Br_{0.17})_3$ (≡ FAMA), and $(Cs_{0.10}FA_{0.75}MA_{0.15})Pb(I_{0.85}Br_{0.15})_3$ (≡ CsFAMA), with 60-min annealing at 100°C. (b) Annealing effect on the power-conversion efficiency (η). Variations of (c) η and (d) open-circuit voltage (V_{oc}) during the cell stability test.

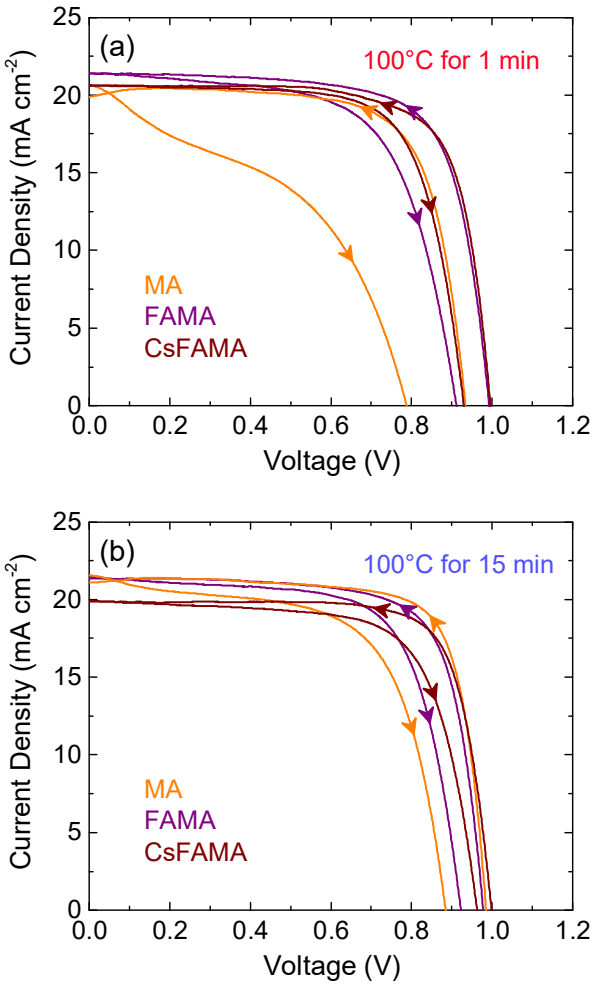

Fig. 2-2. (Color) Best cell performance at different thermal annealing time. *J-V* of $MAPbI_3$, $(FA_{0.83}MA_{0.17})Pb(I_{0.83}Br_{0.17})_3$, and $(Cs_{0.10}FA_{0.75}MA_{0.15})Pb(I_{0.85}Br_{0.15})_3$ solar cells at annealing time of perovskite for (a) 1 min and (b) 15 min. Arrows indicate the voltage scan directions at the 100 mV/s rate.

(a) **100°C for 1 min**	J_{sc} **(mA cm^{-2})**	V_{oc} **(V)**	***FF*** **(%)**	η **(%)**
MA (*For*)	20.6	0.789	43.4	7.1
MA (*Rev*)	19.9	0.935	73.2	13.6
FAMA (*For*)	21.4	0.912	64.1	12.5
FAMA (*Rev*)	21.4	0.994	72.0	15.3
CsFAMA (*For*)	20.6	0.931	71.1	13.7
CsFAMA (*Rev*)	20.6	0.997	73.7	15.1

(b) **100°C for 15 min**	J_{sc} **(mA cm^{-2})**	V_{oc} **(V)**	***FF*** **(%)**	η **(%)**
MA (*For*)	21.5	0.886	62.8	12.0
MA (*Rev*)	21.1	0.986	77.2	16.1
FAMA (*For*)	21.4	0.924	68.9	13.6
FAMA (*Rev*)	21.3	0.979	73.7	15.4
CsFAMA (*For*)	19.9	0.964	69.7	13.4
CsFAMA (*Rev*)	19.9	1.000	76.6	15.2

(c) **100°C for 60 min**	J_{sc} **(mA cm^{-2})**	V_{oc} **(V)**	***FF*** **(%)**	η **(%)**
MA (*For*)	22.4	0.911	62.6	12.8
MA (*Rev*)	22.3	0.991	76.3	16.8
FAMA (*For*)	21.4	0.924	67.4	13.3
FAMA (*Rev*)	21.4	0.974	73.4	15.3
CsFAMA (*For*)	21.6	0.935	72.5	14.6
CsFAMA (*Rev*)	21.6	1.017	76.4	16.8

Table 2-1. Best cell parameters at each perovskite condition. Short-circuit current density (J_{sc}), open-circuit voltage (V_{oc}), fill factor (*FF*), and power conversion efficiency (η) of solar cells displayed in Figs. 2-1(a) and 2-2. Thermal-annealing condition of (a) 100°C for 1 min, (b) 15 min, and (c) 60 min, respectively. Forward scan direction is denoted as '*For*', and reverse as '*Rev*', respectively.

For MA cells, annealing results in η improvement with the gradual increase of both V_{oc} and J_{sc} (Fig. 2-1(b) and details in Fig. 2-3). The general trend of annealing dependence is consistent to that of the best-performing cells (Table 2-1). For both FAMA and CsFAMA cells (Figs. 2-1(b), 2-4, and 2-5), annealing has a negligible impact on the photovoltaic performance. While the annealing causes minute changes, η is distinguished between the composition of $FAPbI_3$ structure, and η is increased through Cs incorporation due to the rise of both V_{oc} and FF. However, J_{sc} is minutely decreased compared to MA (by ~1 mA/cm^2), and it is again confirmed from external quantum efficiency (EQE) in Fig. 2-6. Even considering the blue-shift of bandgap energy for (Cs)FAMA than MA, J_{sc} of ~23 mA/cm^2 is commonly obtained in the state-of-the-art devices, and it necessitates the compositional optimization (less than 10% of Cs mixing for high-performance [5,21]). In the aspect of efficiency discrepancy between scan directions (hysteresis), this gap is reduced as annealing for MA, and CsFAMA shows the smallest discrepancy (Table 2-1). For example, hysteresis-effect index which is defined based on the difference between J_{Rev} and J_{For} at around maximum power-point ('*Rev*' and '*For*' for the reverse and forward scan directions, respectively) demonstrates that hysteresis is reduced as MA (1 min) → MA (15 min) → MA (60 min) → FAMA → CsFAMA [38]. (Cs)FAMA has $\{V_{oc}^{Rev} - V_{oc}^{For}\} < 100$ mV, while MA shows ~150 mV with reaching 30% FF difference for the 1-min annealing. The hysteresis-effect index determined from various J-V scans are summarized in Fig. 2-7(a), and consistently, CsFAMA shows the reliable η while MA exhibits large disparities over the scan directions. In short, CsFAMA cells exhibit the highest η along with the decrease of hysteresis, and MA cells are more sensitively dependent on the annealing than others. FAMA cells result in lower η than CsFAMA with negligible dependence on annealing as similar to CsFAMA.

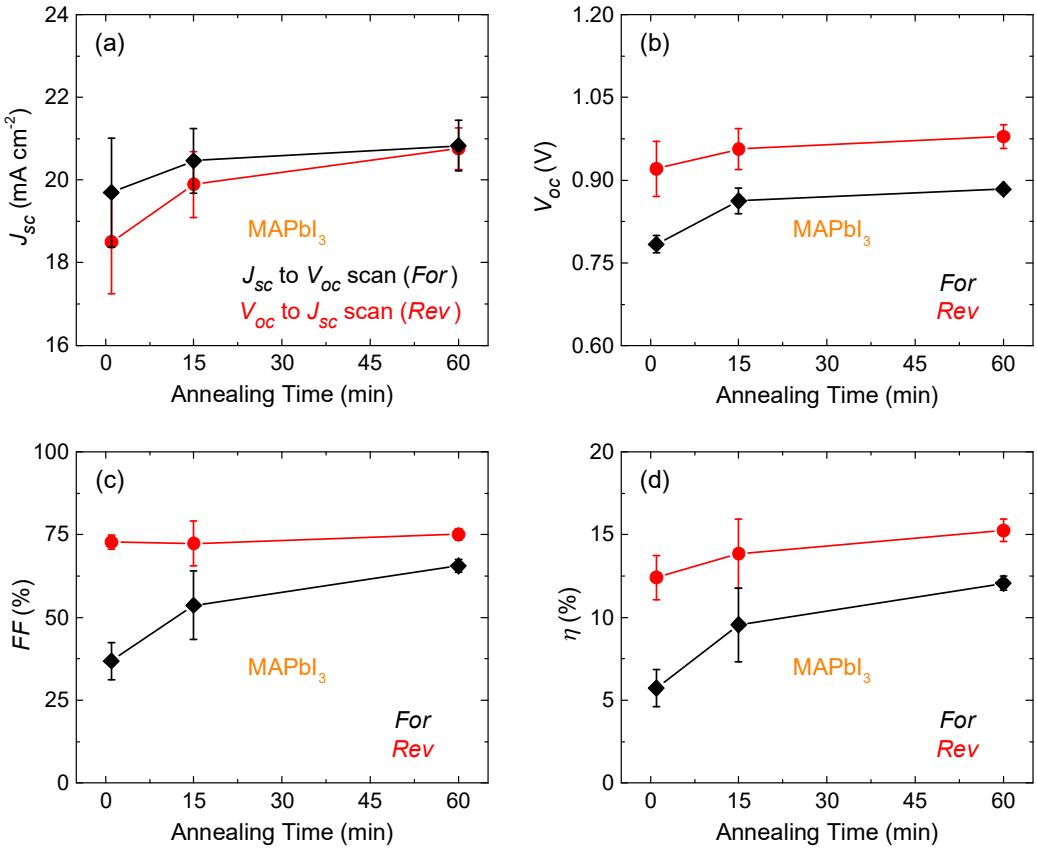

Fig. 2-3. (Color) General trend of $MAPbI_3$ cell parameters on annealing time (at 100°C). (a) J_{sc}, (b) V_{oc}, (c) *FF*, and (d) η.

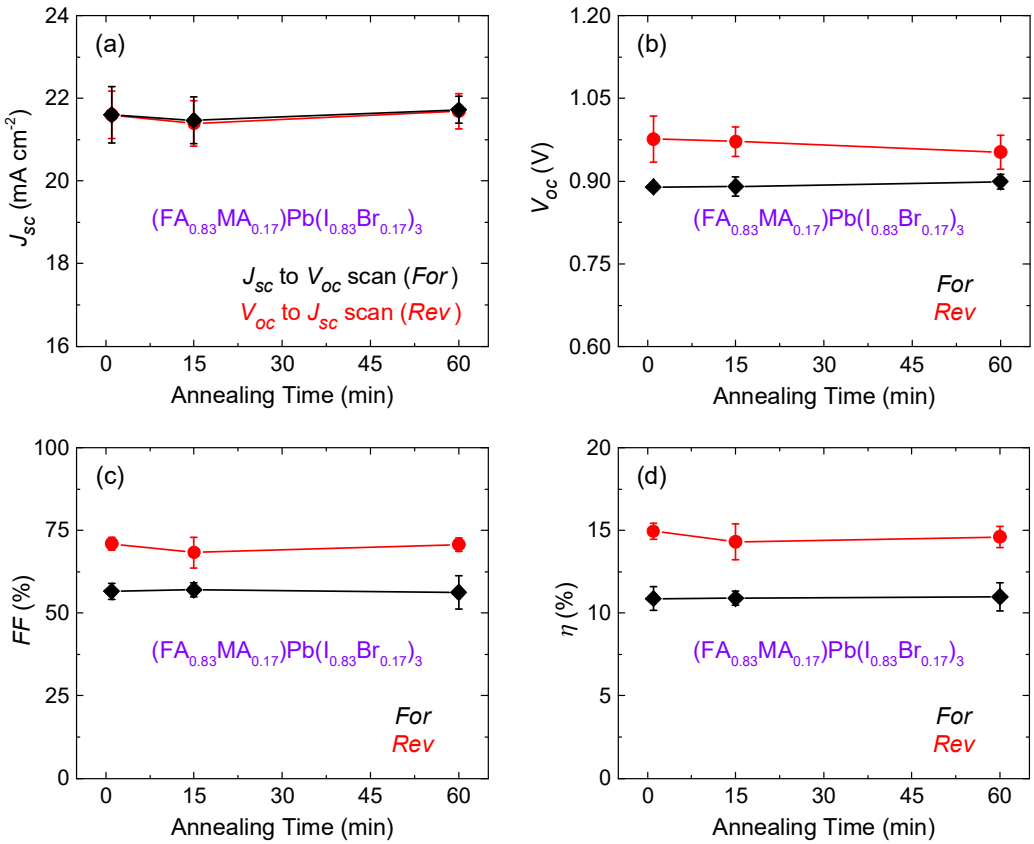

Fig. 2-4. (Color) General trend of $(FA_{0.83}MA_{0.17})Pb(I_{0.83}Br_{0.17})_3$ cell parameters on annealing time (at 100°C). (a) J_{sc}, (b) V_{oc}, (c) *FF*, and (d) η.

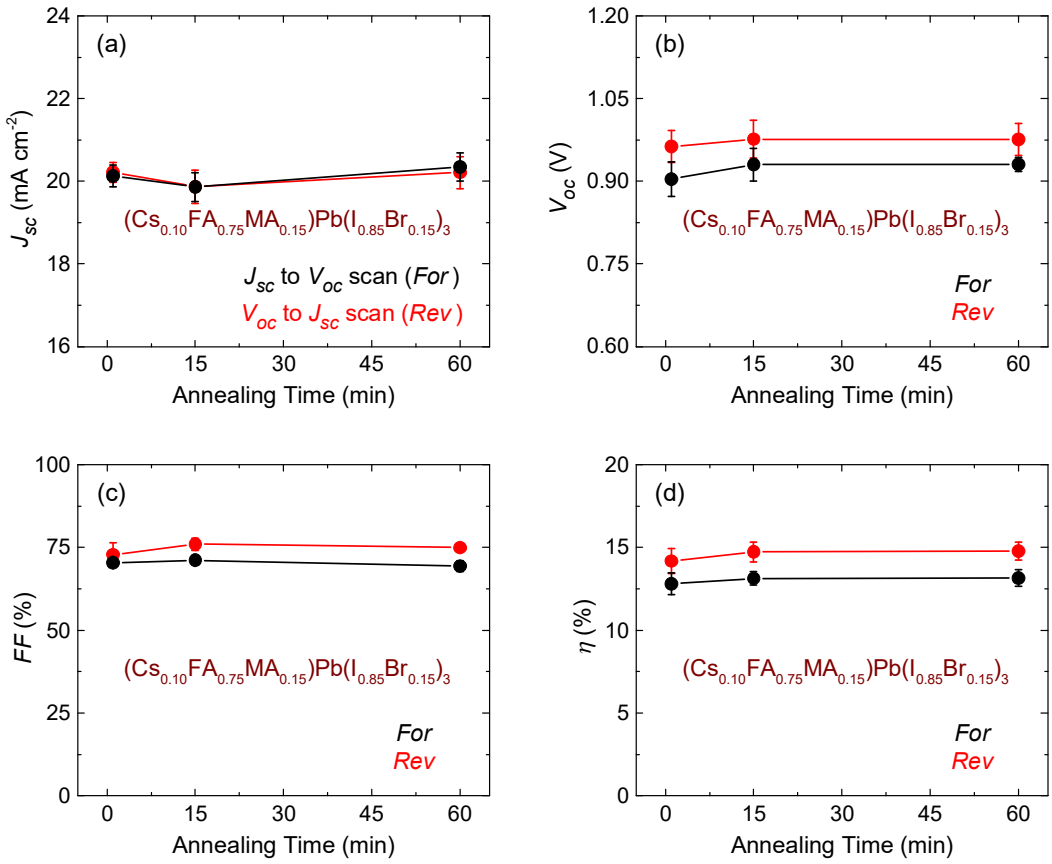

Fig. 2-5. (Color) General trend of $(Cs_{0.10}FA_{0.75}MA_{0.15})Pb(I_{0.85}Br_{0.15})_3$ cell parameters on annealing time (at 100°C). (a) J_{sc}, (b) V_{oc}, (c) *FF*, and (d) η.

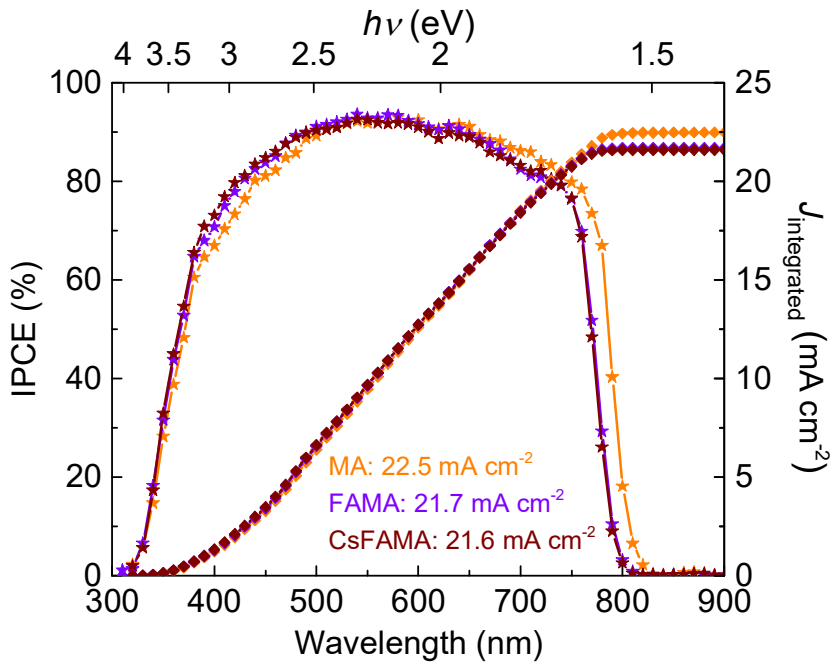

Fig. 2-6. (Color) Incident photon-to-current conversion efficiency of solar cells. $MAPbI_3$, $(FA_{0.83}MA_{0.17})Pb(I_{0.83}Br_{0.17})_3$, and $(Cs_{0.10}FA_{0.75}MA_{0.15})Pb(I_{0.85}Br_{0.15})_3$ cells with the integrated current density values in the inset. Annealing is the same as 60 min.

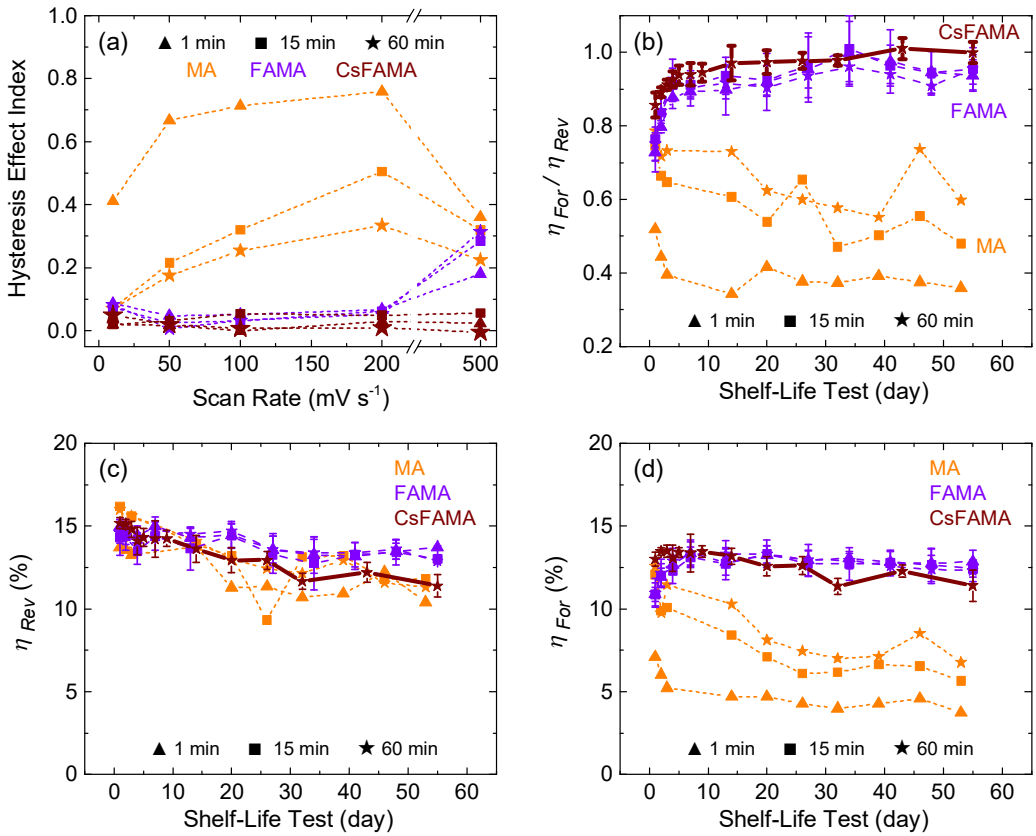

Fig. 2-7. (Color) Degree of hysteresis and shelf-life test. (a) Scan-rate dependent hysteresis-effect index, which is defined based on the difference between J_{Rev} and J_{For} at 0.8 V_{oc}. Best-performing cells are selected to test the scan-rate dependency. (b) Variation of the degree of hysteresis during shelf-life test. The ratio of η_{For} over η_{Rev} shows very similar tendency to the hysteresis-effect index. For both $MAPbI_3$ and $(FA_{0.83}MA_{0.17})Pb(I_{0.83}Br_{0.17})_3$ cells, annealing (for 1, 15, and 60 min) is controlled, while $(Cs_{0.10}FA_{0.75}MA_{0.15})Pb(I_{0.85}Br_{0.15})_3$ is fixed to 60-min annealing. (c) and (d) Actual values of η_{Rev} and η_{For}.

Besides the cell efficiency, its stability is analyzed through the shelf-life test (Fig. 2-1(c)). Variations of J_{sc}, V_{oc} and FF are summarized in Figs. 2-7 and 2-8. All the solar cells experience similar degradation of η_{Rev}, irrespective of compositions (Fig. 2-1(c)). While η_{For} is maintained for (Cs)FAMA, MA shows steep degradation (Fig. 2-7). The drastic change of η_{For} is due to FF, and effects of other parameters can be compared through Fig. 2-8. Interestingly, η of CsFAMA becomes independent of scans, and η_{For}/η_{Rev} ratio increases with approaching to unity as storage (cell aging), which is remarkably different to MA where the ratio drops (i.e., falling below 0.6). Also, V_{oc} is negligibly changed for (Cs)FAMA (even slightly increased) during the stability test, while MA shows clear V_{oc} degradation as compared in Fig. 2-1(d). In summary, similar degradation of a cell efficiency is observed for all the compositions, however, both FAMA and CsFAMA cells keep approximately constant V_{oc}, instead of decrease in MA cells.

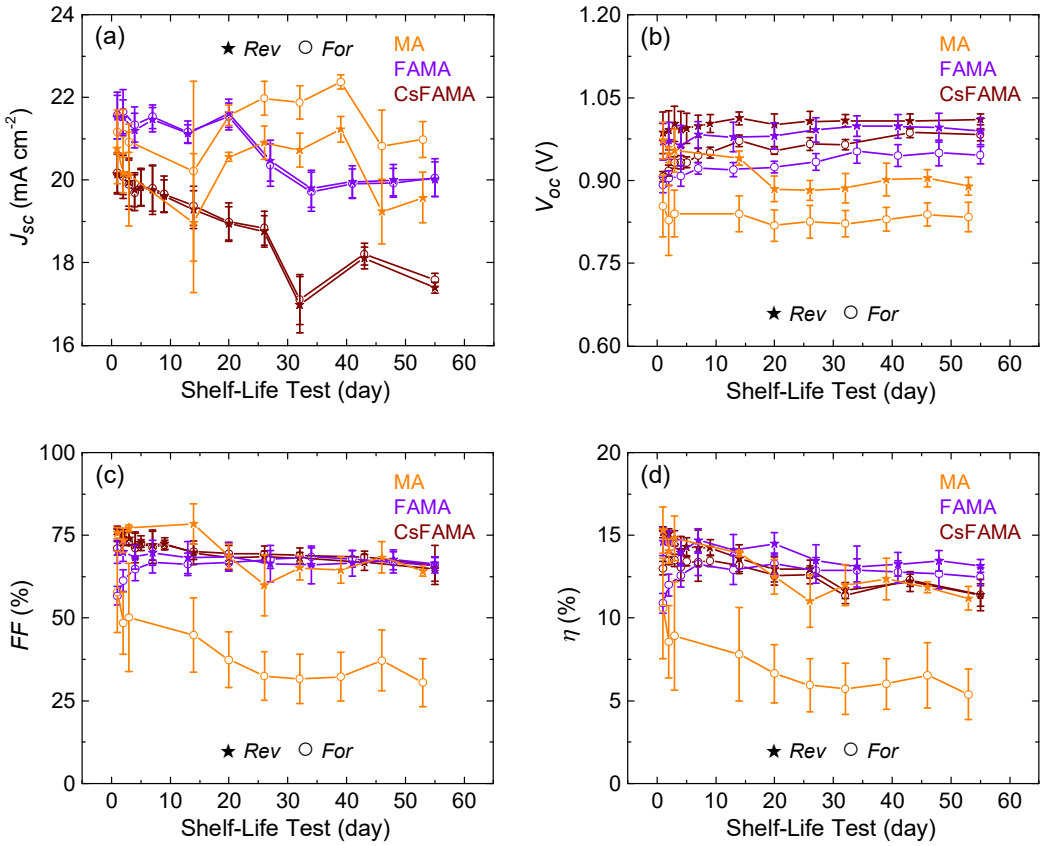

Fig. 2-8. (Color) Variation of cell parameters during shelf-life test. (a) J_{sc}, (b) V_{oc}, (c) FF, and (d) η of $MAPbI_3$, $(FA_{0.83}MA_{0.17})Pb(I_{0.83}Br_{0.17})_3$, and $(Cs_{0.10}FA_{0.75}MA_{0.15})Pb(I_{0.85}Br_{0.15})_3$ cells. Photovoltaic parameters are averaged irrespective of the annealing time at each composition.

2.3.2. Film Properties / Nanoscale Photocurrent and Shallow Electronic Traps (Noise)

To scrutinize the annealing effects, microstructural, optical, and optoelectronic properties are examined to analyze the factors differentiating the cell performance. Film morphologies and grain sizes are characterized as shown in Fig. 2-9. We have observed the gradual increase of grain size during the annealing process, and therefore data of two distinct conditions (1 and 60 min) are arranged. Prolonged annealing is limited to prevent the irreversible degradation of perovskite into PbI_2. The prerequisite of complete coverage is satisfied, and size analyses demonstrate the normal grain growth (unimodal distribution of grain sizes). Also, diffraction (Figs. 2-10 (a) and (b)) exhibits negligible crystalline impurities. Notably, grain growth is significant for MA, while minute for both FAMA and CsFAMA. Micron-sized grains are observed which are larger than the film thickness of 400-500 nm, and abnormal grain growth is frequently observed in MA with preferable orientation along [110] [10,39]. Instead, grain sizes are smaller in both FAMA and CsFAMA probably due to the specimen thickness effect [40]. At least, the absence of both preferable orientation and impurities (e.g., Zener pinning at grain boundary) involves that causes for different growths lie elsewhere such as grain-boundary mobility, grooving, and substrate chemistry [41].

Diffraction data measured in solar cell are compared in Fig. 2-10(c). It is analyzed based on the cells which have experienced the repetitive measurements for up to ~3 months. An Au electrode is indexed, and reflection from spiro-OMeTAD is absent due to the steric hindrance for crystallization. Markedly, both PbI_2 and hydrated perovskite are negligible, which are the products of the atmospheric degradation. Minute formation of δ-$FAPbI_3$

and PbI_2 in FAMA is rather originated from the composition where Cs addition results in high quality films. Also, peak broadening in diffraction is analyzed for the nonuniform distribution of local strains, where double peak Lorentzian function is used for fitting the full width at half maximum (Δk), considering the effect of Cu $K\alpha_1$ and $K\alpha_2$ (the scattering vector $k = (4\pi/\lambda) \sin \theta$) as shown in Figs. 2-10(d-f). The narrower peaks of MA than (Cs)FAMA are in line with the larger grains in Fig. 2-9, and local strains do not correlate to the cell performance.

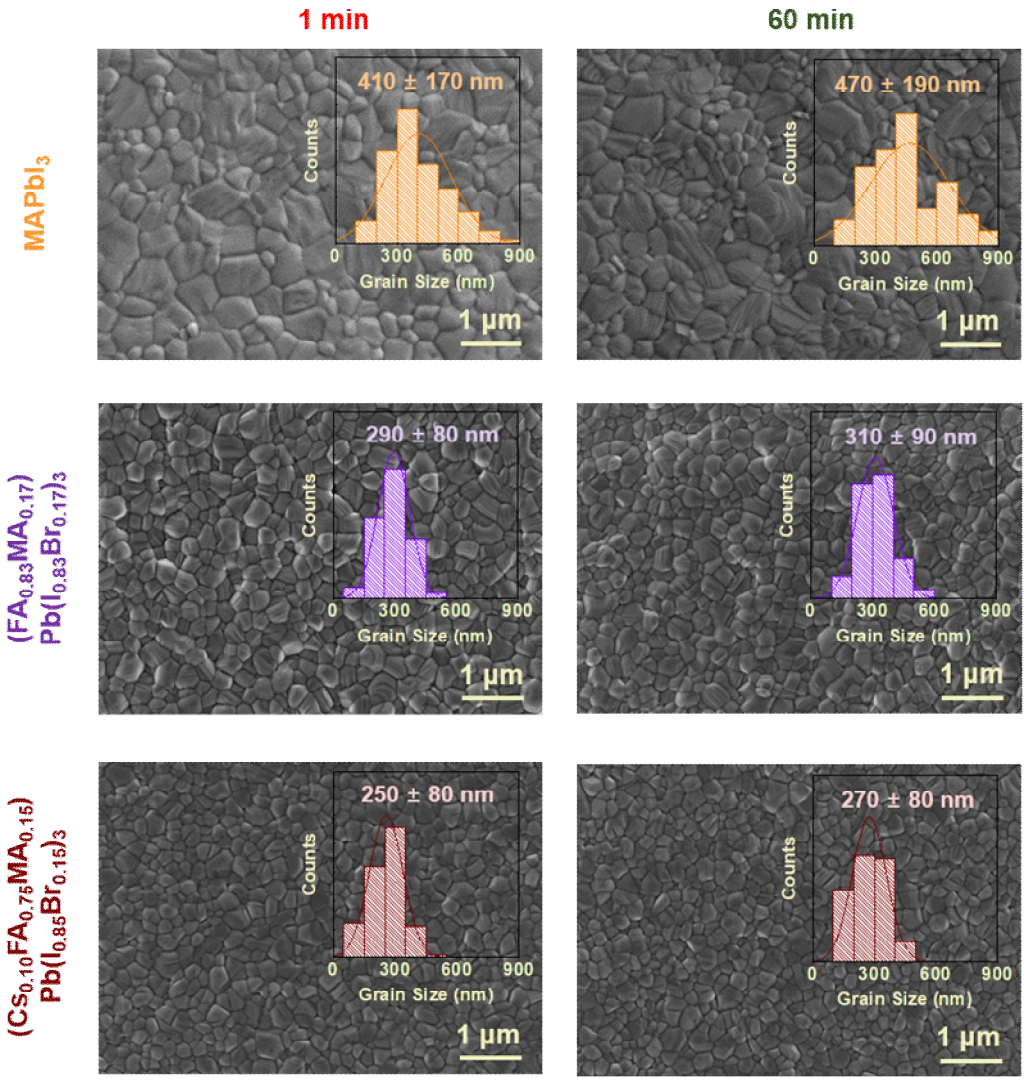

Fig. 2-9. (Color) Grain size analyses. Scanning electron microscopy image of each perovskite surface with the inset of grain-size distribution (normal distribution curve with the column width of 100 nm).

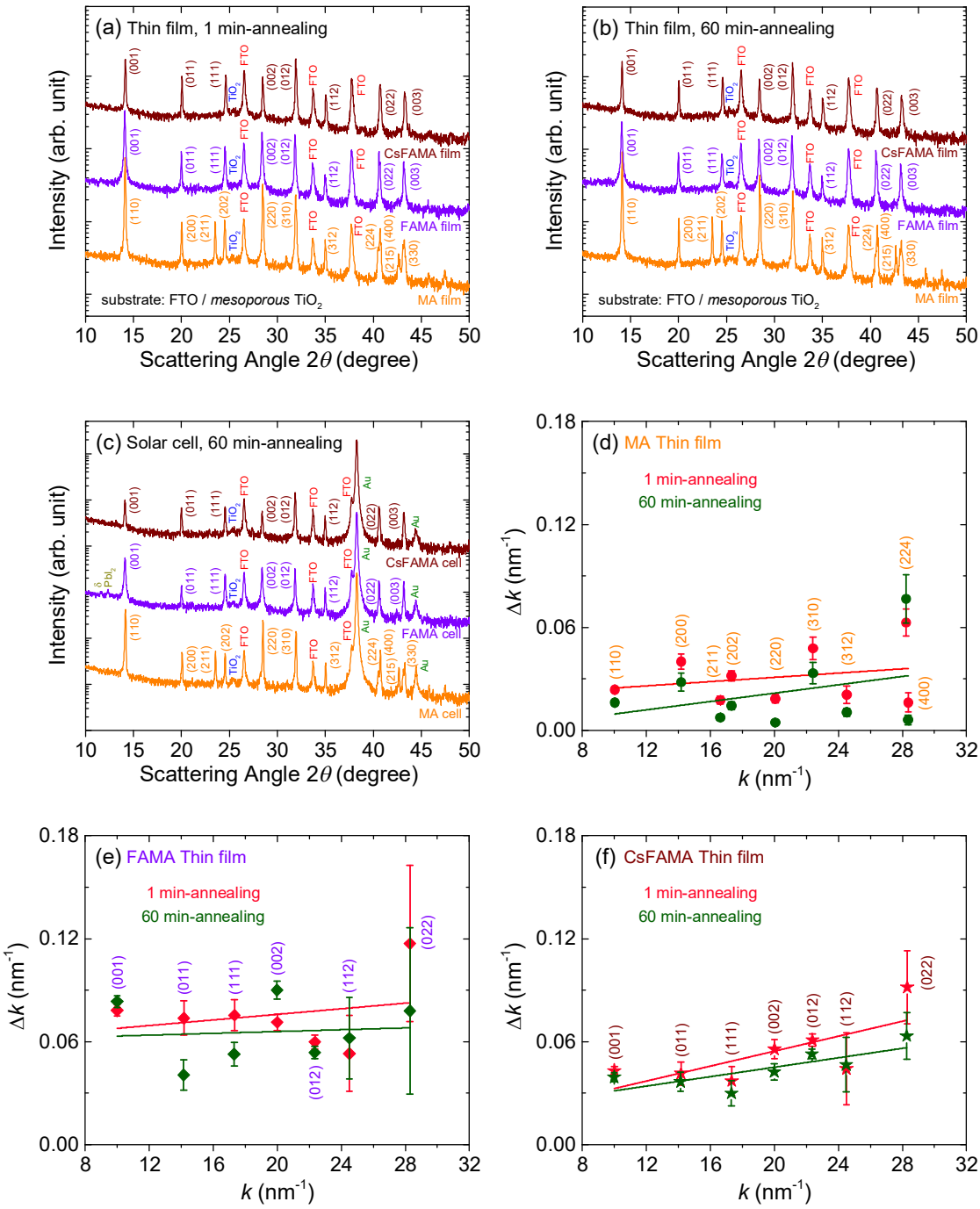
(a) Thin film, 1 min-annealing
(b) Thin film, 60 min-annealing
(c) Solar cell, 60 min-annealing
(d) MA Thin film
(e) FAMA Thin film
(f) CsFAMA Thin film
1 min-annealing
60 min-annealing
CsFAMA film
FAMA film
MA film
CsFAMA cell
FAMA cell
MA cell
substrate: FTO / mesoporous TiO2
Intensity (arb. unit)
Scattering Angle 2θ (degree)
Δk (nm-1)
k (nm-1)

Fig. 2-10. (Color) X-ray diffraction characterization of perovskite thin films and solar cells. Diffraction of (a) 1-min-annealed and (b) 60-min-annealed perovskite thin films. (c) Solar cells after the shelf-life test of more than 1 month from the cell fabrication date. Peaks are indexed following the crystalline structure of tetragonal $MAPbI_3$ and cubic α-$FAPbI_3$, while δ is hexagonal $FAPbI_3$. (d-f) The slopes for the determination of nonuniform distribution of local strains, for the MA, FAMA, and CsFAMA films, respectively.

Both microstructural and atomistic phenomena cause the materials and cell degradation. The scaling behavior of materials stability with the $MAPbI_3$ grain size and iodide-vacancy-mediated degradation under light/O_2 are verified [17,28]. Monohydrate perovskite which acts as an insulating layer is known to be reversibly formed at grain boundaries through the reaction with H_2O, and O_2 is known to adsorb on the grain boundaries causing electrical doping [16,42]. Compositional redistribution of perovskite and interfacial changes at the charge-selective contacts demonstrates the entangled origins for the cell degradation [43]. Therefore, nanoscopic characterizations are further utilized for the trap analyses to understand the degradation behavior of η (with V_{oc}, J_{sc} and FF).

Absorption coefficient and photoluminescence (PL) data are first compared in Fig. 2-11. The blue-shift of absorption onset for both FAMA and CsFAMA than MA is consistent with EQE spectra (Fig. 2-6), and absorption coefficients are similar in the range of ~10^4 cm^{-1}. The absorption tail is fitted using an exponential function, and the large Urbach energy herein is due to the reflection which overestimates the absorption below bandgap energy [44]. The measured PL peak energy is consistent to the bandgap energy determined from the Tauc plot, and peak broadening dominated by phonon scattering (related to charge mobility) is decreased for CsFAMA compared to FAMA and also MA, respectively [45].

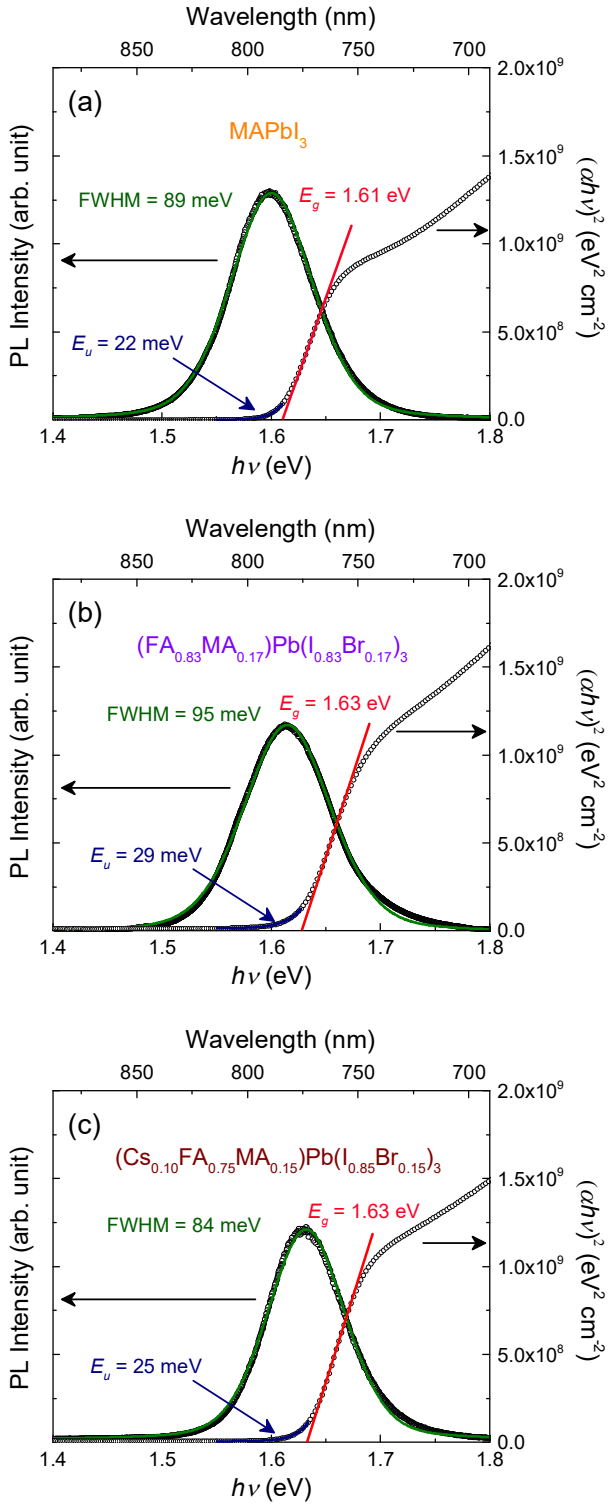
Wavelength (nm)
850
800
750
700
(a)
MAPbI3
FWHM = 89 meV
Eg = 1.61 eV
Eu = 22 meV
PL Intensity (arb. unit)
(αhν)² (eV² cm⁻²)
2.0x10⁹
1.5x10⁹
1.0x10⁹
5.0x10⁸
0.0
1.4
1.5
1.6
1.7
1.8
hν (eV)
(b)
(FA0.83MA0.17)Pb(I0.83Br0.17)3
FWHM = 95 meV
Eg = 1.63 eV
Eu = 29 meV
(c)
(Cs0.10FA0.75MA0.15)Pb(I0.85Br0.15)3
FWHM = 84 meV
Eg = 1.63 eV
Eu = 25 meV

Fig. 2-11. (Color) Optical properties of $MAPbI_3$, $(FA_{0.83}MA_{0.17})Pb(I_{0.83}Br_{0.17})_3$, and $(Cs_{0.10}FA_{0.75}MA_{0.15})Pb(I_{0.85}Br_{0.15})_3$. Absorption coefficient and photoluminescence (PL) spectrum of (a) $MAPbI_3$, (b) $(FA_{0.83}MA_{0.17})Pb(I_{0.83}Br_{0.17})_3$, and (c) $(Cs_{0.10}FA_{0.75}MA_{0.15})Pb(I_{0.85}Br_{0.15})_3$ with bandgap energy (E_g), Urbach energy (E_u), and PL broadening (full-width at half-maximum) values. Black symbols are the raw data, and color lines are the fitting results of E_g (red), E_u (blue), and FWHM (green), respectively.

Photoconductive noise microscopy based on the conductive atomic force microscopy (*c*AFM) is utilized to characterize the localized photocurrents and shallow electronic traps [46,47]. The photocurrent and current-normalized noise power spectral density (PSD) of FAMA and CsFAMA films are compared in Fig. 2-12. And, the data for MA case were provided in our previous work [36]. Topography with the comparison of root-mean-square roughness (σ_{rms}) demonstrates more smooth surface by Cs incorporation (Figs. 2-13 (a) and (b)). Grain-by-grain photocurrent is distinguished by higher photocurrents at grain boundaries (Fig. 2-12(a)). The frequency spectrum of current-noise PSD shows $1/f$ behavior (Fig. 2-13(c)), and the PSD magnitude can be used to quantify the effective trap densities existing along the current paths [36]. Generally, grains having higher photocurrent exhibit lower noise PSD in both FAMA and CsFAMA (Fig. 2-12(b)). Photocurrent and noise maps are further analyzed after the elimination of grain boundary (Fig. 2-14), and this elimination simplifies the PSD arguments by excluding grain boundary characters such as band bending, thermal grooving, chemical/physical inhomogeneity, etc. [48,49]. Interestingly, the scatter plot of grain size vs. photocurrent shows that photocurrent is increased by Cs addition (~20% enhancement) rather than scaled up along the grain size (Fig. 2-12(c)). Also, higher photocurrent at CsFAMA than FAMA is observed in short-annealing conditions (Fig. 2-14). Considering the minute decrease of charge mobility by Cs doping in FAMA, photocurrent improvement could be related to the increase of photocarrier density which is determined by the reduced carrier recombination [21]. In addition, broad photocurrent distribution (inhomogeneity) over grains (Fig. 2-14(a)) is diminished with the reduction of average photocurrent as annealing time increases, and mobility change due to the solute scattering may contribute to the photocurrent (Figs. 2-14(a), (b) and (c)).

Trap-mediated recombination is the dominant mechanism under illumination, and effective trap densities are deduced from noise PSD. The relationship between photocurrents and effective trap densities in Figs. 2-12(d) and 2-14(c) shows inverse proportionality. For CsFAMA, lower trap densities are observed in addition to the higher photocurrents than FAMA. The carrier number fluctuations causing electrical noises in perovskite are expected to originate from the shallow traps which result in trapping-detrapping or recombination into deeper states [50]. In that sense, high photocurrents and low trap densities in CsFAMA are in accordance of the reduction for shallow traps with recombination. Regarding the perovskite formation, solvent for perovskite precursor relies on strongly-coordinating molecules having high electronegative elements such as -C=S-, -S=O-, and -C=O- [10]. Strong interactions between solvent molecules and organic/inorganic precursors result in molecule-intercalated intermediate phases and also the inverse solubility behavior with respect to a temperature change [51]. The evaporation of molecules during annealing may cause the non-stoichiometric composition leading to point defects that post-treatment using constituent elements results in some passivation and electrical doping [17,52]. Even though the grain sizes are smaller for both FAMA and CsFAMA compared to MA, the defect/trap reduction plays a crucial role in improving the photovoltaic performance.

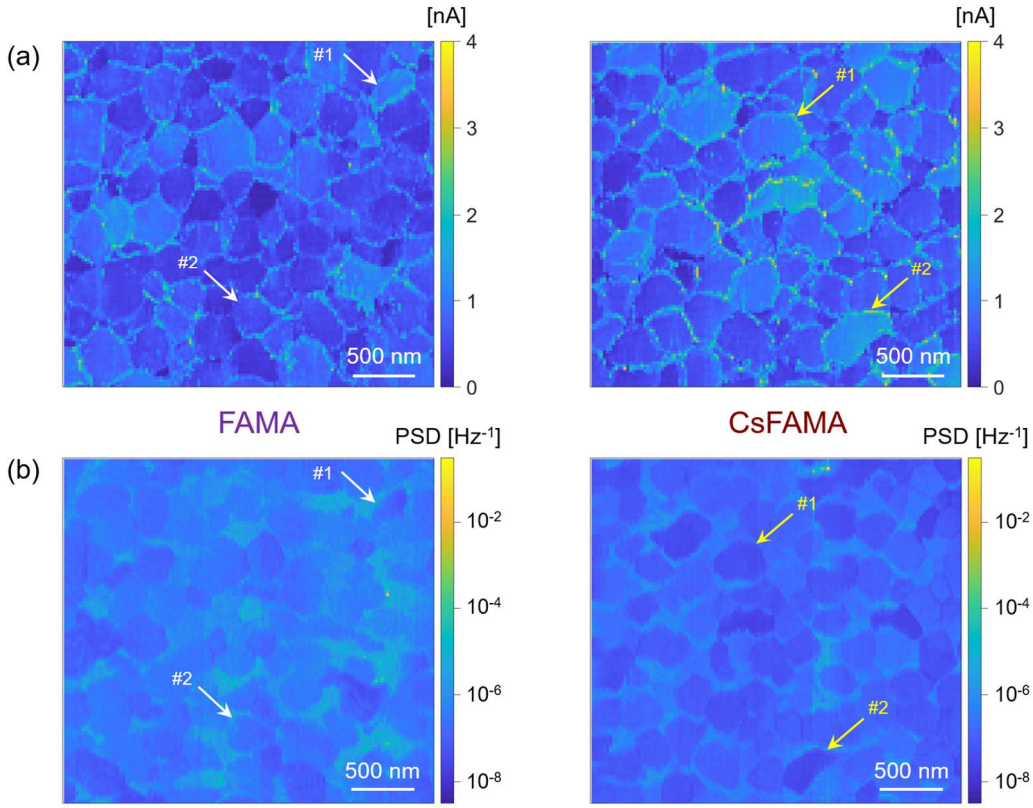

Fig. 2-12. (Color) Localized photocurrent (I_{sc}) and electrical noise via photoconductive noise microscopy. (a) Nanoscale I_{sc} map. (b) Current-normalized noise power spectral density (PSD) at 140 Hz of $1/f$ noise. For photoconductive distribution, current mapping is performed under illumination (100 mW/cm^2 of white light) and short-circuit condition. For noise (PSD), tip is biased at 0.4 V under dark in FTO-TiO_2-perovskite-Pt tip structure. The numbered arrow in I_{sc} and noise map indicates each identical grain.

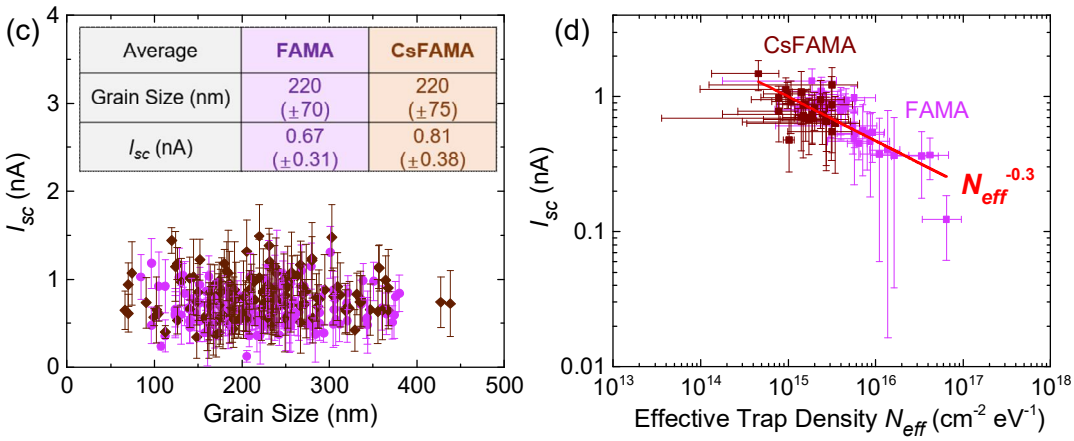

Fig. 2-12. (Color) (Continued) (c) Variations of I_{sc} vs. grain size. (d) I_{sc} vs. effective trap density (N_{eff}) where N_{eff} is proportional to the current-normalized noise PSD, originating from the tail-state traps by a single relaxation in each trap.

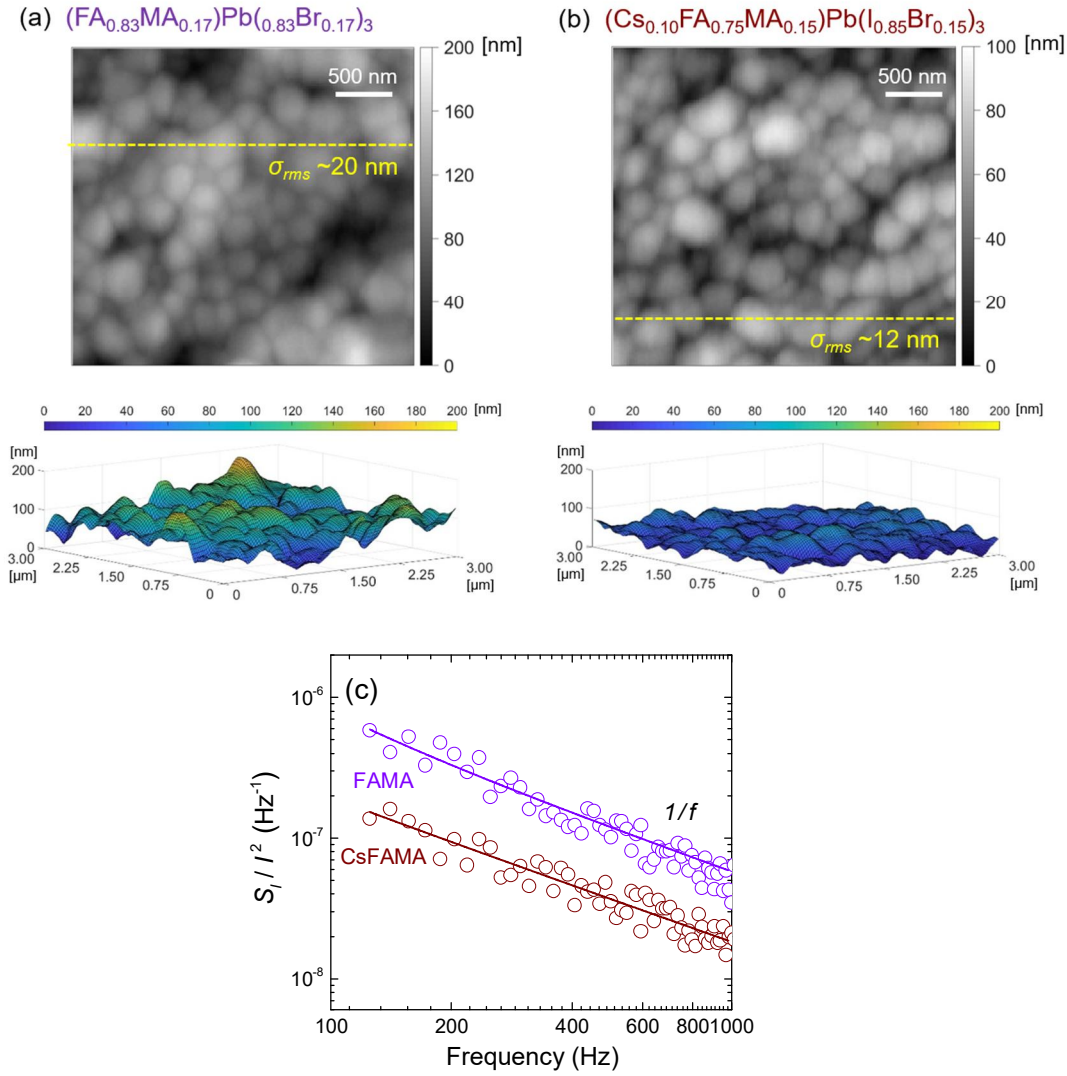

Fig. 2-13. (Color) Topography of perovskite film and frequency spectrum of noise PSD. (a) $(FA_{0.83}MA_{0.17})Pb(I_{0.83}Br_{0.17})_3$ and (b) $(Cs_{0.10}FA_{0.75}MA_{0.15})Pb(I_{0.85}Br_{0.15})_3$ films. Bottom is the 3D plot for comparison. Vertical roughness σ_{rms} is from the yellow line. (c) Comparison of current-normalized noise PSD (S_I / I^2) spectrum of perovskite film in Fig. 2-12. Scatter plot is the raw data and the straight line is the fitting (1/*f* behavior).

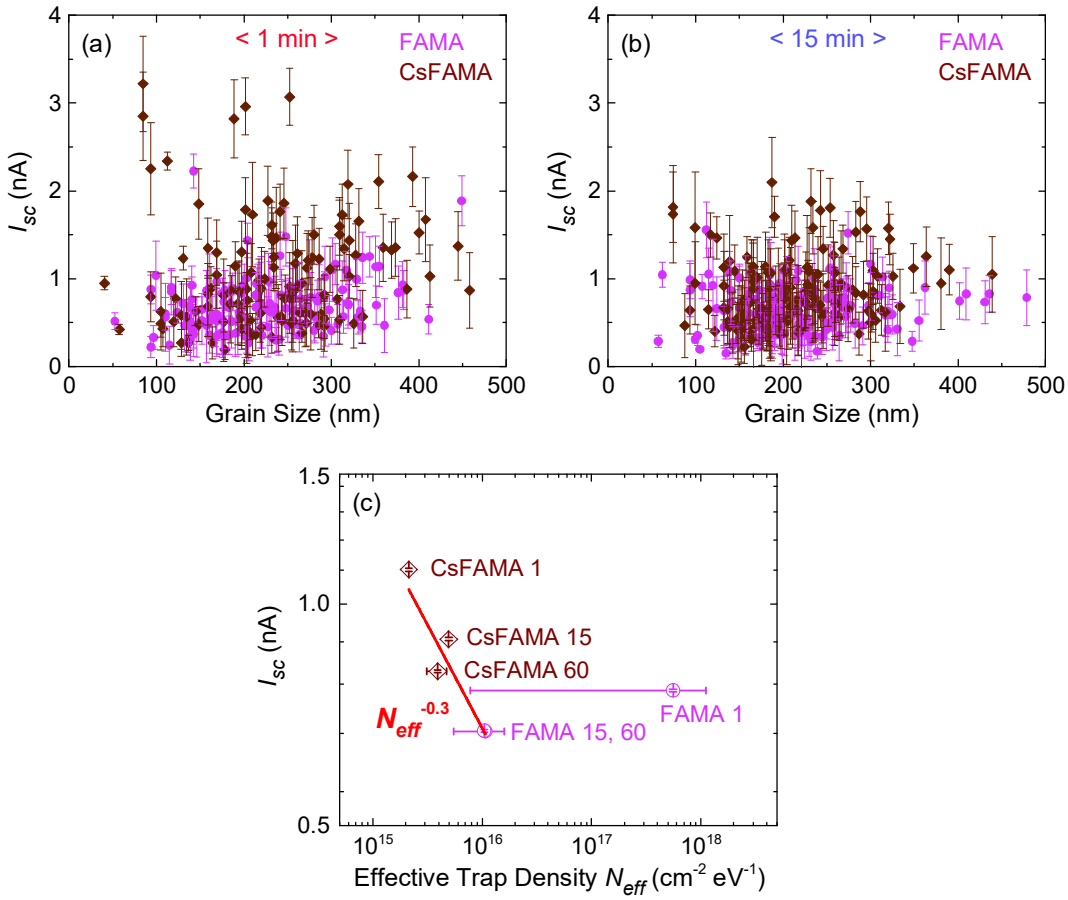

Fig. 2-14. (Color) Annealing effect on photocurrent/noise and image processing of raw data. Scatter plot of photocurrent (I_{sc}) and grain size for the annealing of (a) 1 min and (b) 15 min at $(FA_{0.83}MA_{0.17})Pb(I_{0.83}Br_{0.17})_3$ and $(Cs_{0.10}FA_{0.75}MA_{0.15})Pb(I_{0.85}Br_{0.15})_3$. (c) Scatter plot of I_{sc} and effective trap density (N_{eff}). Each point corresponds to the average value of all the values in each I_{pc} and N_{eff} map after grain boundary elimination (with standard error). Red line is the fitting result (except FAMA 1), and number is the annealing time (e.g., FAMA 1 for 1-min annealing).

(d)		1 min	15 min
FAMA	Grain Size (nm)	220 (± 80)	220 (± 70)
	I_{sc} (nA)	0.76 (± 0.42)	0.67 (± 0.35)
CsFAMA	Grain Size (nm)	230 (± 80)	210 (± 70)
	I_{sc} (nA)	1.11 (± 0.66)	0.90 (± 0.51)

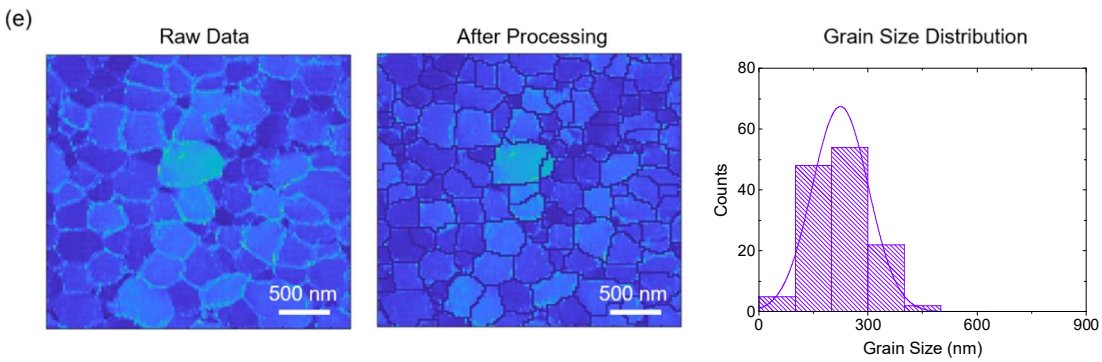

Fig. 2-14. (Color) (Continued) (d) I_{sc} and grain size at each perovskite. (e) Example of grain-boundary elimination using Sobel method (e.g., FAMA 1). For the normal distribution curve (100 nm-column width), grain size is determined using the image processing tool in MATLAB.

2.3.3. Capacitance Analyses for Deep Electronic Traps and Mobile Defects

Figure 2-15 compares the capacitance of each solar cell where capacitance is derived from the impedance as $C \equiv 1/i\omega Z$. Impedance spectroscopy in perovskite solar cells revealed the microscopic origins of resistive, capacitive, and inductive elements with their correlations to the photovoltaic performance [37,53-55]. Nyquist, Bode, and capacitance plots are compared between MA, FAMA, and CsFAMA cells in Fig. 2-16, and two arcs are commonly distinguished. It is noteworthy to mention that hybrid perovskite is known to exhibit mixed electronic/ionic conduction, and electric fields enable the transport of ionic constituents [2]. The open characteristics of grain boundaries normally results in facile ionic diffusion while ion migration is also evident in a single grain. Entangled ionic contributions in addition to the electronic conduction complicated the direct comparison to both cell performance and microscopic origins such as diffusion paths and ionic species. We have observed the increased resistance at a low frequency for both FAMA and CsFAMA than MA (Fig. 2-16(a)). It may involve the impeded ionic transport by the decreased lattice size, which will be discussed with relation to the charge accumulation and cell parameters in the following. Capacitance rather than resistance is studied herein based on the various capacitive effects in solar cells (e.g., capacitive current by mobile ions for *J-V* hysteresis, electrode polarization by interfacial charge accumulation, etc.) [31,33].

The measured low-frequency capacitance value (Fig. 2-15(a)) is similar regardless of annealing and composition. The high-frequency capacitance is identical irrespective of annealing, but it depends on the composition. Transition is shifted to a higher

frequency in the CsFAMA > FAMA > MA cells. The high-frequency capacitance is attributed to the geometrical capacitance of the perovskite layer and depletion-layer capacitance at each interface [53,56]. A dielectric-constant change by compositions gives rise to the differences of both geometrical and depletion capacitances. The low-frequency capacitance is suggested to originate from the charge accumulation at the interfaces and/or charging/discharging of traps in a junction (in addition to the geometrical and depletion capacitances) [57-62]. First, electrode polarization is demonstrated from the light-intensity-dependent exponential increase of capacitance by photogenerated hole accumulation [57]. Under dark, facile ionic diffusion also results in the interfacial charge accumulation, and ion blocking properties of each contact material in a solar cell also have potential for the electric double layer formation by ionic charges [32,33]. Besides the charge accumulation, frequency-dependent capacitance originates from the electronic traps by trapping/detrapping of intrinsic carriers (charging/discharging of traps) [58-62]. Contributions of traps into capacitance is determined by relative energy level of traps in the bandgap, angular frequency of ac voltage (Fermi-level), and temperature (relations described in Table 2-2). Deep-level traps (far from the bandedge) can contribute to the capacitance at a low frequency and a high temperature, and vice versa for the traps shifted toward the bandedge. Thereby, the capacitance-frequency spectra can be converted into the trap-density distribution vs. E_{ω} (= E - $E_{Bandedge}$), as shown in Fig. 2-15(b). The derivative of capacitance (C) as frequency gives a trap density (Eq. (1)), and angular frequency (ω) corresponding for the maximum $dC/d(\ln \omega)$ converts into a trap energy level (Eq. (2)). The details of input parameters (in Table 2-2) are assumed as following: built-in potential as 1 V (Fig. 2-17), depletion width of 400 nm (perovskite thickness in a *n-i-p* junction), temperature of 300 K, and attempt-to-escape frequency of

10^{12} s^{-1} [61,62]. Trap distribution is fitted using a Gaussian function (Eq. (3)), and parameters are summarized in Tables 2-2 and 2-3.

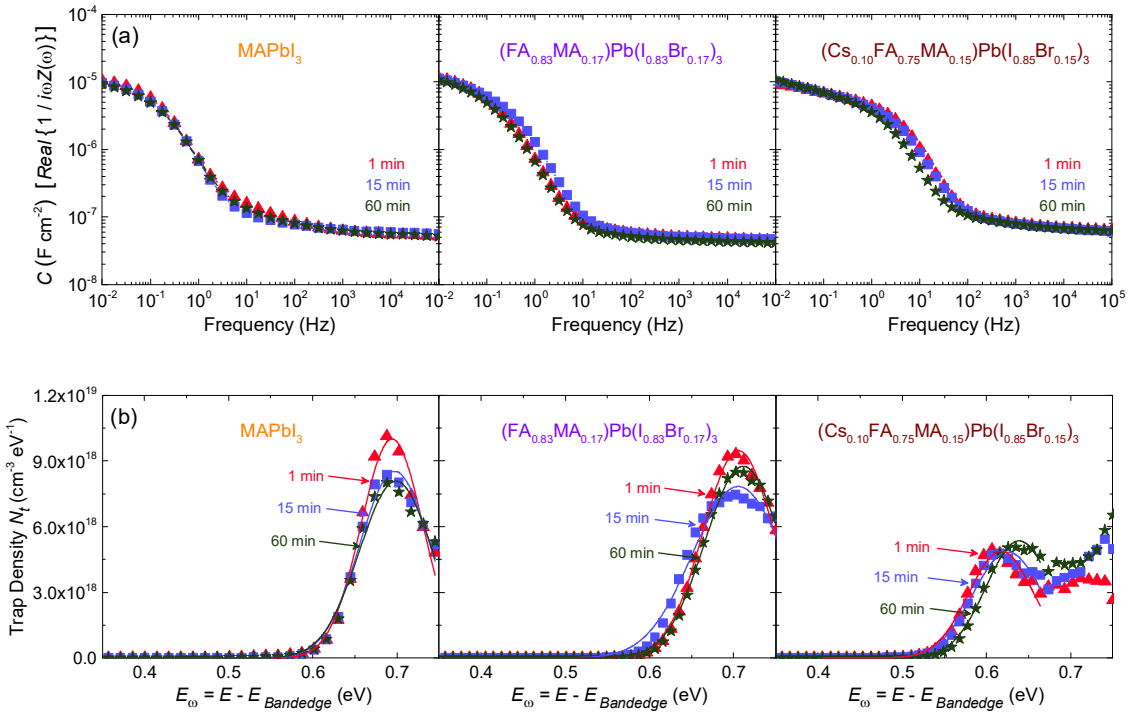

Fig. 2-15. (Color) Effect of perovskite composition (with annealing) on the capacitances and electronic traps. (a) Capacitance-frequency (top panel) and (b) trap analyses (bottom panel) of $MAPbI_3$, $(FA_{0.83}MA_{0.17})Pb(I_{0.83}Br_{0.17})_3$, and $(Cs_{0.10}FA_{0.75}MA_{0.15})Pb(I_{0.85}Br_{0.15})_3$ solar cells along different annealing between 1 and 60 min. Trap densities are approximated by a Gaussian, and the fitting results are summarized in Tables 2-2 and 2-3. The impedance measurement is performed under dark and without applied bias.

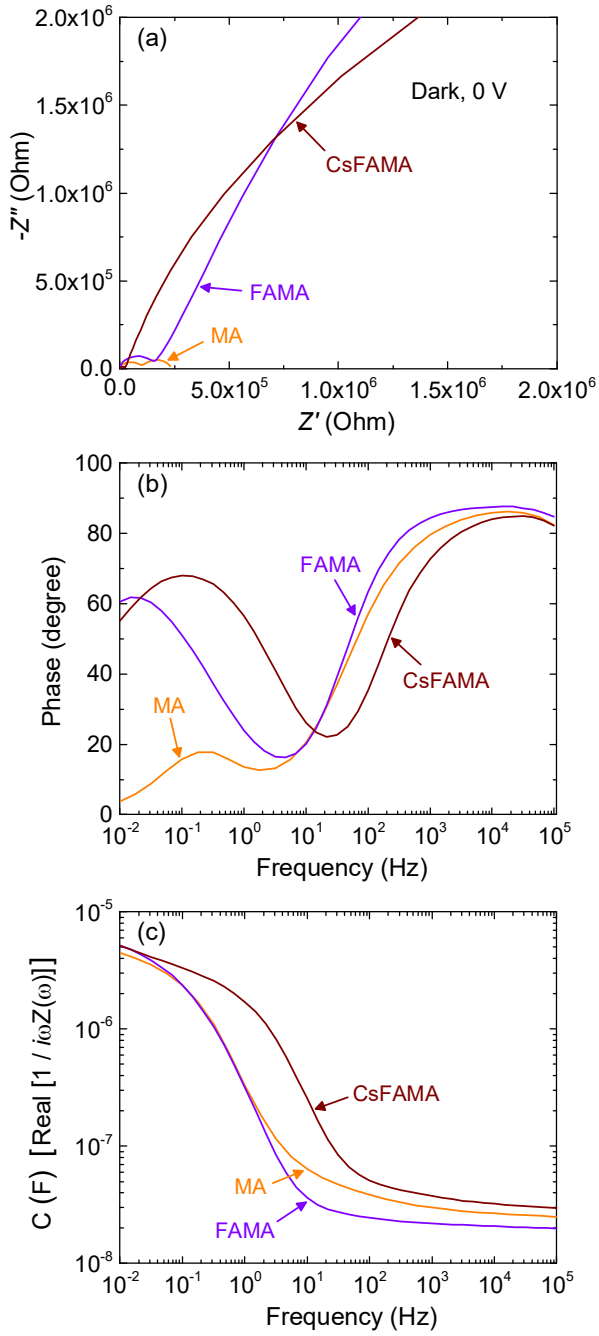

Fig. 2-16. (Color) Nyquist, Bode, and complex capacitance plot. (a) Nyquist plot (under dark and 0 V), (b) Bode plot, and (c) real part (C) of complex capacitance, respectively. Annealing is 60 min for all the compositions with the corresponding data in Fig. 2-15. Active area (Au electrode) is 0.48 cm^2.

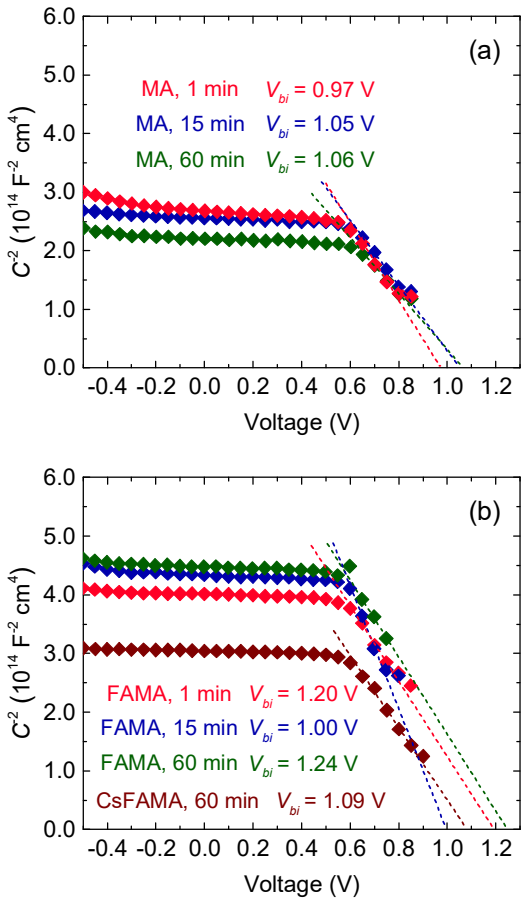

Fig. 2-17. (Color) Mott-Schottky analyses of MA, FAMA, and CsFAMA solar cells. (a) Annealing time control in $MAPbI_3$ and (b) $(FA_{0.83}MA_{0.17})Pb(I_{0.83}Br_{0.17})_3$ with additional Cs-doped one (60-min annealing), respectively. The measurement was carried out under dark and ac voltage amplitude of 10 mV at 30 kHz. The built-in potential (V_{bi}) was extracted from the dashed fitting line.

Table 2-2. Fitting results of trap density (N_t) vs. E - $E_{Bandedge}$ (= E_ω) in Fig. 2-15.

$$N_t = \frac{V_{bi}}{qW}\left(\frac{\partial C}{\partial \omega}\right)\frac{\omega}{k_B T} \qquad (1)$$

$$E_\omega = k_B T ln\left(\frac{\omega_0}{\omega}\right) \qquad (2)$$

V_{bi}: built-in potential, q: elementary charge, W: depletion width, C: capacitance, ω: angular frequency, k_B: Boltzmann constant, T: temperature, ω_0: attempt-to-escape frequency [58-62].

Fitting

$$N_t(E_\omega) = \frac{n_t}{\sqrt{2\pi}\sigma}\exp\left[-\frac{(E_0-E_\omega)^2}{2\sigma^2}\right] \qquad (3)$$

n_t: traps per volume, E_0: trap energy level, σ : disorder parameter.

Composition	Annealing Time	n_t (cm^{-3})	E_0 (eV)
MA	1 min	9.24±0.20 × 10^{17}	0.694±0.001
	15 min	8.93±0.21 × 10^{17}	0.698±0.001
	60 min	8.79±0.24 × 10^{17}	0.699±0.001
$FA_{0.83}MA_{0.17}$	1 min	1.01±0.01× 10^{18}	0.706±0.001
	15 min	1.06±0.03 × 10^{18}	0.705±0.002
	60 min	1.00±0.01 × 10^{18}	0.711±0.001
$Cs_{0.10}FA_{0.75}MA_{0.15}$	1 min	4.72±0.15 × 10^{17}	0.618±0.001
	15 min	5.03±0.16 × 10^{17}	0.626±0.002
	60 min	5.30±0.13 × 10^{17}	0.639±0.001

Table 2-3. Disorder parameter (in Table 2-2) from Fig. 2-15.

Composition	Annealing Time	Disorder Parameter σ (meV)
MA	1 min	36.9 (1.0)
	15 min	41.8 (1.2)
	60 min	43.4 (1.4)
$FA_{0.83}MA_{0.17}$	1 min	42.4 (0.5)
	15 min	54.5 (1.6)
	60 min	45.4 (0.6)
$Cs_{0.10}FA_{0.75}MA_{0.15}$	1 min	38.7 (1.5)
	15 min	41.5 (1.6)
	60 min	39.5 (1.0)

The trap distribution spectra provide the differences among the annealing and compositional conditions (Table 2-2). In the aspect of thermal annealing, a trap density is decreased as annealing for MA, and it is in accordance with the η tendency that the increase of η in Fig. 2-1(b) is attributed to the trap density reduction. Trap density reduction for MA at a longer annealing time is correlated to the grain growth as analyzed in the SEM image of Fig. 2-9 (further supported by XRD characterization in Figs. 2-10(d-f)), and the possible trap passivation by PbI_2 is ruled-out since PbI_2 is negligible even at the longer annealing as shown in diffraction of Figs. 2-10(a) and (b). The correlation between grain growth and trap reduction in MA suggests that grain boundaries are mainly the origin of electronic traps, however, the theoretical calculations have revealed that the grain boundaries do not generate deep trap states in the bandgap [24]. Accordingly, the reduction of interfacial traps which is originated from the enlarged grains (and preferred orientation) is worthy to be considered. Different to the MA perovskite, both FAMA and CsFAMA perovskites do not show distinctive changes as annealing (similar η irrespective of the annealing as shown in Fig. 2-1(b)).

For the different composition, traps at deep level (~0.7 eV vs. bandedge) are reduced for CsFAMA compared to both MA and FAMA, and less-deep-level traps (~0.6 eV) are identified. Trap density at ~0.6 eV in CsFAMA is about half compared to the trap density at ~0.7 eV in both MA and FAMA (Fig. 2-15(b)). Even though the diffraction peaks are broadened for CsFAMA compared to MA (Figs. 2-10(d-f)), the reduction of trap density is observed for CsFAMA than MA, suggesting the improved property of CsFAMA in the aspect of electronic traps. In addition, the improved crystallinity of CsFAMA than FAMA (peak sharpening as can be compared between Figs. 2-10(e) and (f)) is correlated to the lower trap density. CsFAMA films are

independently deposited by using different precursor concentrations to confirm whether the differences of E_{ω} (= E - $E_{Bandedge}$) are the general results. Figure 2-18 shows the effects of concentration tuning on both the cell performance and trap distributions in $(Cs_{0.10}FA_{0.75}MA_{0.15})Pb(I_{0.85}Br_{0.15})_3$. Actually, trap states shifting toward the bandedge (CsFAMA compared to both MA and FAMA) is identified for all the conditions having similar photovoltaic performances, demonstrating the common effects of Cs incorporation in the trap states [21].

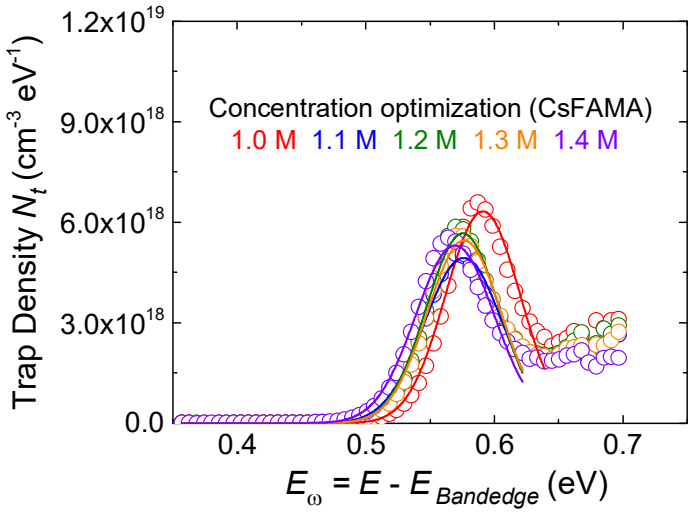

Fig. 2-18. (Color) Concentration optimization of $(Cs_{0.10}FA_{0.75}MA_{0.15})Pb(I_{0.85}Br_{0.15})_3$. Molar ratio of 0.5 : 5 : 1 : 5 : 1 = CsI : FAI : MABr : PbI_2 : $PbBr_2$ is fixed, with frequency herein is 10^{-1} to 10^5 Hz.

Figure 2-19 exhibits the variation of capacitance spectra over the 2-week shelf-life test (with 60-min annealing for all the compositions). While the original capacitance for MA is approximately maintained in the course of test, both FAMA and CsFAMA cells clearly exhibit the gradual shift to higher frequency. In the aspect of deep trap levels, it is kept almost constant for MA, while it has shifted toward the bandedge for both FAMA and CsFAMA. Distinctive trends are consistently observed over the long-term test, that is, more than 6 weeks, as shown in Fig. 2-20. The variations of trap density and disorder parameter are tabulated in the inset of Fig. 2-20. As explained in Fig. 2-1(c), η of each cell falls off analogously regardless of compositions. However, V_{oc} change is distinguished between MA and (Cs)FAMA in that it is negligible in both FAMA and CsFAMA as displayed in Fig. 2-1(d). Negligible microstructural degradation of materials (diffraction in Fig. 2-10(c)) argues that causes of a different cell stability may lie in the nanoscopic origins of ionic defects such as electronic traps and mobile ions.

Impedance is analyzed at different applied bias voltages (Fig. 2-21). Low-frequency capacitance (10 mHz) is compared between MA, FAMA, and CsFAMA, and it follows the exponential function (Fig. 2-21(d)). The degree of increase is prominent for MA, and it is weakened in both FAMA and CsFAMA. Prolonged annealing diminishes the level of rising, and the amount of decrease is conspicuous for MA cells. The low-frequency capacitance, which is attributed to the ionic charge accumulation, is decreased as MA > FAMA > CsFAMA. Electric double layer formation by ionic charges supports the exponential dependence, and weak dependence of capacitance on the bias involves the low accumulated-charge density (with fitting parameters in Table 2-4) [33]. Consistently, *J-V* hysteresis is reduced as MA > FAMA > CsFAMA (Fig. 2-7). Combining the capacitance spectra and *J-V* analyses together, it is concluded that the improved η with

the reduced hysteresis is attributed to the reduction of both electronic trap density (Fig. 2-15) and mobile ion concentration (Fig. 2-21). With the reduction of electronic traps and mobile ions, the photovoltaic performance enhancement is expected as seen in the CsFAMA cells herein. Also, defect annihilation through illumination has some potential to sustain constant V_{oc} (even slight increase) by compelling with defect formation [30]. We have analyzed the perovskite surface after the elimination of the upper layers (hole-transport material and Au electrode) to characterize the possible defect formation at the interface for the solar cells which have experienced the shelf-life test for more than 1 month (Fig. 2-22). The absence of additional chemical states through XPS implies the relatively intact perovskite at the interface of hole-transport materials, supporting the importance of the interface with the electron-transport material for the further stability improvement as discussed below [43].

Regarding the variation of photovoltaic parameters over time, both the electronic traps and ion migration adversely affect the cell performance that their influences should be minimized. Trapped charge-driven perovskite degradation under the ambient environment emphasizes the need of trap reduction together with the blocking of atmospheric elements (O_2 and H_2O) to suppress the photovoltaic performance drop [63]. Polarity-dependent perovskite instability points out the critical role of both charge extraction and mobile ions on the degradation mechanisms [64]. MA cells exhibit high trap- and mobile-ion- concentrations, and CsFAMA cells are opposite to MA in our results. Due to the negligible change of both microstructural and surface properties after the stability test, we attribute the different cell behaviors depending on the perovskite composition to the distinctive defect characters. CsFAMA cells exhibit stable V_{oc} during the stability test with high initial efficiency and low *J-V* hysteresis, while MA cells having

high defect density undergo rapid V_{oc} drops. (FAMA cells also show stable V_{oc}, supporting the merits of compositional mixing in recent state-of-the-art devices, and the study on the underlying microscopic origins is further needed.) The relatively low V_{oc} compared to the state-of-the-art devices (beyond 1.10 V) might cause the accelerated degradation of photovoltaic performance, and it might be due to the high defect density by the defective charge-transport layers (e.g., TiO_2) in addition to the perovskites [65,66].

In summary, further defect engineering of perovskite is expected to realize the long-term stability through reducing the trap/ion migration-mediated instability, which is also expected to gain higher V_{oc}. The novel selective contacts with additional cell encapsulation will further prevent the defect formation and enable for the improved stability [43,67].

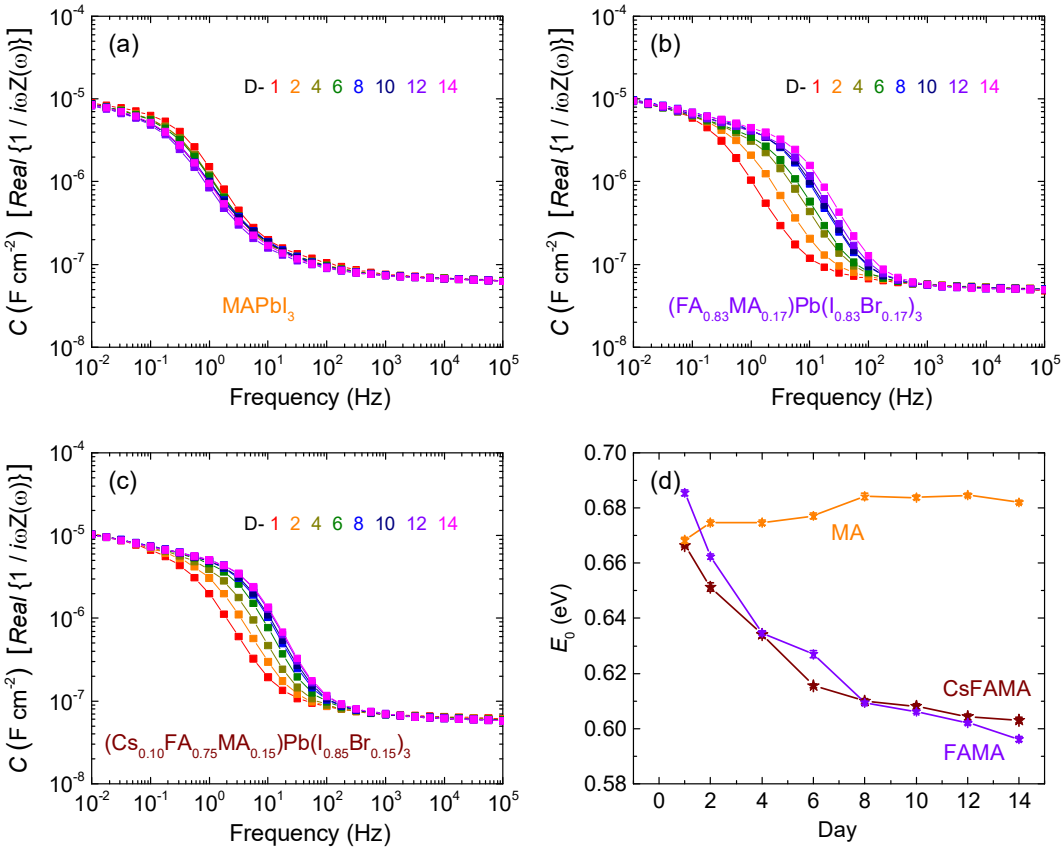

Fig. 2-19. (Color) Capacitance and trap energy level (E_0) variations by solar cell aging. Capacitance analyses of (a) $MAPbI_3$, (b) $(FA_{0.83}MA_{0.17})Pb(I_{0.83}Br_{0.17})_3$, and (c) $(Cs_{0.10}FA_{0.75}MA_{0.15})Pb(I_{0.85}Br_{0.15})_3$ cells during the stability measurement. Number is the measurement date (e.g., D-1 for the cell fabrication date). (d) Variation of trap energy level (E_0) derived from Eqs. (1), (2), and (3) in Table 2-2.

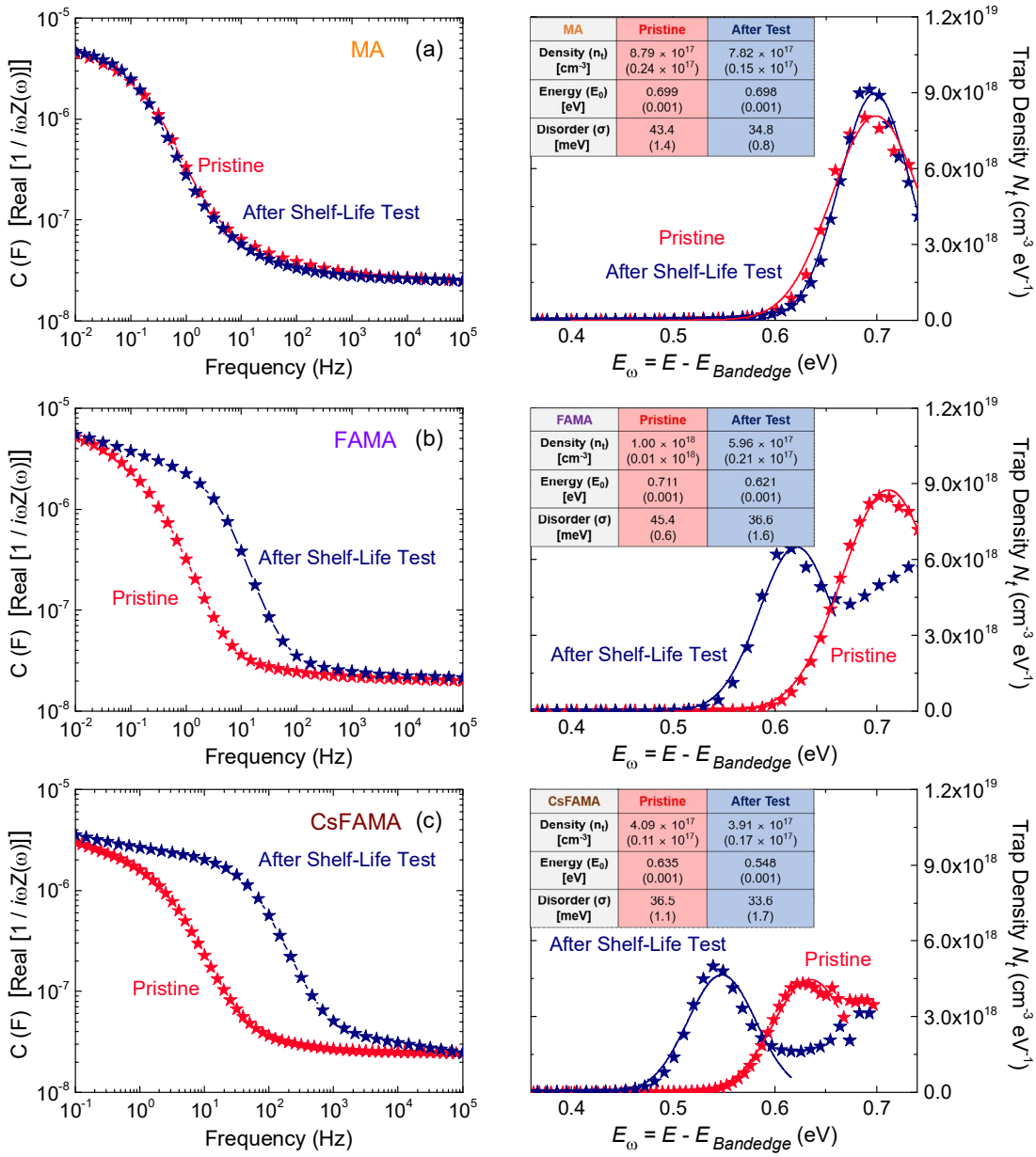

Fig. 2-20. (Color) Long-term aging effect on capacitance and trap state in solar cells. (a) Capacitance-frequency change after stability test of $MAPbI_3$ cell and the corresponding trap with the inset of fitting parameters (raw data: star, and fitting: line).

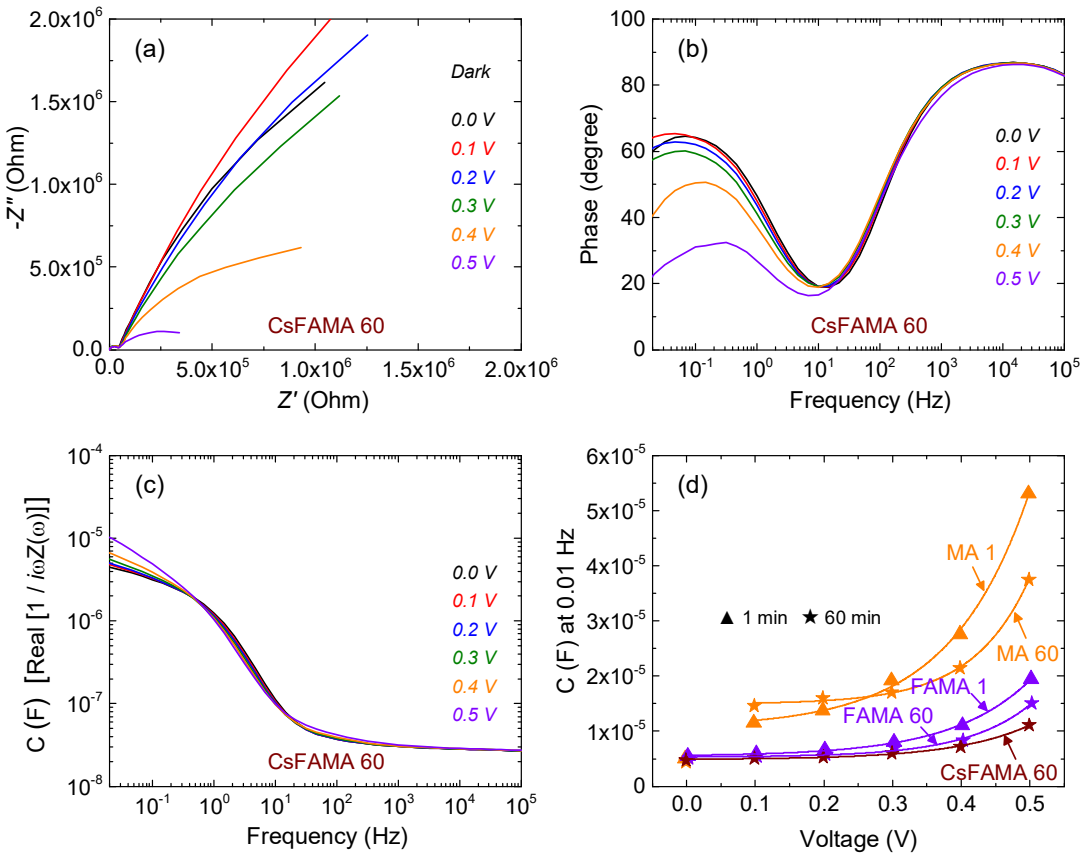

Fig. 2-21. (Color) Annealing and composition effects on the low-frequency capacitance. (a) Nyquist plot, (b) Bode plot, and (c) capacitance plot (applied-voltage control under dark). Number is the annealing time (e.g., CsFAMA 60 for 60-min annealing). (d) Dependency of low-frequency capacitance on the applied voltage, and the lines are the fitting results.

Table 2-4. Fitting parameters in Fig. 2-21(d).

Fitting equation for Fig. 2-21(d): Capacitance (V) $= A_0 + A_1 e^{V/A_2}$, where V is voltage.				
	Annealing Time	A_0 (F)	A_1 (F)	A_2 (V)
MA	1 min	1.06×10^{-5} (1.12×10^{-6})	5.62×10^{-7} (2.25×10^{-7})	0.12 (0.01)
	60 min	1.49×10^{-5} (4.06×10^{-7})	5.41×10^{-8} (2.57×10^{-8})	0.08 (0.01)
FAMA	1 min	5.46×10^{-6} (1.65×10^{-7})	1.73×10^{-7} (3.59×10^{-8})	0.11 (0.01)
	60 min	5.30×10^{-6} (2.33×10^{-7})	4.77×10^{-8} (2.74×10^{-8})	0.09 (0.01)
CsFAMA	60 min	4.86×10^{-6} (1.60×10^{-7})	6.72×10^{-8} (3.21×10^{-8})	0.11 (0.01)

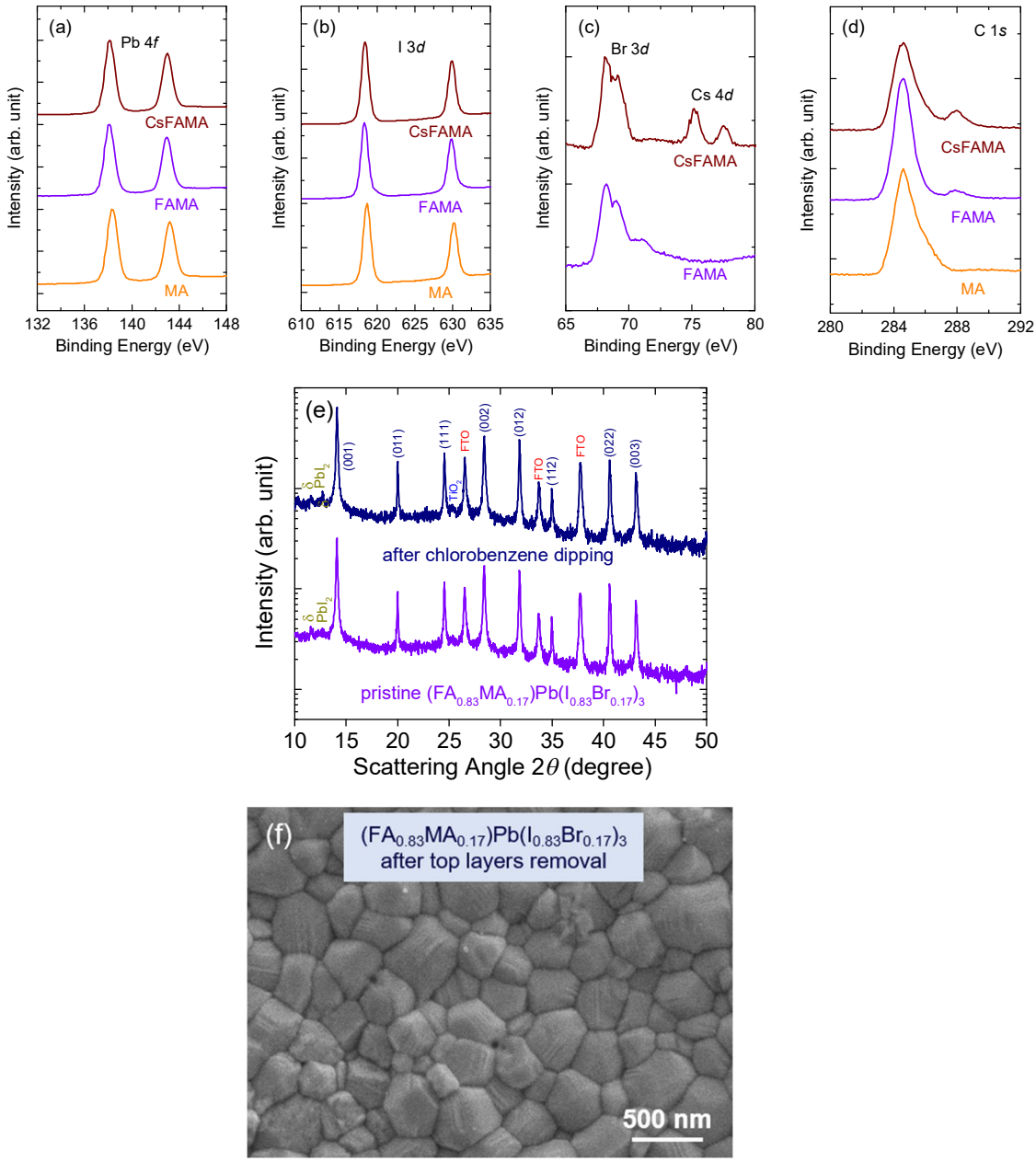
(a)
Pb 4f
CsFAMA
FAMA
MA
Intensity (arb. unit)
132 136 140 144 148
Binding Energy (eV)
(b)
I 3d
CsFAMA
FAMA
MA
Intensity (arb. unit)
610 615 620 625 630 635
Binding Energy (eV)
(c)
Br 3d
Cs 4d
CsFAMA
FAMA
Intensity (arb. unit)
65 70 75 80
Binding Energy (eV)
(d)
C 1s
CsFAMA
FAMA
MA
Intensity (arb. unit)
280 284 288 292
Binding Energy (eV)
(e)
δ-PbI2
(001)
(011)
(111)
TiO2
FTO
(002)
(012)
FTO
(112)
FTO
(022)
(003)
after chlorobenzene dipping
δ-PbI2
pristine (FA0.83MA0.17)Pb(I0.83Br0.17)3
Intensity (arb. unit)
10 15 20 25 30 35 40 45 50
Scattering Angle 2θ (degree)
(f)
(FA0.83MA0.17)Pb(I0.83Br0.17)3
after top layers removal
500 nm

Fig. 2-22. (Color) Analyses of perovskite surface after the shelf-life test. X-ray photoelectron spectroscopy for (a) Pb 4*f*, (b) I 3*d*, (c) Br 3*d* and Cs 4*d*, and (d) C 1*s* of $MAPbI_3$, $(FA_{0.83}MA_{0.17})Pb(I_{0.83}Br_{0.17})_3$, and $(Cs_{0.10}FA_{0.75}MA_{0.15})Pb(I_{0.85}Br_{0.15})_3$ surfaces after the elimination of upper hole-transport layer and Au electrode. (e) X-ray diffraction and (f) surface morphology before and after the removal of upper layers in the $(FAPbI_3)_{0.83}(MAPbBr_3)_{0.17}$ cell. Peaks are indexed to cubic α-$FAPbI_3$ (with δ for the hexagonal $FAPbI_3$).

2.4. Conclusions

In this work, the role of ionic defects on perovskite solar-cell performance was examined. $MAPbI_3$, $(FA_{0.83}MA_{0.17})Pb(I_{0.83}Br_{0.17})_3$, and $(Cs_{0.10}FA_{0.75}MA_{0.15})Pb(I_{0.85}Br_{0.15})_3$ were compared with an additional thermal-annealing control for different grain growth. The enlarged grain of $MAPbI_3$ resulted in an efficiency increase while the enhancement was negligible in others, and the efficiency difference among the perovskites was attributed to the distinctive electronic traps. Electrical $1/f$ noises of perovskites and capacitance analyses of solar cells revealed that CsFAMA had a lower trap density with a trap-energy level close to the bandedge. Furthermore, V_{oc} change during the shelf-life test was correlated to the trap-state variation Solar cells with the negligible change of V_{oc} over weeks exhibited trap states shifting toward the bandedge in spite of the decreasing power-conversion efficiency. In addition to the electronic traps, a low-frequency capacitance was analysed to understand the effects of charge accumulation on the photovoltaic performance, and the reduction of mobile-defect accumulation led to both efficient and stable cell properties. Solar cell degradation was discussed focusing on the traps/defects in the perovskite and interfaces of solar cells, supporting the recent approaches for improving the performance based on the defect and interface engineering.

2.5. References

1. Jeon, N. J.; Na, H.; Jung, E. H.; Yang, T.-Y.; Lee, Y. G.; Kim, G.; Shin, H.-W.; Seok, S. I.; Lee, J.; Seo, J. A Fluorene-Terminated Hole-Transporting Material for Highly Efficient and Stable Perovskite Solar Cells. *Nat. Energy* **2018**, *3*, 682-689.
2. Hwang, T.; Lee, B.; Kim, J.; Lee, S.; Gil, B.; Yun, A. J.; Park, B. From Nanostructural Evolution to Dynamic Interplay of Constituents: Perspectives for Perovskite Solar Cells. *Adv. Mater.* **2018**, 1704208.
3. Miller, O. D.; Yablonovitch, E.; Kurtz, R. Strong Internal and External Luminescence as Solar Cells Approach the Shockley–Queisser Limit. *IEEE. J. Photovolt.* **2012**, *2* 303-311.
4. Ruhle, S. Tabulated Values of the Shockley–Queisser Limit for Single Junction Solar Cells. *Solar Energy* **2016**, *130*, 139-147.
5. Abdi-Jalebi, M.; Andaji-Garmaroudi, Z.; Cacovich, S.; Stavrakas, C.; Philippe, B.; Richter, J. M.; Alsari, M.; Booker, E. P.; Hutter, E. M.; Pearson, A. J.; Lilliu, S.; Savenije, T. J.; Rensmo, H.; Divitni, G.; Ducati, C.; Friend, R. H.; Stranks, S. D. Maximizing and Stabilizing Luminescence from Halide Perovskites with Potassium Passivation. *Nature* **2018**, *555*, 497-501.
6. Polman, A.; Atwater, H. A. Photonic Design Principles for Ultrahigh-Efficiency Photovoltaics. *Nat. Mater.* **2012**, *11*, 174-177.
7. Mcdaniel, H.; Heil, P. E.; Tsai, C.-L.; Kim, K.; Shim, M. Integration of Type II Nanorod Heterostructures into Potovoltaics. *ACS Nano* **2011**, *5*, 7677-7683.
8. Lin, C.-H.; Chattopadhyay, S.; Hsu, C.-W.; Wu, M.-H.; Chen, W.-C.; Wu, C.-T.; Tseng, S.-C.; Hwang, J.-S.; Lee, J.-H.; Chen, C.-W.; Chen, C.-H.; Chen, L.-C.;

Chen, K.-H. Enhanced Charge Separation by Sieve-Layer Mediation in High-Efficiency Inorganic-Organic Solar Cells. *Adv. Mater.* **2009**, *21*, 759-763.

9. Kim, D. U.; Hangarter, C. M.; Debnath, R.; Ha, J. Y.; Beauchamp, C. R.; Widstrom, M. D.; Guyer, J. E.; Nguyen, N.; Yoo, B. Y.; Josell, D. Backcontact CdSe/CdTe Windowless Solar Cells. *Solar Energ. Mat. Sol. C.* **2013**, *109*, 246-253.
10. Fei, C.; Li, B.; Zhang, R.; Fu, H.; Tian, J.; Cao, G. Highly Efficient and Stable Perovskite Solar Cells Based on Monolithically Grained $CH_3NH_3PbI_3$ Film. *Adv. Energy Mater.* **2017**, *7*, 1602017.
11. Kim, W.; Jung, M. S.; Lee, S.; Choi, Y. J.; Kim, J. K.; Chai, S. U; Kim, W.; Choi, D.-G.; Ahn, H.; Cho, J. H.; Choi, D.; Shin, H.; Kim, D.; Park, J. H. Oriented Grains with Preferred Low-Angle Grain Boundaries in Halide Perovskite Films by Pressure-Induced Crystallization. *Adv. Energy Mater.* **2018**, *8*, 1702369.
12. Bi, C.; Wang, Q.; Shao, Y.; Yuan, Y.; Xiao, Z.; Huang, J. Non-Wetting Surface-Driven High-Aspect-Ratio Crystalline Grain Growth for Efficient Hybrid Perovskite Solar Cells. *Nat. Commun.* **2015**, *6*, 7747.
13. Kim, D. H.; Park, J.; Li, Z.; Yang, M.; Park, J.-S.; Park, I. J.; Kim, J. Y.; Berry, J. J.; Rumbles, G.; Zhu, K. 300% Enhancement of Carrier Mobility in Uniaxial-Oriented Perovskite Films Formed by Topotactic-Oriented Attachment. *Adv. Mater.* **2017**, *29*, 1606831.
14. Ham, S.; Choi, Y. J.; Lee, J.-W.; Park, N.-G.; Kim, D. Impact of Excess CH_3NH_3I on Free Carrier Dynamics in High-Performance Nonstoichiometric Perovskites. *J. Phys. Chem. C* **2017**, *121*, 3143-3148.

15. Son, D.-Y.; Lee, J.-W.; Choi, Y. J.; Jang, I.-H.; Lee, S.; Yoo, P. J.; Shin, H.; Ahn, N.; Choi, M.; Kim, D.; Park, N.-G. Self-Formed Grain Boundary Healing Layer for Highly Efficient $CH_3NH_3PbI_3$ Perovskite Solar Cells. *Nat. Energy* **2016**, *1*, 16081.
16. Leguy, A. M. A.; Hu, Y.; Campoy-Quiles, M.; Alonso, M. I.; Weber, O. J.; Azarhoosh, P.; Schilfgaarde, M. v.; Weller, M. T.; Bein, T.; Nelson, J.; Docampo, P., Barnes, P. R. F. Reversible Hydration of $CH_3NH_3PbI_3$ in Films, Single Crystals, and Solar Cells. *Chem. Mater.* **2015**, *27*, 3397-3407.
17. Aristidou, N.; Eames, C.; Sanchez-Molina, I.; Bu, X.; Kosco, J.; Islam, M. S.; Haque, S. A. Fast Oxygen Diffusion and Iodide Defects Mediate Oxygen-Induced Degradation of Perovskite Solar Cells. *Nat. Commun.* **2017**, *8*, 15218.
18. Saidaminov, M. I.; Kim, J.; Jain, A.; Quintero-Bermudez, R.; Tan, H.; Long, G.; Tan, F.; Johnston, A.; Zhao, Y.; Voznyy, O.; Sargent, E. H. Suppression of Atomic Vacancies via Incorporation of Isovalent Small Ions to Increase the Stability of Halide Perovskite Solar Cells in Ambient Air. *Nat. Energy* **2018**, *3*, 648-654.
19. Yang, W. S.; Park, B.-W.; Jung, E. H.; Jeon, N. J.; Kim, Y. C.; Lee, D. U.; Shin, S. S.; Seo, J.; Kim, E. K.; Noh, J. H.; Seok, S. I. Iodide Management in Formamidinium-Lead-Halide-Based Perovskite Layers for Efficient Solar Cells. *Science* **2017**, *356*, 1376-1379.
20. Son, D.-Y.; Kim, S.-G.; Seo, J.-Y.; Lee, S.-H.; Shin, H.; Lee, D.; Park, N.-G. Universal Approach toward Hysteresis-Free Perovskite Solar Cell via Defect Engineering. *J. Am. Chem. Soc.* **2018**, *140*, 1358-1364.
21. Hu, Y.; Hutter, E. M.; Rieder, P.; Grill, I.; Hanisch, J.; Aygüler, M. F.; Hufnagel, A. G.; Handloser, M.; Bein, T.; Hartschuh, A.; Tvingstedt, K.; Dyakonov, V.; Baumann, A.; Savenije, T. J.; Petrus, M. L.; Docampo, P. Understanding the Role of Cesium

and Rubidium Additives in Perovskite Solar Cells: Trap States, Charge Transport, and Recombination. *Adv. Energy Mater.* **2018**, *8*, 1703057.

22. Zhao, J.; Deng, Y.; Wei, H.; Zheng, X.; Yu, Z.; Shao, Y.; Shield, J. E.; Huang, J. Strained Hybrid Perovskite Thin Films and Their Impact on the Intrinsic Stability of Perovskite Solar Cells. *Sci. Adv.* **2017**, *3*, eaao5616.
23. Zheng, X.; Chen, B.; Dai, J.; Fang, Y.; Bai, Y.; Lin, Y.; Wei, H.; Zeng, X. C.; Huang, J. Defect Passivation in Hybrid Perovskite Solar Cells Using Quaternary Ammonium Halide Anions and Cations. *Nat. Energy* **2017**, *2*, 17102.
24. Yin, W.-J.; Shi, T.; Yan, Y. Unique Properties of Halide Perovskites as Possible Origins of the Superior Solar Cell Performance. *Adv. Mater.* **2014**, *26*, 4653-4658.
25. Xie, L.-Q.; Chen, L.; Nan, Z.-A.; Lin, H.-X.; Wang, T.; Zhan, D.-P.; Yan, J.-W.; Mao, B.-W.; Tian, Z.-Q. Understanding the Cubic Phase Stabilization and Crystallization Kinetics in Mixed Cations and Halides Perovskite Single Crystals. *J. Am. Chem. Soc.* **2017**, *139*, 3320-3323.
26. Abdi-Jalebi, M.; Dar, M. I.; Sadhanala, A.; Senanayak, S. P.; Franckevicius, M.; Arora, N.; Hu, Y.; Nazeeruddin, M. K.; Zakeeruddin, S. M.; Grätzel, M.; Friend, R. H. Impact of Monovalent Cation Halide Additives on the Structural and Optoelectronic Properties of $CH_3NH_3PbI_3$ Perovskite. *Adv. Energy Mater.* **2016**, *6*, 1502472.
27. Bag, S.; Durstock, M. F. Large Perovskite Grain Growth in Low-Temperature Solution-Processed Planar P-I-N Solar Cells by Sodium Addition. *ACS Appl. Mater. Interfaces* **2016**, *8*, 5053-5057.

28. Wang, Q.; Chen, B.; Liu, Y.; Deng, Y.; Bai, Y.; Dong, Q.; Huang, J. Scaling Behavior of Moisture-Induced Grain Degradation in Polycrystalline Hybrid Perovskite Thin Films. *Energy Environ. Sci.* **2017**, *10*, 516-522.

29. DeQuilettes, D. W.; Zhang, W.; Burlakov, V. M.; Graham, D. J.; Leijtens, T.; Osherov, A.; Bulovic, V.; Snaith, H. J.; Ginger, D. S.; Stranks, S. D. Photo-Induced Halide Redistribution in Organic-Inorganic Perovskite Films. *Nat. Commun.* **2016**, *7*, 11683.

30. Mosconi, E.; Meggiolaro, D.; Snaith, H. J.; Stranks, S. D.; Angelis, F. D. Light-Induced Annihilation of Frenkel Defects in Organo-Lead Halide Perovskites. *Energy Environ. Sci.* **2016**, *9*, 3180-3187.

31. Ravishankar, S.; Almora, O.; Echeverría-Arrondo, C.; Ghahremanirad, E.; Aranda, C.; Guerrero, A.; Fabregat-Santiago, F.; Zaban, A.; Garcia-Belmonte, G.; Bisquert, J. Surface Polarization Model for the Dynamic Hysteresis of Perovskite Solar Cells. *J. Phys. Chem. Lett.* **2017**, *8*, 915-921.

32. Weber, S. A. L.; Hermes, I. M.; Turren-Cruz, S.-H.; Gort, C.; Bergmann, V. W.; Gilson, L.; Hagfeldt, A.; Graetzel, M.; Tress, W.; Berger, R. How the Formation of Interfacial Charge Causes Hysteresis in Perovskite Solar Cells. *Energy Environ. Sci.* **2018**, *11*, 2404-2413.

33. Almora, O.; Guerrero, A.; Garcia-Belmonte, G. Ionic Charging by Local Imbalance at Interfaces in Hybrid Lead Halide Perovskites. *Appl. Phys. Lett.* **2016**, *108*, 043903.

34. Carrillo, J.; Guerrero, A.; Rahimnejad, S.; Almora, O.; Zarazua, I.; Mas-Marza, E.; Bisquert, J.; Garcia-Belmonte, G. Ionic Reactivity at Contacts and Aging of Methylammonium Lead Triiodide Perovskite Solar Cells. *Adv. Energy Mater.* **2016**, *6*, 1502246.

35. Christians, J. A.; Habisreutinger, S. N.; Berry, J. J.; Luther, J. M. Stability in Perovskite Photovoltaics: A Paradigm for Newfangled Technologies. *ACS Energy Lett.* **2018**, *3*, 2136-2143.

36. Cho, D.; Hwang, T.; Cho, D.-g.; Park, B.; Hong, S. Photoconductive Noise Microscopy Revealing Quantitative Effect of Localized Electronic Traps on the Perovskite-Based Solar Cell Performance. *Nano Energy* **2018**, *43*, 29-36.

37. Pockett, A.; Eperon, G. E.; Sakai, N.; Snaith, H. J.; Peter, L. M.; Cameron, P. J. Microseconds, Milliseconds and Seconds: Deconvoluting the Dynamic Behaviour of Planar Perovskite Solar Cells. *Phys. Chem. Chem. Phys.* **2017**, *19*, 5959-5970.

38. Rong, Y.; Hu, Y.; Ravishankar, S.; Liu, H.; Hou, X.; Sheng, Y.; Mei, A.; Wang, Q.; Li, D.; Xu, M.; Bisquert, J.; Han, H. Tunable Hysteresis Effect for Perovskite Solar Cells. *Energy Environ. Sci.* **2017**, *10*, 2383-2391.

39. Ma, T.; Zhang, Q.; Tadaki, D.; Hirano-Iwata, A.; Niwano, M. Fabrication and Characterization of High-Quality Perovskite Films with Large Crystal Grains. *J. Phys. Chem. Lett.* **2017**, *8*, 720-726.

40. Zhou, Y.; Game, O. S.; Pang, S.; Padture, N. P. Microstructures of Organometal Trihalide Perovskites for Solar Cells: Their Evolution from Solutions and Characterization. *J. Phys. Chem. Lett.* **2015**, *6*, 4827-4839.

41. Thompson, C. V. Grain Growth in Thin Films. *Annu. Rev. Mater. Sci.* **1990**, *20*, 245-268,

42. Yuan, Y.; Li, T.; Wang, Q.; Xing, J.; Gruverman, A.; Huang, J. Anomalous Photovoltaic Effect in Organic-Inorganic Hybrid Perovskite Solar Cells. *Sci. Adv.* **2017**, *3*, e1602164.

43. Christians, J. A.; Schulz, P.; Tinkham, J. S.; Schloemer, T. H.; Harvey, S. P.; Villers, B. J. T. d.; Sellinger, A.; Berry, J. J.; Luther, J. M. Tailored Interfaces of Unencapsulated Perovskite Solar Cells for >1,000 Hour Operational Stability. *Nat. Energy* **2018**, *3*, 68-74.

44. Wolf, S. D.; Holovsky, J.; Moon, S.-J.; Loper, P.; Niesen, B.; Ledinsky, M.; Haug, F.-J.; Yum, J.-H.; Ballif, C. Organometallic Halide Perovskites: Sharp Optical Absorption Edge and Its Relation to Photovoltaic Performance. *J. Phys. Chem. Lett.* **2014**, *5*, 1035-1039.

45. Wright, A. D.; Verdi, C.; Milot, R. L.; Eperon, G. E.; Perez-Osorio, M. A.; Snaith, H. J.; Giustino, F.; Johnston, M. B.; Herz, L. M. Electron–Phonon Coupling in Hybrid Lead Halide Perovskites. *Nat. Commun.* **2016**, *7*, 11755.

46. Lee, B.; Lee, S.; Cho, D.; Kim, J.; Hwang, T.; Kim, K. H.; Hong, S.; Moon, T.; Park, B. Evaluation the Optoelectronic Quality of Hybrid Perovskites by Conductive Atomic Force Microscopy with Noise Spectroscopy. *ACS Appl. Mater. Interfaces* **2016**, *8*, 30985-30991.

47. Hwang, T.; Cho, D.; Kim, J.; Kim, J.; Lee, S.; Lee, B.; Kim, K. H.; Hong, S.; Kim, C.; Park, B. Investigation of Chlorine-Mediated Microstructural Evolution of $CH_3NH_3PbI_3$(Cl) Grains for High Optoelectronic Responses. *Nano Energy* **2016**, *25*, 91-99.

48. Kim, D.; Kim, G. Y.; Ko, C.; Pae, S. R.; Lee, Y. S.; Gunawan, O.; Ogletree, D. F.; Jo, W.; Shin, B. Effects of Postsynthesis Thermal Conditions on Methylammonium Lead Halide Perovskite: Band Bending at Grain Boundaries and Its Impacts on Solar Cell Performance. *J. Phys. Chem. C* **2016**, *120*, 21330-21335.

49. MacDonald, G. A.; Yang, M.; Berweger, S.; Killgore, J. P.; Kabos, P.; Berry, J. J.; Zhu, K.; DelRio, F. W. Methylammonium Lead Iodide Grain Boundaries Exhibit Depth-Dependent Electrical Properties. *Energy Environ. Sci.* **2016**, *9*, 3642-3649.

50. Landi, G.; Neitzert, H. C.; Barone, C.; Mauro, C.; Lang, F.; Albrecht, S.; Rech, B.; Pagano, S. Correlation between Electronic Defect States Distribution and Device Performance of Perovskite Solar Cells. *Adv. Sci.* **2017**, *4*, 1700183.

51. Saidaminov, M. I.; Abdelhady, A. L.; Murali, B.; Alarousu, E.; Burlakov, V. M.; Peng, W.; Dursun, I.; Wang, L.; He, Y.; Maculan, G.; Goriely, A.; Wu, T.; Mohammed, O. F.; Bakr, O. M. High-Quality Bulk Hybrid Perovskite Single Crystals within Minutes by Inverse Temperature Crystallization. *Nat. Commun.* **2015**, *6*, 7586.

52. Zohar, A.; Levine, I.; Gupta, S.; Davidson, O.; Azulay, D.; Millo, O.; Balberg, I.; Hodes, G.; Cahen, D. What is the Mechanism of $MAPbI_3$ P-Doping by I_2? Insights from Optoelectronic Properties. *ACS Energy Lett.* **2017**, *2*, 2408-2414.

53. Zarazua, I.; Han, G.; Boix, P. P.; Mhaisalkar, S.; Fabregat-Santiago, F.; Mora-Seró, I.; Bisquert, J.; Garcia-Belmonte, G. Surface Recombination and Collection Efficiency in Perovskite Solar Cells from Impedance Analysis. *J. Phys. Chem. Lett.* **2016**, *7*, 5105-5113.

54. Guerrero, A.; Garcia-Belmonte, G.; Mora-Sero, I.; Bisquert, J.; Kang, Y. S.; Jacobsson, T. J.; Correa-Baena, J.-P.; Hagfeldt, A. Properties of Contact and Bulk Impedances in Hybrid Lead Halide Perovskite Solar Cells Including Inductive Loop Elements. *J. Phys. Chem. C* **2016**, *120*, 8023-8032.

55. Zarazúa, I.; Sidhik, S.; Lopéz-Luke, T.; Esparza, D.; Rosa, E. D. l.; Reyes-Gomez, J.; Mora-Sero, I.; Garcia-Belmonte, G. Operating Mechanisms of Mesoscopic

Perovskite Solar Cells through Impedance Spectroscopy and *J-V* Modeling. *J. Phys. Chem. Lett.* **2017**, *8*, 6073-6079.

56. Almora, O.; Aranda, C.; Mas-Marzá, E.; Garcia-Belmonte, G. On Mott-Schottky Analysis Interpretation of Capacitance Measurements in Organometal Perovskite Solar Cells. *Appl. Phys. Lett.* **2016**, *109*, 173903.
57. Zarazua, I.; Bisquert, J.; Garcia-Belmonte, G. Light-Induced Space-Charge Accumulation Zone as Photovoltaic Mechanism in Perovskite Solar Cells. *J. Phys. Chem. Lett.* **2016**, *7*, 525-528.
58. Walter, T.; Herberholz, R.; Muller, C.; Schock, H. W. Determination of Defect Distributions from Admittance Measurements and Application to $Cu(In,Ga)Se_2$ Based Heterojunctions. *J. Appl. Phys.* **1996**, *80*, 4411-4420.
59. Khelifi, S.; Decock, K.; Lauwaert, J.; Vrielinck, H.; Spoltore, D.; Piersimoni, F.; Manca, J.; Belghachi, A.; Burgelman, M. Investigation of Defects by Admittance Spectroscopy Measurements in Poly (3-Hexylthiophene):(6,6)-Phenyl C_{61}-Butyric Acid Methyl Ester Organic Solar Cells Degraded under Air Exposure. *J. Appl. Phys.* **2011**, *110*, 094509.
60. Boix, P. P.; Garcia-Belmonte, G.; Muñecas, U.; Neophytou, M.; Waldauf, C.; Pacios, R. Determination of Gap Defect States in Organic Bulk Heterojunction Solar Cells from Capacitance Measurements. *Appl. Phys. Lett.* **2009**, *95*, 233302.
61. Samiee, M.; Konduri, S.; Ganapathy, B.; Kottokkaran, R.; Abbas, H. A.; Kitahara, A.; Joshi, P.; Zhang, L.; Noack, M.; Dalal, V. Defect Density and Dielectric Constant in Perovskite Solar Cells. *Appl. Phys. Lett.* **2014**, *105*, 153502.

62. Prochowicz, D.; Yadav, P.; Saliba, M.; Saski, M.; Zakeeruddin, S. M.; Lewiński, J.; Grätzel, M. Reduction in the Interfacial Trap Density of Mechanochemically Synthesized $MAPbI_3$. *ACS Appl. Mater. Interfaces* **2017**, *9*, 28418-28425.

63. Ahn, N.; Kwak, K.; Jang, M. S.; Yoon, H.; Lee, B. Y.; Lee, J.-K.; Pikhitsa, P. V.; Byun, J.; Choi, M. Trapped Charge-Driven Degradation of Perovskite Solar Cells. *Nat. Commun.* **2016**, *7*, 13422.

64. Lin, Y.; Chen, B.; Fang, Y.; Zhao, J.; Bao, C.; Yu, Z.; Deng, Y.; Rudd, P. N.; Yan, Y.; Yuan, Y.; Huang, J. Excess Charge-Carrier Induced Instability of Hybrid Perovskites. *Nat. Commun.* **2018**, *9*, 4981.

65. Jung, H. J.; Kim, D.; Kim, S.; Park, J.; Dravid, V. P.; Shin, B. Stability of Halide Perovskite Solar Cell Devices: *In Situ* Observation of Oxygen Diffusion under Biasing. *Adv. Mater.* **2018**, *30*, 1802769.

66. Hwang, T.; Lee, S.; Kim, J.; Kim, J.; Kim, C.; Shin, B.; Park, B. Tailoring the Mesoscopic TiO_2 Layer: Concomitant Parameters for Enabling High-Performance Perovskite Solar Cells. *Nanoscale Res. Lett.* **2017**, *12*, 57.

67. Shi, L.; Young, T. L.; Kim, J.; Sheng, Y.; Wang, L.; Chen, Y.; Feng, Z.; Keevers, M. J.; Hao, X.; Verlinden, P. J.; Green, M. A.; Ho-Baillie, A. W. Y. Accelerated Lifetime Testing of Organic-Inorganic Perovskite Solar Cells Encapsulated by Polyisobutylene. *ACS Appl. Mater. Interfaces* **2017**, *9*, 25073-25081.

Chapter 3.

Electronic Trap Modulation of Perovskite by MACl Post-Treatment for the Efficient Photovoltaic Performance

3.1. Introduction

Organic-inorganic halide perovskites present a photon-to-current conversion efficiency surpassing 23%, and minimum loss of bandgap energy and maximum photocarrier extraction will enable for the achievement of photovoltaic efficiency limit [1]. The inevitable entanglements among microstructural factors of perovskite films have normally complicated to pinpoint the variable to be controlled due to the critical roles by nanoscopic origins of point defects and electronic traps on the optoelectronic properties and the device performance [2-4].

The post-deposition treatment is widely utilized to improve the solar cell performance [5,6]. The role of CH_3NH_3Cl (MACl) on both surface post-treatment and perovskite formation is widely studied with the utilization of its values for the state-of-the-art devices [7-14]. In general for the surface post-treatment, vulnerability of perovskite to polar solvents has both positive and negative effects on film quality and photovoltaic performance. Microstructural reconstruction followed by morphological changes by post-treatment (MA*X* with *X*: Cl, Br, I) commonly accompanies grain growth

---

*The work presented in Chap. 3 is submitted to *Advanced Materials Interfaces* entitled,
"Electronic Trap Modulation of Perovskite Surface by MACl Post-Treatment for the Efficient Photovoltaic Performance"
Taehyun Hwang, Byungho Lee, Jinhyun Kim, Alan Jiwan Yun, Younghyun Lee, and Byungwoo Park*

with high optoelectronic properties [8-13,15]. MACl vapor also gives the grain growth with both enhanced crystallinity and photovoltaic performance [16]. Destructive effect by polar solvent could be minimized by mixing non-polar solvent that is stable against perovskite, providing the viability for the performance improvement [8].

MACl post-treatment after the perovskite formation, however, might have minute influence due to its small ionic radius and ease of evaporation, and negligible effects may involve the sensitivity of defect formation and annihilation in nanoscale [8]. It is supposed to originate from the nanostructural susceptibility to chemical reactions as supported by critical impacts of molecular species on both the electronic traps and materials degradation [8,17]. Therefore, the chemical states of chlorine leading to the photovoltaic performance enhancement is noteworthy from the prospect of surface defect passivation by electron-donating properties of chlorine, which is expected to act like Lewis base [18]. Chlorine-mediated reduction of both nonradiative recombination (Shockley-Read-Hall) and trapping/detrapping of photocarrier validate the defect passivation [19,20]. Additional organic cation will present the stoichiometry of film surface through compensating the loss of organic species, which is facile to evaporate during annealing that ultimately leading to the PbI_2 formation [9].

In chapter 3, the post-treatment using MACl solution is utilized for the surface defect passivation and efficient solar cells. Intact microstructures of beneath perovskite allow the investigation on the electronic traps with photocarrier recombination near the surface. For MACl treatment, photovoltaic performance is improved in $(Cs_{0.05}FA_{0.79}MA_{0.16})Pb(I_{0.84}Br_{0.16})_3$, while $MAPbI_3$ cells suffer from deterioration. Double-sided effects of MACl treatment are supposed on the trap formation and passivation. It is revealed that additional deep-trap formation limits the improvement in $MAPbI_3$, while

the shift and reduction of deep traps result in the enhancement for $(Cs_{0.05}FA_{0.79}MA_{0.16})Pb(I_{0.84}Br_{0.16})_3$. From the improved resistance to chemical reaction and trap formation, triple-cation perovskites provide viability for further performance enhancement by post-treatment.

3.2. Experimental Methods

3.2.1. Solar Cell Fabrication

Solar cell is based on the *n-i-p* structure. The compact and porous TiO_2 layer are deposited on SnO_2:F (FTO) substrate. Blocking layer is prepared through the double steps, where the solutions of titanium diisopropoxide *bis*(acetylacetonate) in 1-butanol (150 mM and 300 mM) are spin-coated on the wet-cleaned and UV-O_3 treated FTO substrate. Spin-coating is programmed as 2500 rpm for 20 s (ramp of 2500 rpm/s), and the substrate is sintered at 500°C for 30 min after the drying at each spin-coating (125°C for 20 min). Porous layer is prepared by using the TiO_2 paste (30NR-D, Dyesol) and spin-coating method (4000 rpm for 10 s with ramp of 2000 rpm/s), and the substrate is again sintered at 500°C for 30 min. Both $MAPbI_3$ and $(Cs_{0.05}FA_{0.79}MA_{0.16})Pb(I_{0.84}Br_{0.16})_3$ are deposited using the chlorobenzene dripping method (drip at 5 s before the end of the spin-coating), and annealing is fixed to 100ºC for 60 min. For $MAPbI_3$ precursor, MAI (1.2 M) and PbI_2 (1.2 M) are dissolved in a mixture of DMF and DMSO (volume ratio of 9:1). For triple-cation perovskite, CsI (0.05 M), FAI (1.00 M), PbI_2 (1.05 M), MABr (0.20 M), and $PbBr_2$ (0.20 M) are dissolved in a 4:1 mixture (volume ratio). Spin-coating is programmed as 1000 rpm for 10 s (ramp of 200 rpm/s) followed by 3000 rpm for 20 s (ramp of 2000 rpm/s). Then, the MACl post-treatment is performed as mentioned below. Hole-transport layer is based on the spiro-OMeTAD (72.3 mg/mL in chlorobenzene) with additives of Li-TFSI, FK209 and tBP (final molar ratio of 1.00 : 3.33 : 0.54 : 0.10). An Au electrode is thermally evaporated, and the active area for the solar cell measurement is 0.09 cm^2. Deposition of perovskite, hole-transport material, and MACl treatment are performed in the N_2-glove box.

3.2.2. Post-Treatment by MACl Solution

MACl powder is obtained by recrystallizing methylamine hydrochloride followed by drying under vacuum oven at 70ºC for overnight. The stock solution (9 mM) is prepared by dissolving in anhydrous ethanol/cyclohexane with the volume ratio of 1:3 solution. It is stirred at 45ºC, and spin-coating is performed at 3000 rpm for 20 s (ramp of 3000 rpm/s) with the waiting time for less than 3 s before the spin start. (Prolonged waiting (e.g., 30 s) dissolved the perovskite film, and therefore the waiting time is reduced to minimize the reconstruction by ethanol.) Then, the post-annealing ($T_{Post\text{-}Anneal}$) is controlled as 45ºC, 90ºC, or 110ºC for 10 min.

3.2.3. Characterization

X-ray diffraction (D8 Advance: Bruker) is utilized for the crystal structure analyses. The field-emission scanning electron microscope (Merlin Compact: Carl Zeiss) and scanning transmission electron microscope (JEM-2100F: Jeol) are used for the morphology analyses. Elemental analyses are performed using the built-in energy-dispersive x-ray spectroscopy in electron microscope, wavelength-dispersive x-ray fluorescence (XRF-1800: Shimadzu) using Rh $K\alpha$ (20.216 keV), and x-ray photoelectron spectroscopy (AXIS-His: Kratos) using Al $K\alpha$ (1486.7 eV). For the elemental analyses by electron microscopy, the perovskite film is mechanically peeled-off, followed by dispersion of scratched powders in hexane, and the sample is prepared on the lacey carbon-supported Cu grid. Steady-state and time-resolved photoluminescence spectra (LabRAM HV Evolution: Horiba, FluoTime 300: Picoquant) are obtained using $\lambda_{excitation}$ = 532 and 398 nm lasers, respectively. The film is prepared on a glass substrate with the incident light direction on the perovskite surface. Solar cell performance is characterized using

the solar cell measurement system (K3000: McScience) with a solar simulator (Xenon lamp, air mass 1.5 at 100 mW/cm^2) in the voltage range between -0.1 V and 1.2 V without preconditioning (scan rate of 100 mV/s). Impedance is measured using a potentiostat (Zive SP1: WonATech) in the frequency range between 10 mHz and 100 kHz with an AC amplitude of 10 mV at zero applied bias under dark. The onset of photoemission for the work-function determination is measured at the beamline 4D of Pohang Light Source (PLS-II) using an incident photon energy of 90 eV with -5 V bias on the sample. For the calibration of photon energy, built-in Au foil is used as a reference.

3.3. Results and Discussion

To understand the reactions by the CH_3NH_3Cl (MACl) post-treatment on either $MAPbI_3$ or $(Cs_{0.05}FA_{0.79}MA_{0.16})Pb(I_{0.84}Br_{0.16})_3$ surface (abbreviated as MA or CsFAMA perovskite, where FA is $(NH_2)_2CH$), both crystalline phase and surface morphology are analyzed in Fig. 3-1. Contrary to the impurity-free pristine films (Fig. 3-1(a)), the MACl treatment followed by the post-annealing at 45ºC causes the formation of PbI_2 and Cl-mediated phases [21,22]. As the post-annealing temperature ($T_{Post\text{-}Anneal}$) is increased to 90ºC, these phases have disappeared in both perovskite films, resulting in the impurity-free films as similar to the pristine. Further raise to 110ºC results in the additional formation of PbI_2 for MA perovskite, while it is absent for CsFAMA perovskite. The disappearance of Cl-mediated phases above 90ºC is attributed to the loss of MACl, probably in the form of dissociated species (e.g., CH_3NH_2 and HCl) due to much higher sublimation temperature of MACl itself (i.e. 250°C) [21,22]. Better thermal durability (and accordingly the resistance to decomposition) is expected for CsFAMA perovskite than MA perovskite since the PbI_2 formation is suppressed for CsFAMA at the elevated temperature of 110°C.

Morphological changes in Figs. 3-1(b) and (c) are in line with the diffraction results. (Additional cross-sectional images are provided in Fig. 3-2.) At $T_{Post\text{-}Anneal}$ of 45ºC, clear boundaries between the perovskite grains have disappeared for MA perovskite, and additional microstructures have appeared on the CsFAMA perovskite surface. The morphological changes imply the vulnerability of both perovskites to ethanol (solvent for the MACl dissolution) and the subsequent reconstruction reactions [9,10,13]. While alcoholic solvents are commonly used for the post-treatment, the use

of polar/non-polar solvent mixture would be necessary since it may minimize the potential destructive effects (for example, perovskite dissolution). As $T_{Post\text{-}Anneal}$ is raised to 90ºC, boundaries are again distinctive as similar to the pristine films, and further increase to 110ºC leads to the PbI_2 formation at grain boundaries and surfaces as evidenced from diffraction. Again, the intact morphology beneath the surface implies that the chemical reactions are limited to the film surface (Fig. 3-2).

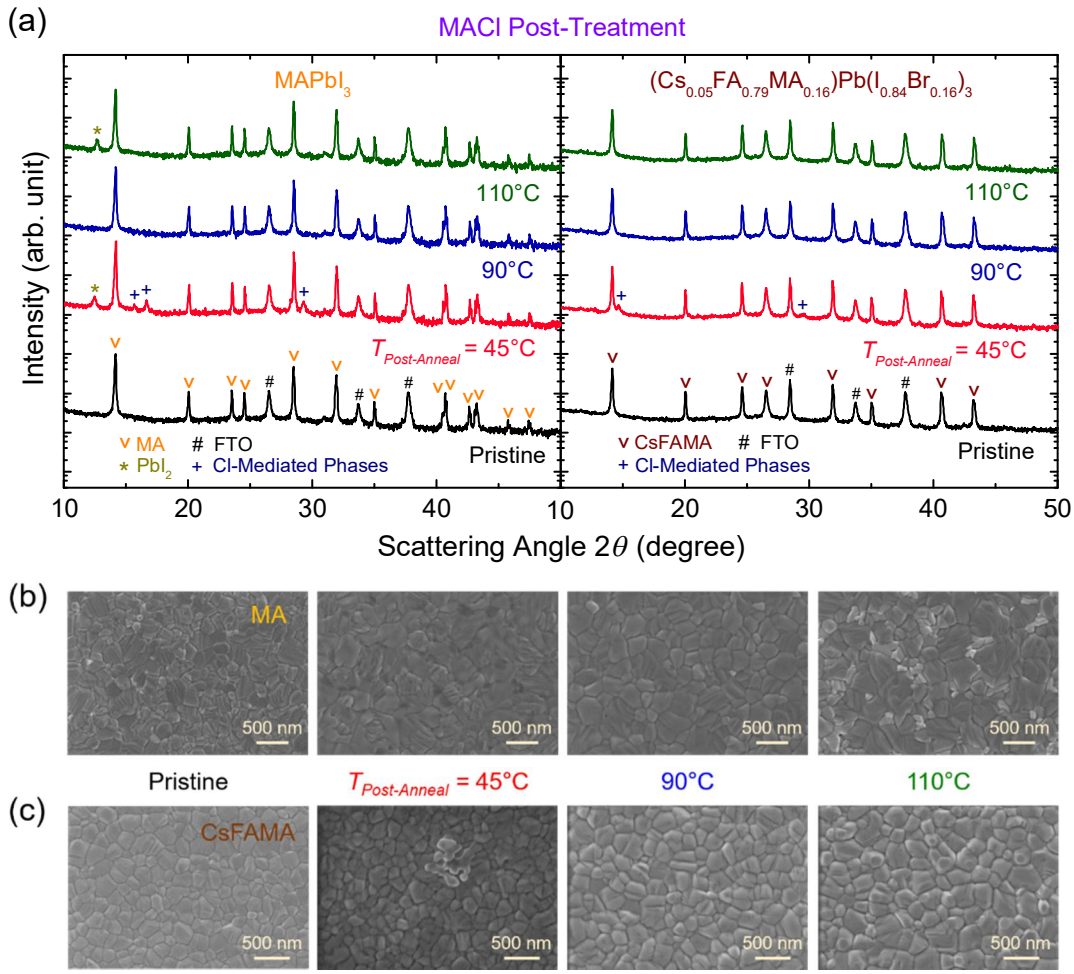

Fig. 3-1. (Color) Crystalline phase and morphological change by the MACl post-treatment. (a) X-ray diffraction of $MAPbI_3$ (abbreviated as MA) and $(Cs_{0.05}FA_{0.79}MA_{0.16})Pb(I_{0.84}Br_{0.16})_3$ (CsFAMA) films, respectively, after the MACl post-treatment with the control of post-annealing temperature ($T_{Post\text{-}Anneal}$) at 45°C, 90°C, and 110°C, and pristine for a reference. Scanning electron microscopy images of (b) $MAPbI_3$ and (c) $(Cs_{0.05}FA_{0.79}MA_{0.16})Pb(I_{0.84}Br_{0.16})_3$ films after the post-treatment.

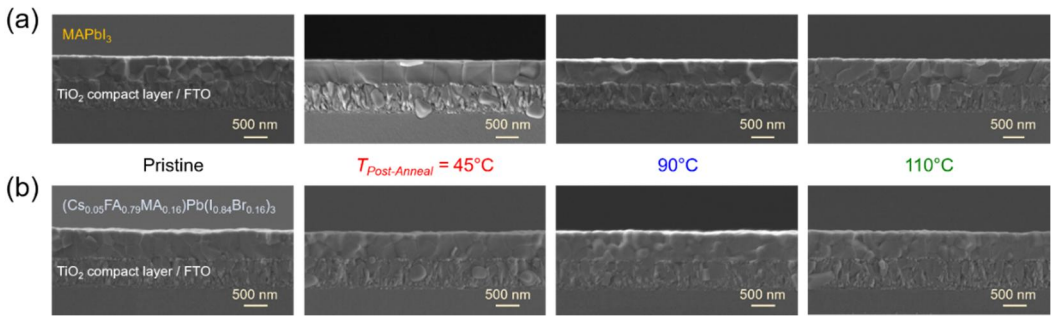

Fig. 3-2. (Color) Cross-sectional images after the MACl post-treatment. (a) Cross-sectional scanning electron microscopy images of $MAPbI_3$ and (b) $(Cs_{0.05}FA_{0.79}MA_{0.16})Pb(I_{0.84}Br_{0.16})_3$ (after Pt coating).

X-ray fluorescence demonstrates the evaporation of Cl during the post-annealing. As shown in Fig. 3-3(a), the Cl $K\alpha$ fluorescence (normalized to Pb $L\beta$) diminishes as $T_{Post\text{-}Anneal}$ increases. However, non-negligible fluorescence is observed at both 90ºC and 110ºC, suggesting other states like amorphous and/or chemisorbed structures rather than the crystalline structures. Elemental analyses are further utilized to characterize the distribution of constituent atoms. Characteristic x-ray spectra (energy-dispersive x-ray spectroscopy of electron microscopy) are analyzed for MA and CsFAMA perovskites in Fig. 3-3(b), and the corresponding maps showing elemental distribution are provided in Figs. 3-3(c) and 3-4(a). Since Cl $K\alpha$ overlaps with Pb $M\gamma$ (~2.63 keV), signal at ~2.6 keV should be scrutinized to confirm its origin [21,23]. Pristine MA (without MACl treatment) is first analyzed and the results are compared with MACl-treated MA, and furthermore different batches of MACl-treated MA are additionally compared (Fig. 3-4(b)). Since perovskites commonly exhibit grain-by-grain inhomogeneity of defect density, the different batches are predicted to have nonuniform Cl concentrations even though the nominally identical experiments are performed [20,24]. As shown in Fig. 3-4(b), signal (~2.6 keV) shows disparity among the different batches of MACl-treated MA (which is normalized to Pb $M\alpha$ of 2.35 keV and $M\beta$ of 2.44 keV), supporting that both Cl $K\alpha$ and Pb $M\gamma$ contribute to the peaks at ~2.6 keV [23].

Furthermore, higher Cl/Pb atomic ratio is correlated to the lower I/Pb ratio (Fig. 3-4(c)). The inverse relation between I and Cl concentration provides the potential reaction pathway (I removal followed by the Cl adsorption), and the reaction is expected to be facilitated by the solvent that is capable for the dissolution of iodide compound. (For example, MAI in ethanol is the precursor for the perovskite deposition [25].) The chemical states of Cl are further discussed in Fig. 3-5. Based on the results of crystalline

and elemental analyses, the perovskite films of post-annealing at 90°C are used in the characterization of photocarrier recombination and solar cells since these films demonstrate the impurity-free phase with the remnant Cl on the surface that the correlation between the surface-property change and the photovoltaic performance could be understood.

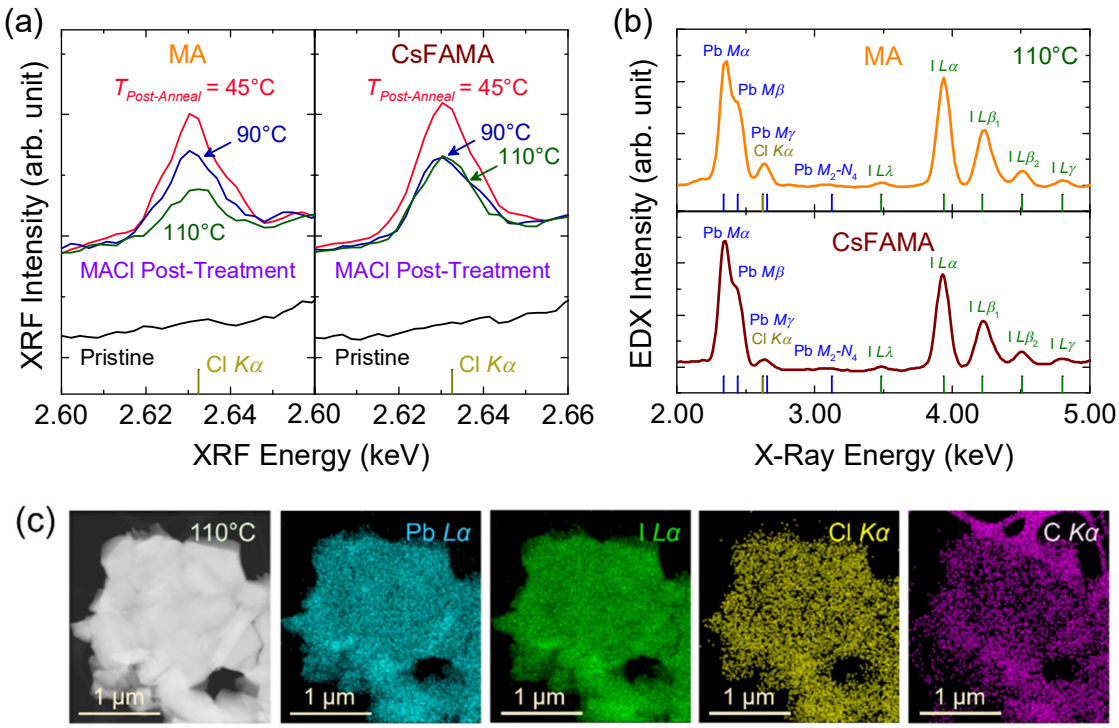

Fig. 3-3. (Color) Elemental analyses and chemisorbed chlorine on the surface. (a) X-ray fluorescence spectra of Cl for the MACl-treated perovskites by different post-annealing temperatures ($T_{Post\text{-}Anneal}$), with pristine for a reference. (b) Energy dispersive x-ray spectra (EDX) of each perovskite after the MACl post-treatment, and (c) EDX mapping of constituent elements for $MAPbI_3$ ($T_{Post\text{-}Anneal}$ = 110°C). (Elemental mapping of MACl-treated $(Cs_{0.05}FA_{0.79}MA_{0.16})Pb(I_{0.84}Br_{0.16})_3$ is in Fig. 3-4.)

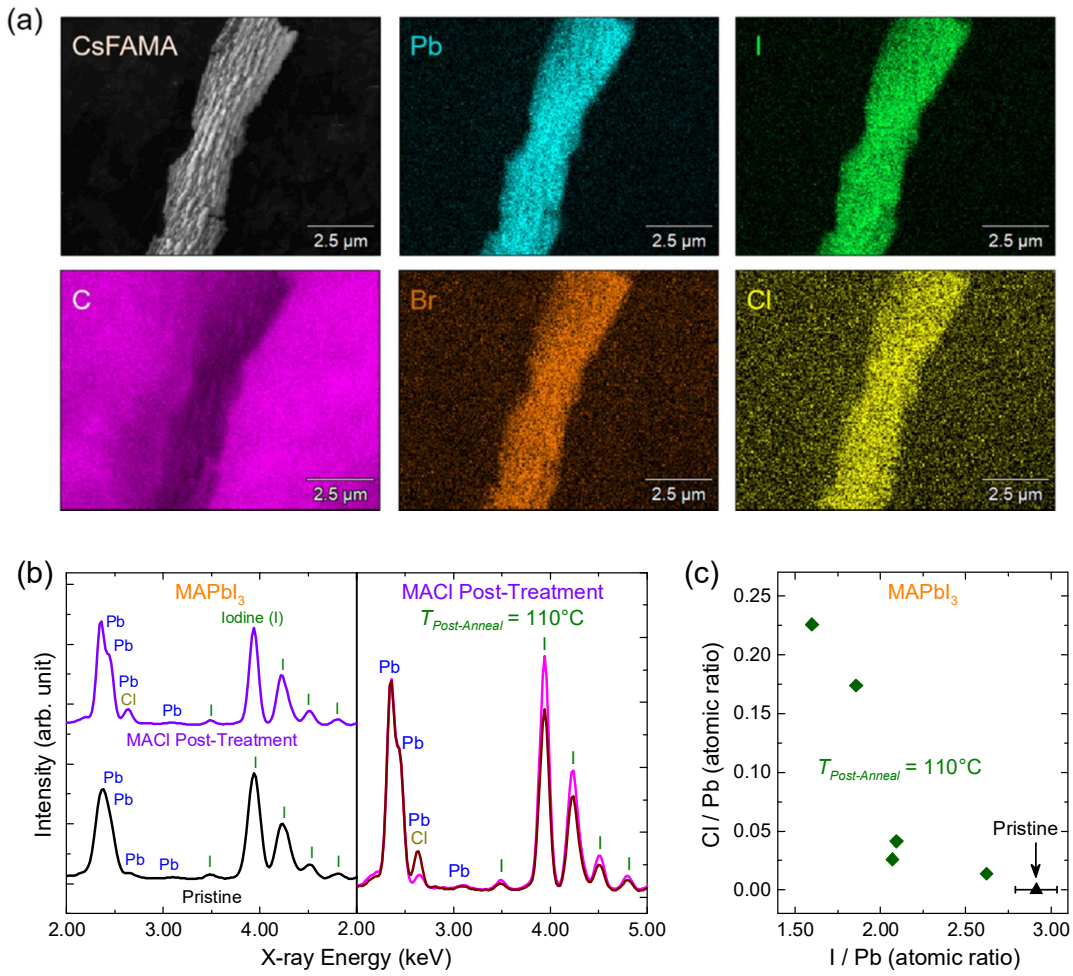

Fig. 3-4. (Color) EDX comparison with pristine and some inhomogeneity of MACl treatment. (a) Elemental mapping of MACl-treated $(Cs_{0.05}FA_{0.79}MA_{0.16})Pb(I_{0.84}Br_{0.16})_3$. (b) (Left) Comparison of energy dispersive x-ray spectra between pristine and MACl-treated $MAPbI_3$ ($T_{Post\text{-}anneal}$ = 110°C). (Right) Comparison between two different samples of MACl-treated $MAPbI_3$ (with the normalized Pb peak). (c) Quantitative relations between Pb, I, and Cl (with an error bar in pristine from the mapping of 3 samples).

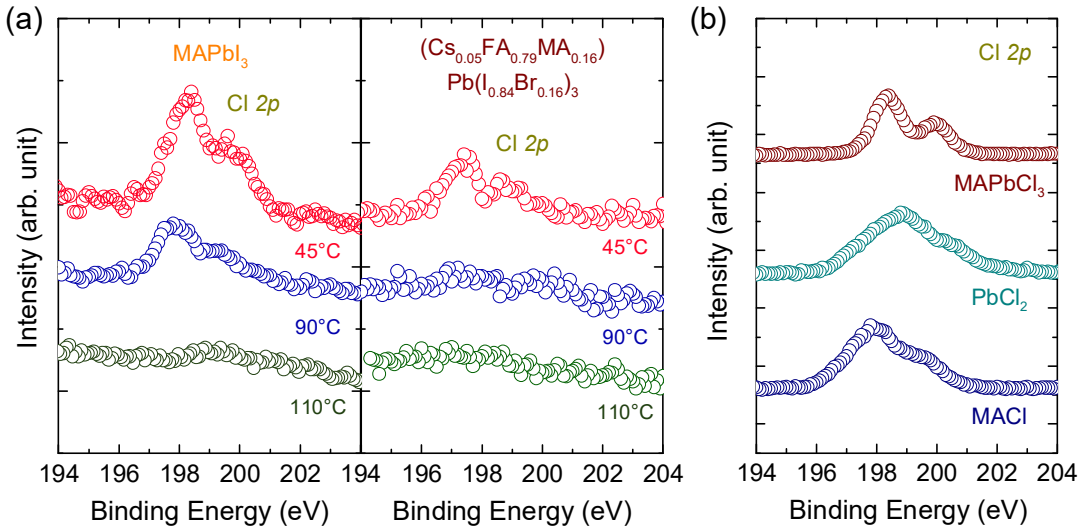

Fig. 3-5. (Color) Variation of chlorine chemical states (Cl 2*p*) in different structures. (a) (Left) Comparison of x-ray photoelectron spectroscopy (XPS) among the MACl-treated $MAPbI_3$ at each post-annealing temperature. (Right) MACl-treated $(Cs_{0.05}FA_{0.79}MA_{0.16})Pb(I_{0.84}Br_{0.16})_3$. (b) Cl 2*p* spectrum in MACl, $PbCl_2$, and $MAPbCl_3$, respectively. Photon energy is calibrated as C 1*s* of 284.5 eV.

The effects of MACl treatment on photoluminescence (PL) properties are summarized in Figs. 3-6, 3-7, and 3-8 [19,26,27]. The MACl treatment results in the blue-shift of PL energy (higher transition energy) in both MA and CsFAMA as shown in Figs. 3-6(a) and (c). Since the disorders/defects in a polycrystalline film induce the band-tail electronic states at the bandedge, the higher or lower PL energy is attributed to the change of electronic structures in the band-tail states. The blue-shift of radiative emission originates from the passivation of defects in the band-tail states (electronically inactive defects) [12,28,29]. By remedying the band-tail traps, PL could be enhanced as shown in the inset of Fig. 3-6(a) for MA. Time-resolved PL demonstrates the slow recombination by the MACl treatment, supporting the suppression of the trap-mediated nonradiative recombination and the consequent increase of radiative recombination (Fig. 3-6(b)). Contrary to MA perovskite, however, CsFAMA perovskite which also shows the blue-shift of PL energy exhibit lower PL after the MACl treatment (Fig. 3-6(c)). Smooth surface and the identical interfaces (glass substrate and air) exclude them as sources of different external PL quantum efficiency [19]. Lower PL efficiency is also observed in time-resolved spectroscopy, where MACl-treated CsFAMA has lower signal compared to the pristine at microsecond (inset of Fig. 3-6(d)).

Radiative recombination necessitates the bimolecular recombination between free e^- and h^+. Low radiative recombination could be due to the mechanisms resulting in the carrier loss of either e^- or h^+ (or both of them). For example, both trap-mediated nonradiative recombination and photocarrier diffusion (either e^- or h^+) lead to the PL quenching [19,30,31]. In that sense, slower decay at sub-microsecond (< 200 ns in Fig. 3-6(d)) followed by the faster decay at microsecond (inset in Fig. 3-6(d)) of MACl-treated CsFAMA than pristine can be understood by lower trap density and higher

photocarrier diffusion after the MACl treatment. Faster photocarrier diffusion is supported by the surface work function analyses (i.e., higher work function for MACl-treated MA than pristine MA as shown in Fig. 3-9). The band bending provides the driving force for the charge separation, and electron diffusion from the film surface towards the interior (i.e., upward band bending) results in the reduction of radiative recombination at the surface [32]. (Band bending is further discussed in the supporting information of Figs. 3-9 and 3-10.) Also, trapped charges in perovskite are known to live as long as microsecond before the recombination with free charges in the band (e.g., trapped e^- and free h^+) [33], suggesting some detrapping of trapped charges. The MACl treatment is additionally performed in $(FA_{0.83}MA_{0.17})Pb(I_{0.83}Br_{0.17})_3$ to confirm the universal properties of tail-state passivation, and the resultant microstructural and optical-property changes are summarized in Fig. 3-8. Intact crystalline structure and the surface morphology confirm the nanoscopic origins for the PL change. The crossing of the time-resolved PL spectra between pristine and MACl-treated FAMA is similar to the case of CsFAMA.

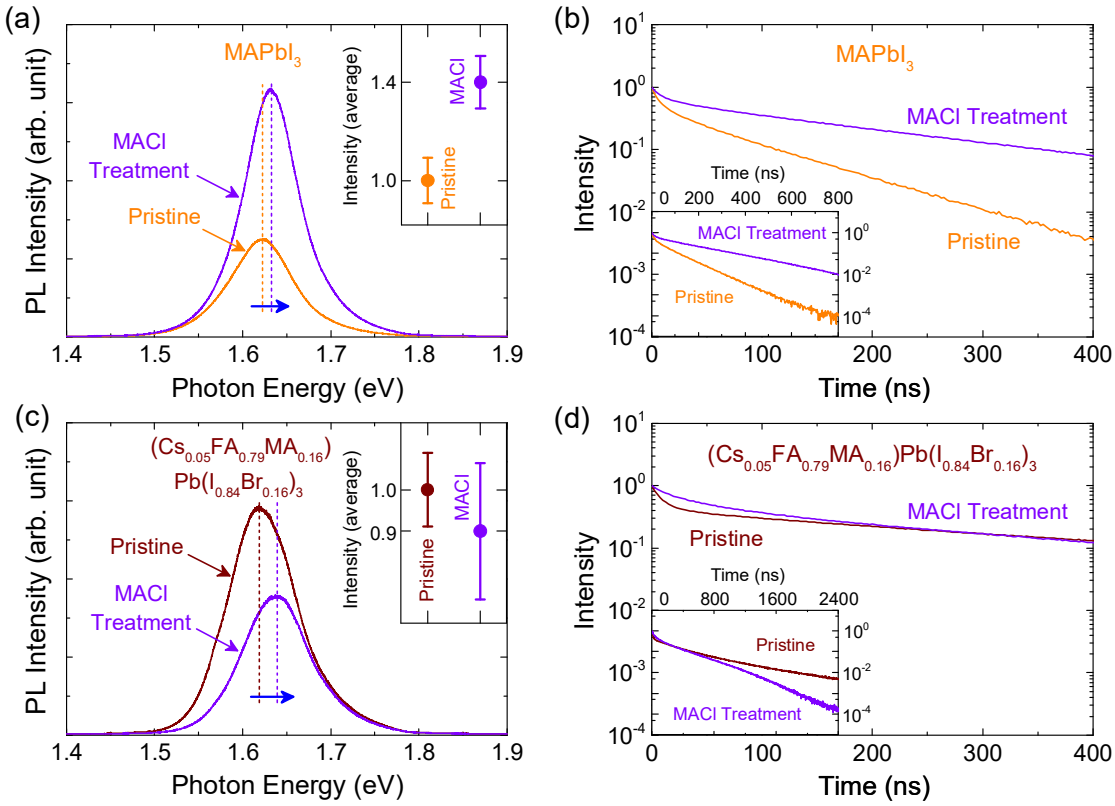

Fig. 3-6. (Color) Photoluminescence (PL) properties and surface passivation. (a) Steady-state PL spectra of pristine and MACl-treated $MAPbI_3$, with the inset for the change of peak intensity (average and standard deviation). Shift of emission peak is marked with a blue arrow. (b) Time-resolved PL spectra with the inset for the extended time scale. (c) Steady-state and (d) time-resolved PL for the MACl post-treatment in $(Cs_{0.05}FA_{0.79}MA_{0.16})Pb(I_{0.84}Br_{0.16})_3$.

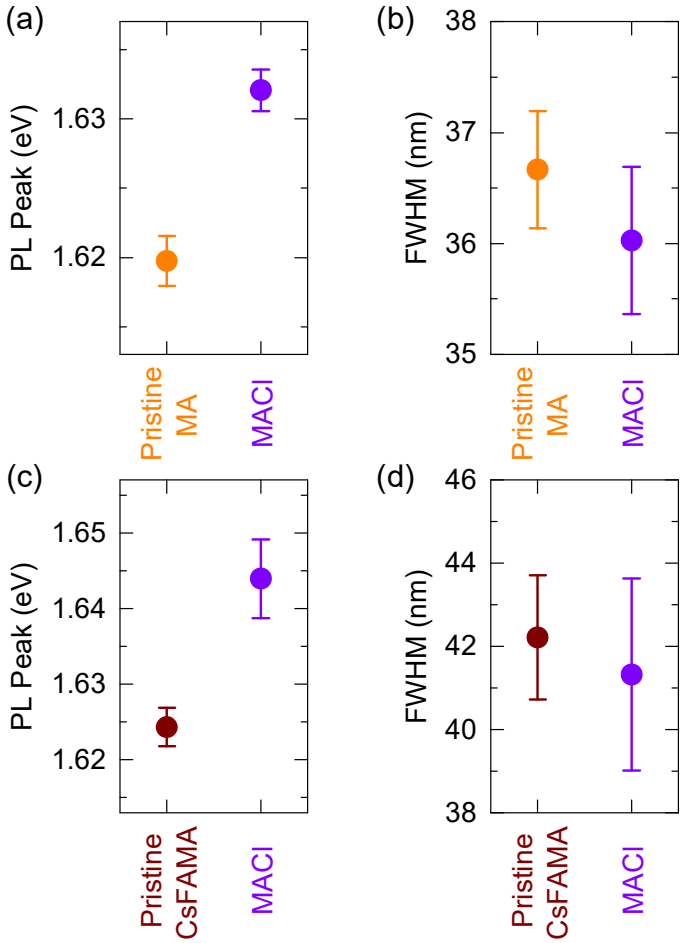

Fig. 3-7. (Color) Photoluminescence-property change by the MACl treatment. (a) Steady-state PL and (b) full width at half-maximum (FWHM) change by MACl treatment in $MAPbI_3$. (c,d) The corresponding data for $(Cs_{0.05}FA_{0.79}MA_{0.16})Pb(I_{0.84}Br_{0.16})_3$.

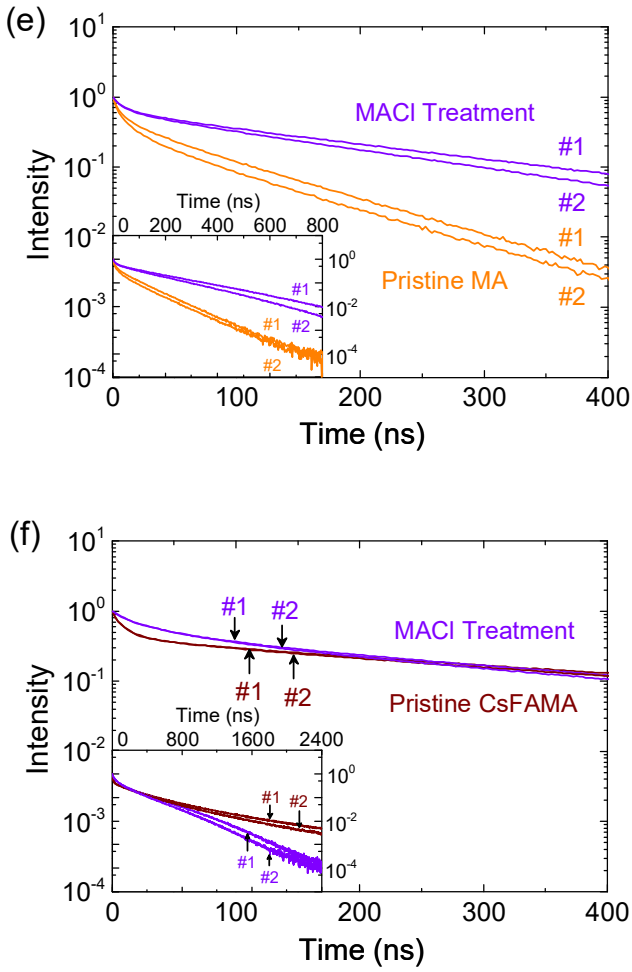

Fig. 3-7. (Color) (Continued) (e) Time-resolved PL spectra of two different samples at each condition for $MAPbI_3$ (arbitrarily labelled as #1 and #2). (f) Two different samples at each condition for $(Cs_{0.05}FA_{0.79}MA_{0.16})Pb(I_{0.84}Br_{0.16})_3$. (#1 and #2 can be clearly distinguished in the inset.)

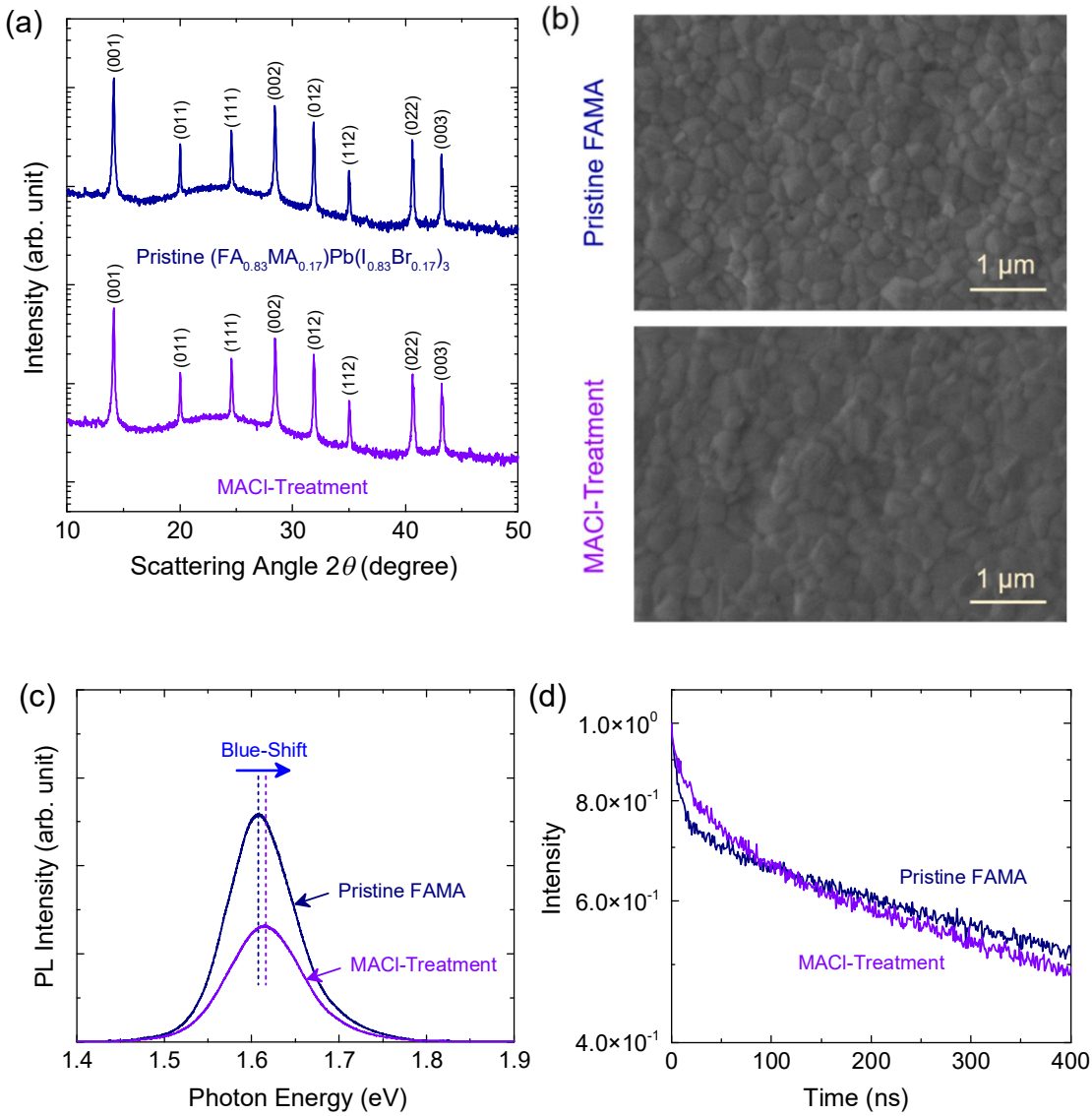

Fig. 3-8. (Color) MACl post-treatment in $(FA_{0.83}MA_{0.17})Pb(I_{0.83}Br_{0.17})_3$ (FAMA). (a) X-ray diffraction, (b) scanning electron microscopy images, (c) steady-state photoluminescence, and (d) time-resolved photoluminescence of pristine and MACl-treated $(FA_{0.83}MA_{0.17})Pb(I_{0.83}Br_{0.17})_3$.

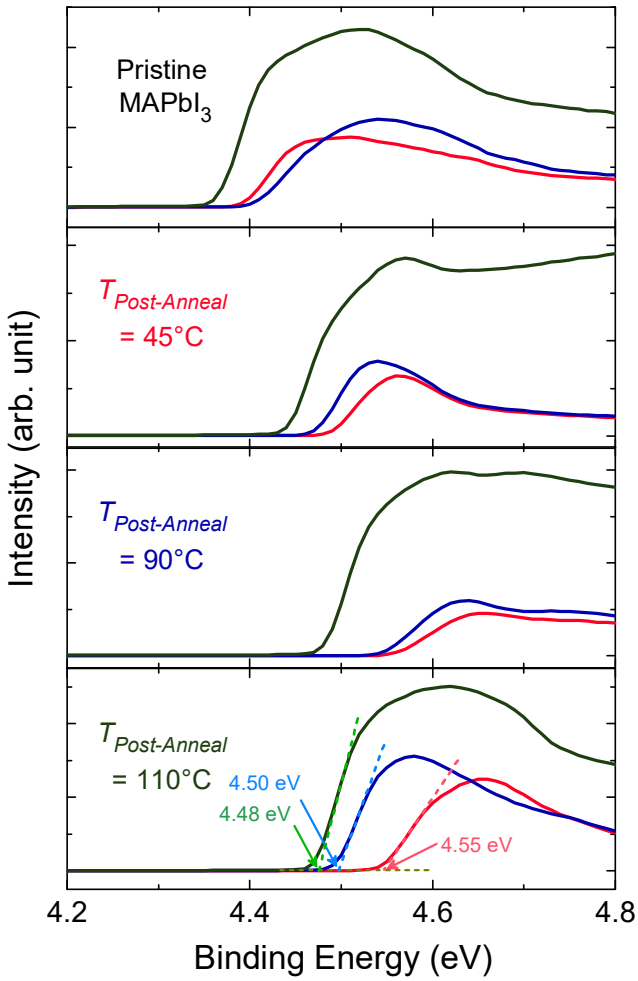

Fig. 3-9. (Color) MACl post-treatment and work function of $MAPbI_3$. Effect of MACl post-treatment on the surface work function of $MAPbI_3$ (post-annealing temperature ($T_{Post\text{-}Anneal}$) between 45°C and 110°C). The measurement sequence is as red, blue, and green (in a different scan region), and photon energy is calibrated by Au work function as 5.1 eV, respectively.

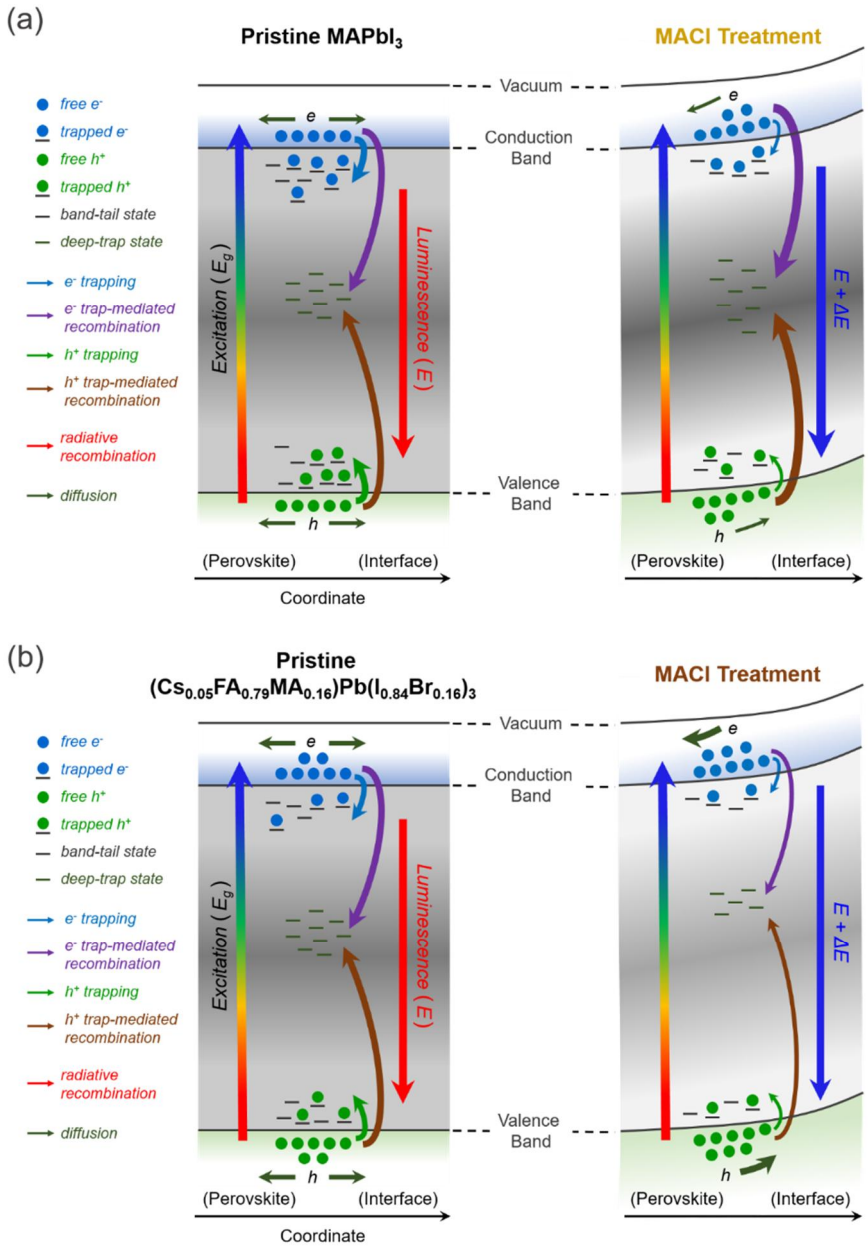

Fig. 3-10. (Color) Double-sided effects of MACl-mediated electronic trap modulation. Schematic illustration for the MACl-treatment effects depending on the perovskite composition (neglecting the surface photovoltage). (a) $MAPbI_3$ and (b) $(Cs_{0.05}FA_{0.79}MA_{0.16})Pb(I_{0.84}Br_{0.16})_3$ cells.

Solar cell performance is compared in Fig. 3-11, and the average cell parameters of short-circuit current density (J_{sc}), open-circuit voltage (V_{oc}), fill factor (FF), and power-conversion efficiency (η) are summarized in Table 3-1. The cell performance has unexpectedly decreased for the MACl-treated MA perovskite. It is counterintuitive to the discussion in PL since the passivation of defects in band-tail states is expected to reduce the nonradiative recombination and thereby increase the cell efficiency. To understand the effects of deep-trap states in the bandgap, trapping/detrapping capacitance is characterized in Fig. 3-11(b) (with linear-scale trap distributions in Fig. 3-12) [34]. MACl-treated MA cells demonstrate the distinctive curvature (like inflection point) while the pristine MA cells show a single transition. Trap distribution spectrum (trap density vs. trap depth against bandedge) exhibits the additional shoulder at ~0.52 eV below the bandedge with the slight reduction of trap density at ~0.67 eV. The recombination via additional deep traps at ~0.52 eV can support the reduction of V_{oc} and η. The unexpected decrease of the cell performance is due to the nanostructural vulnerability of MA perovskite to the polar solvent, which is supported by the inverse relation between iodine and chlorine concentration (Fig. 3-4(c)).

Contrary to MA, CsFAMA cells result in an increase of V_{oc} value (and slight increase of η). For the deep-trap states, MACl-treated CsFAMA cells have shifted the capacitance spectra to higher frequency without altering the spectrum shape of a single transition. Trap analyses demonstrate the shift of deep-trap state toward the bandedge with the reduction of traps at ~0.67 eV, and it supports the performance improvement in addition to the reduction of band-tail states. The opposite results between MA and CsFAMA for the deep-trap formation and reduction, respectively, can be assigned to the different nanostructural durability against the thermal and chemical reactions. Although

the apparent photovoltaic efficiency is increased for CsFAMA, the minute increase of the cell performance raises the issues of perovskite stability against various chemical reactions. This is validated by the decrease of J_{sc} in CsFAMA again, and double-sided effects of trap passivation and formation by the MACl treatment are proposed. (For a reference, both PL enhancement and the deterioration of solar cell performance for $(Cs_{0.05}FA_{0.80}MA_{0.15})Pb(I_{0.85}Br_{0.15})_3$ are reported by Saidaminov *et al.* in Figure S17 of Reference [7]. Also, negligible change of defect structures in $MAPbI_3$ by the MACl post-treatment is proposed by Aristidou *et al.* in Figure 9 of Reference [8].) It provides a message that the versatility for the further performance enhancement could be achieved through the rational selection of solvents for the minimal perovskite reactivity. In summary, double-sided effects of defect passivation and trap formation as well as the band bending of perovskite are summarized in schematic illustration of Fig. 3-10.

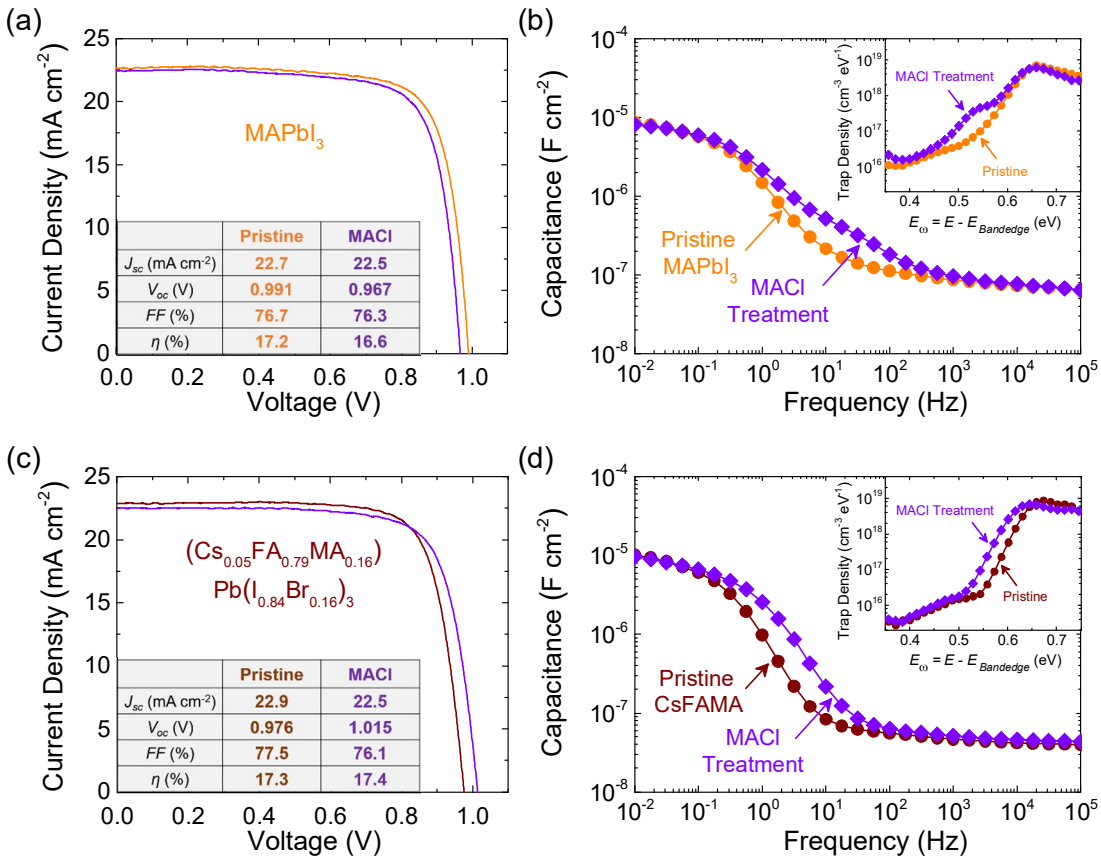

Fig. 3-11. (Color) Solar cell performance and electronic trap characterization. (a) Photovoltaic performance and (b) capacitance with trap analyses (inset) for pristine and MACl-treated $MAPbI_3$ solar cells. (c) *J-V* and (d) capacitance-frequency with trap characterization (inset) for the $(Cs_{0.05}FA_{0.79}MA_{0.16})Pb(I_{0.84}Br_{0.16})_3$ cells. Trap densities in linear scale (for the insets in (b) and (d)) are also shown in Fig. 3-12.

Table 3-1. Solar cell parameters at each perovskite condition. Short-circuit current density (J_{sc}), open-circuit voltage (V_{oc}), fill factor (FF), and power conversion efficiency (η). (a) $MAPbI_3$ and (b) $(Cs_{0.05}FA_{0.79}MA_{0.16})Pb(I_{0.84}Br_{0.16})_3$ solar cells (exhibited in Fig. 3-11), and additional average photovoltaic parameters in the bracket with standard deviation of five cells in each condition.

(a) $MAPbI_3$	J_{sc} (mA cm^{-2})	V_{oc} (V)	FF (%)	η (%)
Pristine	22.7 (22.5 ± 0.4)	0.991 (0.993 ± 0.013)	76.7 (73.4 ± 2.3)	17.2 (16.4 ± 0.5)
MACl-Treatment	22.5 (21.6 ± 1.5)	0.967 (0.966 ± 0.031)	76.3 (74.5 ± 4.2)	16.6 (15.5 ± 0.7)

(b) CsFAMA	J_{sc} (mA cm^{-2})	V_{oc} (V)	FF (%)	η (%)
Pristine	22.9 (23.2 ± 0.4)	0.976 (0.977 ± 0.037)	77.5 (72.9 ± 7.2)	17.3 (16.5 ± 1.8)
MACl-Treatment	22.5 (22.6 ± 0.3)	1.015 (1.004 ± 0.030)	76.1 (76.5 ± 1.4)	17.4 (17.3 ± 0.2)

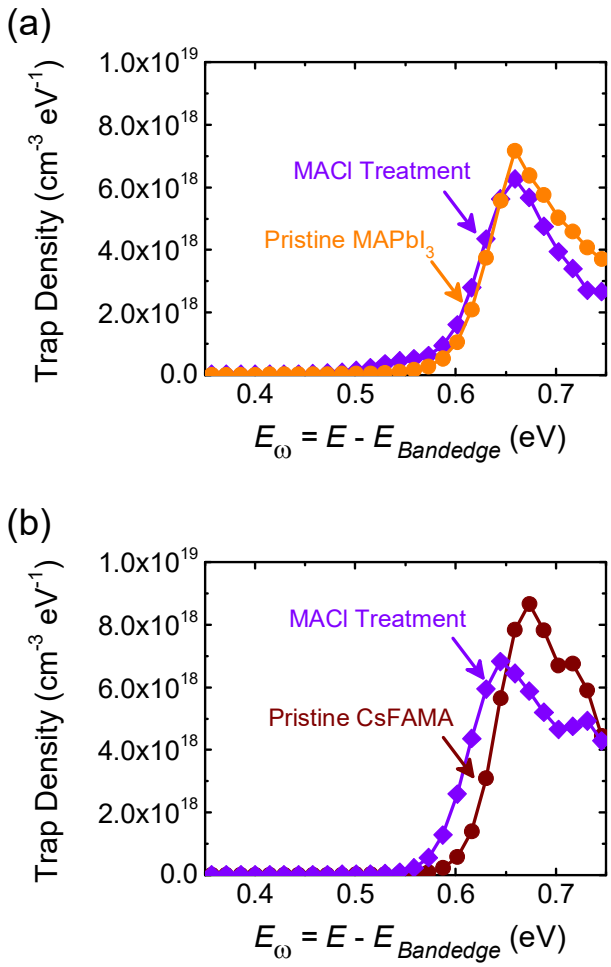

Fig. 3-12. (Color) Linear-scale plot of trap distribution curves in Fig. 3-11. (a) $MAPbI_3$ and (b) $(Cs_{0.05}FA_{0.79}MA_{0.16})Pb(I_{0.84}Br_{0.16})_3$ cells in the insets of Figs. 3-11(b) and (d), respectively.

3.4. Conclusions

Based on the requirement for the minimum energy loss via nonradiative recombination for the efficient solar cells, the MACl surface post-treatment is utilized aiming for the defect reduction and performance improvement in $MAPbI_3$ and $(Cs_{0.05}FA_{0.79}MA_{0.16})Pb(I_{0.84}Br_{0.16})_3$. As a result, the MACl treatment offers the blue-shift of photoluminescence energy regardless of perovskite composition, suggesting the passivation of defects in the band-tail states for remedying the electronically-active defects. However, the opposite results between $MAPbI_3$ and $(Cs_{0.05}FA_{0.79}MA_{0.16})Pb(I_{0.84}Br_{0.16})_3$ are observed in the photovoltaic performance. It presents the implications on the MACl treatment that double-sided effects are supposed for the positive and negative influences. Beneficial impact is provided by the passivation of defects in the tail states. However, perovskites susceptible to the chemical reaction are prone to the additional defect formation as evidenced by the deep-trap characterization. In that sense, the improved resistance of triple-cation-based perovskites will provide viability for the further performance enhancement through the post-treatment.

3.5. References

1. Polman, A.; Knight, M.; Garnett, E. C.; Ehrler, B.; Sinke, W. C. Photovoltaic Materials: Present Efficiencies and Future Challenges. *Science* **2016**, *352*, aad4424.
2. Hwang, T.; Lee, B.; Kim, J.; Lee, S.; Gil, B.; Yun, A. J.; Park, B. From Nanostructural Evolution to Dynamic Interplay of Constituents: Perspectives for Perovskite Solar Cells. *Adv. Mater.* **2018**, *30*, 1704208.
3. Lee, B.; Lee, S.; Cho, D.; Kim, J.; Hwang, T.; Kim, K. H.; Hong, S.; Moon, T.; Park, B. Evaluating the Optoelectronic Quality of Hybrid Perovskites by Conductive Atomic Force Microscopy with Noise Spectroscopy, *ACS Appl. Mater. Interfaces* **2016**, *8*, 30985-30991.
4. Cho, D.; Hwang, T.; Cho, D.-G.; Park, B.; Hong, S. Photoconductive Noise Microscopy Revealing Quantitative Effect of Localized Electronic Traps on the Perovskite-Based Solar Cell Performance, *Nano Energy* **2018**, *9*, 29-36.
5. Park, H. H.; Heasley, R.; Sun, L.; Steinmann, V.; Jaramillo, R.; Hartman, K.; Chakraborty, R.; Sinsermsuksakul, P.; Chua, D.; Buonassisi, T.; Gordon, R. G. Co-Optimization of SnS Absorber and Zn(O,S) Butter Materials for Improved Solar Cells, *Prog. Photovolt: Res. Appl.* **2015**, *23*, 901-908.
6. Chen, Z.; Dong, Q.; Liu, Y.; Bao, C.; Fang, Y.; Lin, Y.; Tang, S.; Wang, Q.; Xiao, X.; Bai, Y. *et al.* Thin Single Crystal Perovskite Solar Cells to Harvest Below-Bandgap Light Absorption. *Nat. Commun.* **2017**, *8*, 1890.
7. Saidaminov, M. I.; Kim, J.; Jain, A.; Quintero-Bermudez, R.; Tan, H.; Long, G.; Tan, F.; Johnston, A.; Zhao, Y.; Voznyy, O. *et al.* Suppression of Atomic Vacancies via Incorporation of Isovalent Small Ions to Increase the Stability of Halide Perovskite

Solar Cells in Ambient Air. *Nat. Energy* **2018**, *3*, 648-654.

8. Aristidou, N.; Eames, C.; Sanchez-Molina, I.; Bu, X.; Kosco, J.; Islam, M. S.; Haque, S. A. Fast Oxygen Diffusion and Iodide Defects Mediate Oxygen-Induced Degradation of Perovskite Solar Cells. *Nat. Commun.* **2017**, *8*, 15218.
9. Noel, N. K.; Habisreutinger, S. N.; Wenger, B.; Klug, M. T.; Ho¨rantner, M. T.; Johnston, M. B.; Nicholas, R. J.; Moore, D. T.; Snaith, H. J. A Low Viscosity, Low Boiling Point, Clean Solvent System for the Rapid Crystallisation of Highly Specular Perovskite Films. *Energy Environ. Sci.* **2017**, *10*, 145-152.
10. Uribe, J. I.; Ciro, J.; Montoya, J. F.; Osorio, J.; Jaramillo, F. Enhancement of Morphological and Optoelectronic Properties of Perovskite Films by CH_3NH_3Cl Treatment for Efficient Solar Minimodules. *ACS Appl. Energy Mater.* **2018**, *1*, 1047-1052.
11. Leijtens, T.; Prasanna, R.; Bush, K. A.; Eperon, G. E.; Raiford, J. A.; Gold-Parker, A.; Wolf, E. J.; Swifter, S. A.; Boyd, C. C.; Wang, H.-P. *et al.* Tin-Lead Halide Perovskites with Improved Thermal and Air Stability for Efficient All-Perovskite Tandem Solar Cells. *Sustainable Energy Fuels* **2018**, *2*, 2450-2459.
12. Xie, F.; Chen, C.-C.; Wu, Y.; Li, X.; Cai, M.; Liu, X.; Yang, X.; Han, L. Vertical Recrystallization for Highly Efficient and Stable Formamidinium-Based Inverted-Structure Perovskite Solar Cells. *Energy Environ. Sci.* **2017**, *10*, 1942-1949.
13. Yang, M.; Zhang, T.; Schulz, P.; Li, Z.; Li, G.; Kim, D. H.; Guo, N.; Berry, J. J.; Zhu, K.; Zhao, Y. Facile Fabrication of Large-Grain $CH_3NH_3PbI_{3-x}Br_x$ Films for High-Efficiency Solar Cells via CH_3NH_3Br Selective Ostwald Ripening. *Nat. Commun.* **2016**, *7*, 12305.
14. Liu, Z.; Qiu, L.; Juarez-Perez, E. J.; Hawash, Z.; Kim, T.; Jiang, Y.; Wu, Z.; Raga,

S. R.; Ono, L. K.; Liu, S. *et al.* Gas-Solid Reaction Based over One-Micrometer Thick Stable Perovskite Films for Efficient Solar Cells and Modules. *Nat. Commun.* **2018**, *9*, 3880.

15. Hangarter, C. M.; Debnath, R.; Ha, J. Y.; Sahiner, M. A.; Reehil, C. J.; Manners, W. A.; Josell, D. Photocurrent Mapping of 3D CdSe/CdTe Windowless Solar Cells. *ACS Appl. Mater. Interfaces* **2013**, *5*, 9120-9127.
16. Khadka, D. B.; Shirai, Y.; Yanagida, M.; Masuda, T.; Miyano, K. Enhancement in Efficiency and Optoelectronic Quality of Perovskite Thin Films Annealed in MACl Vapor. *Sustainable Energy Fuels* **2017**, *1*, 755-766.
17. Gordillo, G.; Otalora, C. A.; Reinoso, M. A. Trap Center Study in Hybrid Organic-Inorganic Perovskite Using Thermally Stimulated Current (TSC) Analyses. *J. Appl. Phys.* **2017**, *122*, 075304.
18. Kim, S.-G.; Chen, J.; Seo, J.-Y.; Kang, D.-H.; Park, N.-G. Rear-Surface Passivation by Melaminium Iodide Additive for Stable and Hysteresis-Less Perovskite Solar Cells. *ACS Appl. Mater. Interfaces* **2018**, *10*, 25372-25383.
19. Richter, J. M.; Abdi-Jalebi, M.; Sadhanala, A.; Tabachnyk, M.; Rivett, J. P. H.; Pazos-Outon, L. M.; Godel, K. C.; Price, M.; Deschler, F.; Friend, R. H. Enhancing Photoluminescence Yields in Lead Halide Perovskites by Photon Recycling and Light Out-Coupling. *Nat. Commun.* **2016**, *7*, 13941.
20. Hwang, T.; Cho, D.; Kim, J.; Kim, J.; Lee, S.; Lee, B.; Kim, K. H.; Hong, S.; Kim, C.; Park, B. Investigation of Chlorine-Mediated Microstructural Evolution of $CH_3NH_3PbI_3$(Cl) Grains for High Optoelectronic Responses. *Nano Energy* **2016**, *25*, 91-99.
21. Unger, E. L.; Bowring, A. R.; Tassone, C. J.; Pool, V. L.; Gold-Parker, A.;

Cheacharoen, R.; Stone, K. H.; Hoke, E. T.; Toney, M. F.; McGehee, M. D. Chloride in Lead Chloride-Derived Organo-Metal Halides for Perovskite-Absorber Solar Cells. *Chem. Mater.* **2014**, *26*, 7158-7165.

22. Yu, H.; Wang, F.; Xie, F.; Li, W.; Chen, J.; Zhao, N. The Role of Chlorine in the Formation Process of "$CH_3NH_3PbI_{3-x}Cl_x$" Perovskite. *Adv. Funct. Mater.* **2014**, *24*, 7102-7108.
23. Zschornack, G. *Handbook of X-Ray Data*; Springer: Berlin, Germany. 2007.
24. DeQuilettes, D. W.; Vorpahl, S. M.; Stranks, S. D.; Nagaoka, H.; Eperon, G. E.; Ziffer, M. E.; Snaith, H. J.; Ginger, D. S. Impact of Microstructure on Local Carrier Lifetime in Perovskite Solar Cells. *Science* **2016**, *348*, 683-686.
25. Kim, J.; Hwang, T.; Lee, S.; Lee, B.; Kim, J.; Jang, G. S.; Nam, S.; Park, B. Solvent and Intermediate Phase as Boosters for the Perovskite Transformation and Solar Cell Performance. *Sci. Rep.* **2016**, *6*, 25648.
26. Polman, A.; Atwater, H. Photonic Design Principles for Ultrahigh-Efficiency Photovoltaics. *Nat. Mater.* **2012**, *11*, 174-177.
27. Sarritzu, V.; Sestu, N.; Marongiu, D.; Chang, X.; Masi, S.; Rizzo, A.; Colella, S.; Quochi, F.; Saba, M.; Mura, A. *et al.* Optimal Determination of Shockley-Read-Hall and Interface Recombination Currents in Hybrid Perovskites. *Sci. Rep.* **2017**, *7*, 44629.
28. DeQuilettes, D. W.; Koch, S.; Burke, S.; Paranji, R. K.; Shropshire, A. J.; Ziffer, M. E.; Ginger, D. S. Photoluminescence Lifetimes Exceeding 8 μs and Quantum Yields Exceeding 30% in Hybrid Perovskite Thin Films by Ligand Passivation. *ACS Energy Lett.* **2016**, *1*, 438-444.
29. Shao, Y.; Xiao, Z.; Bi, C.; Yuan, Y.; Huang, J. Origin and Elimination of

Photocurrent Hysteresis by Fullerene Passivation in $CH_3NH_3PbI_3$ Planar Heterojunction Solar Cells. *Nat. Commun.* **2014**, *5*, 5784.

30. Ding, J.; Lian, Z.; Li, Y.; Wang, S.; Yan, Q. The Role of Surface Defects in Photoluminescence and Decay Dynamics of High-Quality Perovskite $MAPbI_3$ Single Crystals. *J. Phys. Chem. Lett.* **2018**, *9*, 4221-4226.
31. Park, S. Y.; Baek, M. Y.; Ju, Y.; Kim, D. H.; Moon, C. S.; Noh, J. H.; Jung, H. S. Simultaneous Ligand Exchange Fabrication of Flexible Perovskite Solar Cells using Newly Synthesized Uniform Tin Oxide Quantum Dots. *J. Phys. Chem. Lett.* **2018**, *9*, 5460-5467.
32. Kim, D.; Kim, G. Y.; Ko, C.; Pae, S. R.; Lee, Y. S.; Gunawan, O.; Ogletree, D. F.; Jo, W.; Shin, B. Effects of Postsynthesis Thermal Conditions on Methylammonium Lead Halide Perovskite: Band Bending at Grain Boundaries and its Impacts on Solar Cell Performance. *J. Phys. Chem. C* **2016**, *120*, 21330-21335.
33. Leijtens, T.; Eperon, G. E.; Barker, A. J.; Grancini, G.; Zhang, W.; Ball, J. M.; Kandada, A. R. S.; Snaith, H. J.; Petrozza, A. Carrier Trapping and Recombination: The Role of Defect Physics in Enhancing the Open Circuit Voltage of Metal Halide Perovskite Solar Cells. *Energy Environ. Sci.* **2016**, *9*, 3472-3481.
34. Lin, Y.-R.; Tunuguntla, V.; Wei, S.-Y.; Chen, W.-C.; Wong, D.; Lai, C.-H.; Liu, L.-K.; Chen, L.-C.; Chen, K.-H. Bifacial Sodium-Incorporated Treatments: Tailoring Deep Traps and Enhancing Carrier Transport Properties in Cu_2ZnSnS_4 Solar Cells. *Nano Energy* **2015**, *16*, 438-445.

Appendix 1.

Investigation of Chlorine-Mediated Microstructural Evolution of $CH_3NH_3PbI_3(Cl)$ Grains for High Optoelectronic Responses

A.1.1. Introduction

An organic-inorganic hybrid perovskite is considered as a next generation solar cell material, and the perovskite solar cell has reached ~20% high power conversion efficiency recently [1]. Its high absorption coefficient, low exciton binding energy, long charge carrier diffusion length, and low trap density enable the methylammonium lead iodide perovskite ($MAPbI_3$: triiodide perovskite) to be an excellent material as a light harvester. The basic principles lying in the superior solar cell performance are the high charge generation in the light harvesting material, and facile separation followed by the collection of generated charges into each electrode without the significant loss through the recombination [2]. Since $MAPbI_3$ phase intrinsically meets these demands for high cell performance, many strategies have been attempted to improve the power conversion efficiency, mainly focusing on the fine tuning of crystallinity, morphology, and the composition [3-5]. Several earlier studies reported on the improvement of the overall perovskite quality by reducing the intrinsic traps and minimizing any recombination paths

---

*The work presented in Appendix 1 was published in *Nano Energy* **25**, 91 (2016) entitled,
"Investigation of Chlorine-Mediated Microstructural Evolution of $CH_3NH_3PbI_3(Cl)$ Grains for High Optoelectronic Responses"
Taehyun Hwang, Duckhyung Cho, Jinhyun Kim, Jaewon Kim, Sangheon Lee, Byungho Lee, Kyung Hwan Kim, Seunghun Hong, Chunjoong Kim, and Byungwoo Park*

in the cell through complete coverage [6-9]. To resolve these, various synthesis methods such as vapor deposition, vapor-assisted solution process, and liquid solution process have been introduced [10-13]. Also, the compositional variation is investigated by replacing the constituents of $MAPbI_3$ with alternative cations/anions like Sn^{2+}, $HC(NH_2)^{2+}$, Br^-, or Cl^- to alter the optical properties [14-17].

Especially, the role of chlorine in the physicochemical evolution of the $MAPbI_3$ phase is one of the most appealing topics. Morphological effects including preferential orientation, crystallinity improvement, and large grain evolution are commonly observed. However, the compositional effects such as doping in the bulk, passivation at the grain boundary, bonding at the interface of the TiO_2 electrode, etc. have been reported with various possibilities [18-25]. Considering that reactions among the starting compounds and the phase transformations of the constituents from the liquid solution to the solid perovskite film give an indication of the functions of ionic species in the precursor solution, and finally the composition and nanostructures in the solid films, precursor characterization is thus of top priority in deeply understanding the crystallization of the perovskite phase [26-30]. Unveiling the details of the reactions and fundamental phase transformations from the elementary step, i.e. basic recipe of MAI and $PbCl_2$ mixing (hereafter referred as mixed-halide solution, and resulting perovskite as mixed-halide perovskite or $MAPbI_3(Cl)$) will provide a key to understand the role of chlorine. Besides the microstructural effects, the optoelectronic role of chlorine and its relation with the nanostructural chemistry are the essence parameters comprising the high solar cell performance. Conductive-probe AFM (*c*AFM) can measure the current from each grain by directly contacting with the conductive probe, and it is proven to be a powerful tool for characterizing the electronic properties of the light harvesting materials such as CIGS, CZTS, CdTe, $MAPbI_3$, etc. [31-38].

Simultaneous mapping of the microcrystalline topography with the optoelectronic response from each grain will reveal the electronic role of chlorine directly by comparing the different compositional perovskites.

Herein, the microstructural evolution of $MAPbI_3(Cl)$ grain was scrutinized, specifically focusing on the identification of the ionic components in the mixed-halide precursor solution and the equilibrium shift therein. The as-deposited mixed-halide perovskite film was annealed at different temperatures to monitor the chlorine effect, and the simple temperature control gave an evidence of chlorine remaining in the mixed-halide perovskite from x-ray diffraction and fluorescence analyses. Finally, the role of chlorine on the optoelectronic properties and the noise characteristics, which is for the first time to our knowledge, was examined. Consequently, the existing chlorine led to the 30-times increased photocurrent and decrease of recombination centers in $MAPbI_3(Cl)$ compared with $MAPbI_3$.

A.1.2. Experimental Methods

A.1.2.1. CH_3NH_3I Synthesis

CH_3NH_3I (MAI) was synthesized from mixing the CH_3NH_2 solution and the HI solution by 1:1 molar ratio in a round-bottom flask at 0 °C for 2 h under stirring. The solvent was evaporated, and the precipitate was washed with diethyl ether for 3 times and then further washed with the 1:1 vol. ratio mixture of anhydrous ethanol and diethyl ether. The precipitate was dried at 60 °C for 24 h in a vacuum oven.

A.1.2.2. PbI_2 Pre-Coating and Perovskite Deposition

For mixed-halide perovskite precursor solution, MAI (2.64 M) and $PbCl_2$ (0.88 M) were dissolved in *n*,*n*-dimethylformamide (DMF) and the solution was stirred at 100°C for 10 min. The selection of the temperature and the time for the heating were critical for the perovskite film formation since the high temperature heating induced the color change of the solution from yellow to dark brown by the formation of triiodide ion which blocked the perovskite crystallization from charge imbalance of triiodide ion. Dissolved oxygen reacted with I^- ion and H^+ resulting I_3^- ion and H_2O formation, and therefore the preheating conditions for the solution were carefully chosen [39]. For triiodide precursor solution, MAI and PbI_2 with identical concentrations to the mixed halide solution were dissolved in DMF and the solution was stirred at the same condition. Prior to the conventional one-step perovskite deposition, the PbI_2 pre-coating was performed by spin coating the 1.0 M of PbI_2 solution (DMF) on the porous TiO_2 electrode (TiO_2 on FTO). The PbI_2 solution was preheated at 100 °C and vigorously stirred to disperse the PbI_2 particles in the solution uniformly, and the TiO_2 substrate was preheated likewise to prevent the supersaturation of the solution drop. The pre-coated PbI_2 layer was then dried to remove the remaining

solvent at 70 °C for 30 min. Perovskite precursor solution (either triiodide or mixed halide) was spin-coated at 2000 rpm for 60 s on the PbI_2 precoated layer or the TiO_2 substrate, and the films were annealed at 100 °C for 50 min. To check the x-ray peak shift, mixed-halide perovskite was annealed differently where annealing temperature was controlled from 90°C to 160°C with 10°C interval at constant annealing time. Further analyses were examined from the perovskite made using pre-coating method except for the perovskite with specially mentioned. All the perovskite deposition was processed in air, and the films were kept under dark and vacuum conditions before the analyses.

A.1.2.3. Characterization

The extinction of the precursor solution was recorded through a UV–vis spectrophotometer (Cary 5000: Agilent Technologies). For mixed halide solution, the concentration of $PbCl_2$ was varied from 305 μM to 20 mM while constantly maintaining the 3:1 molar ratio between MAI and $PbCl_2$. The solutions were pretreated identically to the film deposition condition before the measurement. Triiodide precursor solution was made by dissolving 100:1 molar ratio between MAI and PbI_2 with the concentration of 260 μM (PbI_2), and the chosen of 100:1 molar ratio was to clearly distinguish both the PbI_3^- and PbI_4^{2-} complexes [26]. The PbI_2 solution (in DMF) was measured as a reference for comparison.

The crystal structure was examined by x-ray diffraction (XRD) (D8 Advance: Bruker). Wavelength-dispersive x-ray fluorescence (WDXRF) (XRF-1800: Shimadzu) using Rh $K\alpha$ as x-ray source (20.216 keV) was adopted to analyze the elements in the perovskite film, and the analyzing single crystals were LiF (200) and Ge (111). The surface was analyzed by x-ray photoelectron spectroscopy (XPS) (AXIS-His: Kratos) using

Al *Kα* x-ray (1486.7 eV). The field-emission scanning electron microscope (FESEM) (Merlin Compact: Zeiss) was used to observe the film morphology. An atomic force microscope (AFM) instrument (XE-70: Park System) was utilized to measure the topography and photocurrent maps on the perovskite film. A conductive Pt probe (25Pt300B: Park System) installed on the AFM was in direct contact with the surface of the perovskite sample. The contact force between the AFM probe and the surface was maintained to ~1.5 μN during the measurements by using an AFM force feedback circuit. To induce the photocurrents, a white light of ~10 mW cm^2 (LS-F100HS: Seokwang Optical) was illuminated on the sample with a dc bias of 1.2 V between the tip and the TiO_2/FTO substrate using a function generator (DS345: Stanford Research Systems). The photocurrent signal was amplified by a low-noise preamplifier (SR570: Stanford Research Systems), and the signals were collected during the AFM scanning of the perovskite film to obtain the photocurrent map simultaneously with the topography map. The scan rate was ~0.20 Hz, and all measurements were conducted in an ambient condition with a closed box to block stray lights. Noise vs. frequency spectra were measured by positioning the tip at the perovskite domain with the identical bias. The power spectral density (PSD) spectra of the amplified current signals were measured using a fast Fourier transform (FFT) network analyzer (SR770: Stanford Research Systems). The current-normalized noise PSD spectra were obtained by normalizing the PSD spectra with respect to the power of the photocurrents.

A.1.3. Results and Discussion

To understand the perovskite crystallization, the precursors were scrutinized to identify the effects of solution constituents on the microstructure evolution. When PbI_2 and MAI are dissolved in DMF, plumbate $PbI_x^{(x-2)-}$ complexes are formed through van der Waals interactions between the I-terminated PbI_2 crystals and ionized I ions from MAI [26,27]. The absorption onset of the mixed-halide solution was similar to that of triiodide solution (Fig. A1-1(a)). In triiodide solution, PbI_4^{2-} and PbI_3^- are featured distinctively as much higher concentration of MAI are dissolved than PbI_2 (100:1 molar ratio of MAI:PbI_2). Basic recipe of 3:1 molar ratio between MAI and $PbCl_2$, however, resulted in the appearance of absorption plateau below 430 nm, and characteristic absorption peaks were difficult to distinguish while the peak positions seemed to be almost maintained. From the possibility of Pb-I complex formation through the ion-exchange reaction between Cl and I, the fitting was performed with the PbI_4^{2-} and the PbI_3^- absorption (pink triangle and green square lines in Fig. A1-1(a)). The curvature near the peak of PbI_4^{2-} for the mixed-halide solution indicated the formation of Pb-I complex by the ion-exchange as expected. However, the complicated plateau region should be further investigated. In order to examine the absorption behavior, the concentration of the mixed-halide solution was controlled at the constant 3:1 molar ratio of MAI and $PbCl_2$ to observe the shift in equilibrium between the products from the MAI and $PbCl_2$ mixing and the solvent (Fig. A1-1(b)). As the $PbCl_2$ concentration was varied in mixed halide solution, peak intensities from PbI_3^- (370 nm) and PbI_4^{2-} (425 nm) followed a quadratic (bimolecular reaction) dependence on the $PbCl_2$ concentration (Figs. A1-1(c) and (d)). Based on these results, yellowish mixed-halide solution originates from the $PbI_x^{(x-2)-}$ complex from $PbCl_2$ and MAI. $PbI_x^{(x-2)-}$ reacts with DMF

differently as a concentration, and the reaction of $PbI_x^{(x-2)-}$ complex in DMF indicates that the complex decomposes at low concentration. The complex in DMF increases quadratically in the early stage, and absorbs completely below 430 nm as the concentration of precursor solution increases, resulting in the absorption plauteau. The occurrence of yellow color in the mixed-halide solution and the possible reactions between $PbI_x^{(x-2)-}$ complex and polar DMF solvent depending on the concentrations are summarized as follows:

$$PbCl_2 + x\ MAI \rightarrow [PbI_x^{(x-2)-} \cdots Cl^-] + x\ MA^+ + Cl^- \quad (1)$$

$$[PbI_x^{(x-2)-} \cdots Cl^-] \rightarrow Pb^{2+} + x\ I^- + Cl^- \text{ (in DMF)} \quad (2)$$

$$[PbI_x^{(x-2)-} \cdots Cl^-]\text{-} \rightarrow \text{-(Pb-I-Pb-I-}\cdots\text{-Cl-Pb-I)- (framework) (in DMF)} \quad (3)$$

The existence of PbI_2 (320 nm) was not accurately detected due to the near-complete extinction. However, the ion exchange reaction between I and Cl results in the formation of neutral or ionized Pb-I complexes. The slight red shift of PbI_4^{2-} peak may be due to the coordination of Cl into the Pb-I complex and the complete extinction below 430 nm in the mixed-halide solution (compared to the triiodide solution) were observed possibly from the colloidal formation (e.g., soft Pb halogen ion framework), and we hereafter refer them as Pb-halide components (either complex or colloid) [26,27,30]. Various ions and neutral/ionized Pb-halide components penetrate into the porous TiO_2 layer forming the perovskite nanocrystals, as an equilibration between Pb-halide components and DMF shifts to the direction in increasing the concentration of Pb-halide components, resulting in the formation of the perovskite phase with chlorine in it during the annealing process. Any remaining Pb halide components which do not penetrate into the porous TiO_2 react with MAI and finally transform into the perovskite capping layer.

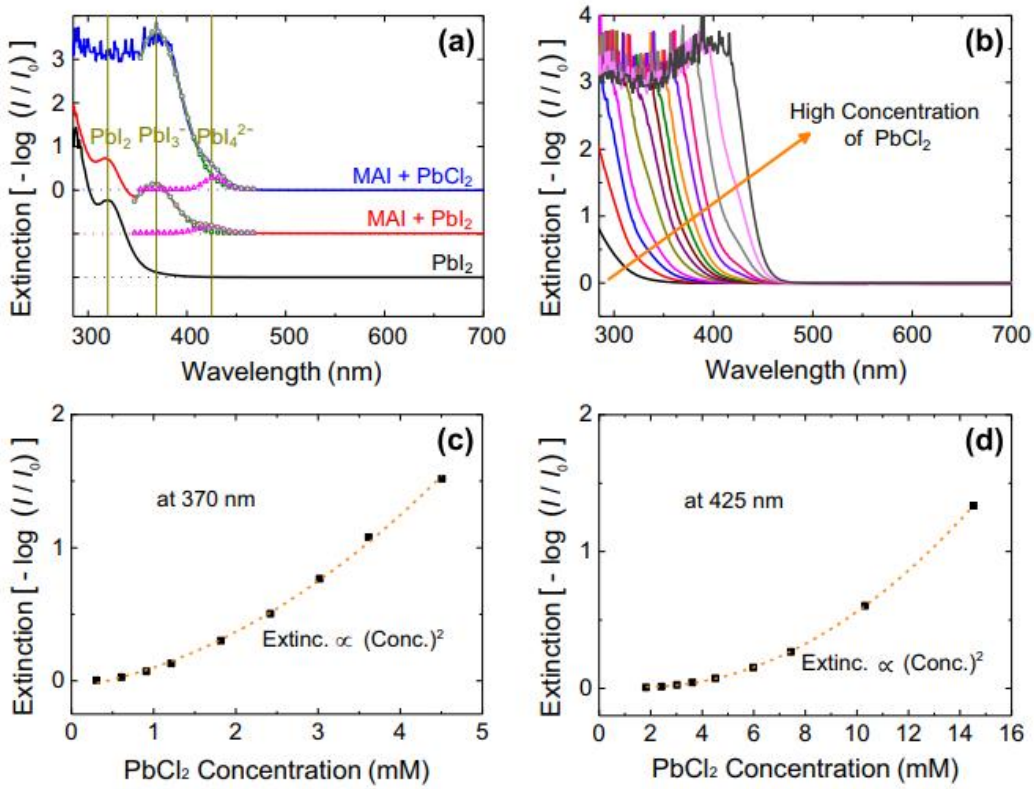

Fig. A1-1. (Color) Extinction spectra of PbI_2, MAI+PbI_2, and MAI+$PbCl_2$ in DMF. (a) PbI_2, MAI+PbI_2 mixture, and MAI+$PbCl_2$ mixture in DMF. The fitting lines are PbI_4^{2-} (pink triangle), PbI_3^- (green square), and the sum of PbI_4^{2-} and PbI_3^- (gray circle). (b) 3:1 molar ratio of MAI:$PbCl_2$ solution with the variation in $PbCl_2$ concentration from 305 μM (left) to 20 mM (right). (c, d) Extinction behavior depending on the $PbCl_2$ concentration (with MAI: $PbCl_2$ = 3:1). (c) Wavelength at 370 nm, corresponding to the absorption of PbI_3^-, and (d) 425 nm corresponding to the absorption of PbI_4^{2-}.

The complete capping layer is essential for the application in the photovoltaic device [9]. Increasing the nucleation sites through the pre-deposition of precursor for the perovskite growth would result in the coverage enhancement with negligible voids. Distinct preparation methods of perovskite films control the crystallization kinetics, and thereby the film nanostructures and morphologies [13,40,41]. The I-terminated PbI_6 octahedrons in the PbI_2 layer form weak van der Waals interactions between iodine and I-terminated PbI_6 octahedrons by iodine-iodine bonding. This interaction between PbI_2 and Pb-halide components in the precursor is expected to assist the coverage improvement, and therefore, the conventional one-step method of dissolving two compounds in one common solvent was slightly modified by the additional PbI_2 coating on the substrate prior to the one-step process. Figure A1-2 shows the effect of the PbI_2 pre-coating on the coverage, and this method clearly enhanced the coverage irrespective of $MAPbI_3(Cl)$ or $MAPbI_3$ film, as expected without any remaining PbI_2 impurity. A noteworthy feature is the film morphology synthesized from the PbI_2 pre-coating and the mixed halide solution. It exhibits distinctive capping-layer comprising large grains (~10 mm) with smaller ones (~1 mm) for the mixed halide perovskite film, as shown in SEM (upper right image in Fig. A1-2). Since the pre-coated PbI_2 evolves easily into the corner shared perovskite structure by the intercalation reaction, the original framework of layer-structured PbI_2 is retained to form $MAPbI_3$ with the additional $MAPbI_3(Cl)$ nanocrystals which are grown from the Pb-halide components in the precursor [42].

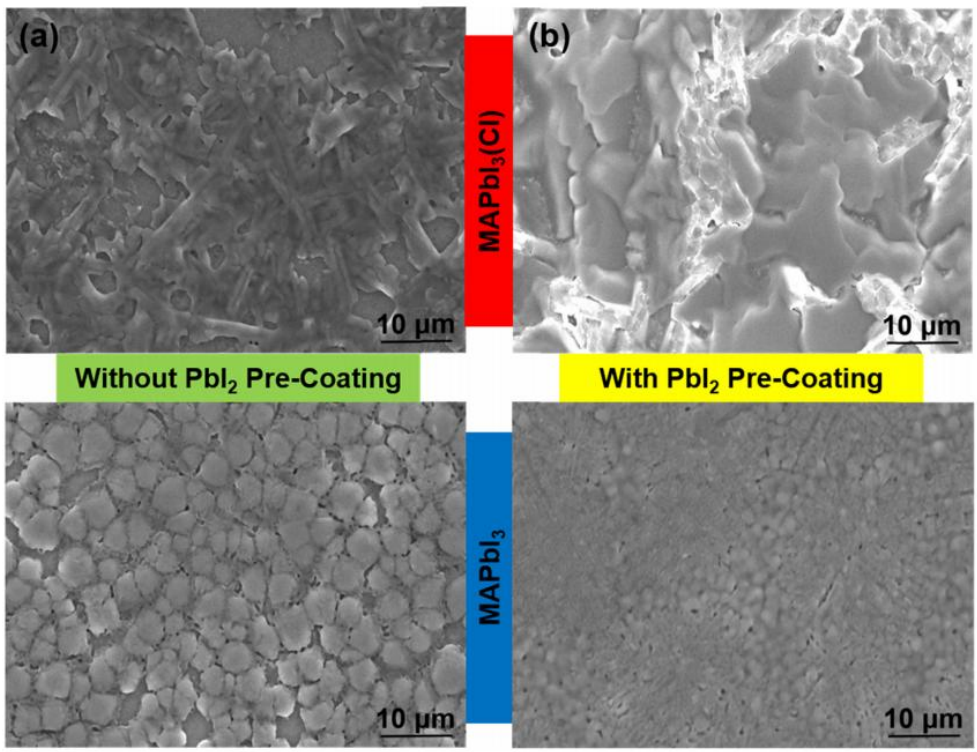

Fig. A1-2. (Color) Microcrystalline evolution of perovskite with the PbI_2 pre-coating method. (a) $CH_3NH_3PbI_3(Cl)$ (top) and $CH_3NH_3PbI_3$ (bottom) perovskite without pre-coating of PbI_2. (b) The perovskite coverage with the pre-coating of PbI_2 layers.

Simple experimental design of annealing-temperature control of the as-deposited precursor film can be used to check the chlorine incorporation in the mixed-halide perovskite (after the complete annealing) since the non-stoichiometric MAI or MACl component in precursor has different sublimation rate at different temperatures [43]. Different amount of excessive MAI or MACl in the precursor evaporates, thus the as-deposited precursor film will develop into microcrystalline grains with differently chlorine amounts. Therefore, x-ray diffraction was further performed to investigate the influences by the annealing-temperature variations. When PbI_2 was not pre-coated, the (110) diffraction peak from $MAPbI_3(Cl)$ shifted by different annealing temperature (Figs. A1-3(a) and (b)), indicating that $MAPbI_3(Cl)$ grain was developed with chlorine in it, which was coincidently observed in the precursor analyses from the slight peak shift in absorption. On the other hand, such diffraction peak shift was negligible for the pre-coating case. By the development of film with blended two-type grains (upper right SEM image in Fig. A1-2, probably $MAPbI_3(Cl)$ and $MAPbI_3$), the peak shift was much reduced. These observations connote that the mixed-halide solution develops $MAPbI_3(Cl)$ with chlorine in its lattice, and the Cl contents vary by different annealing temperature due to the different evaporation rate of MAI and MACl, and the XRF results (Fig. A1-3(c)) support the chlorine incorporation in $MAPbI_3(Cl)$ [25,44–47].

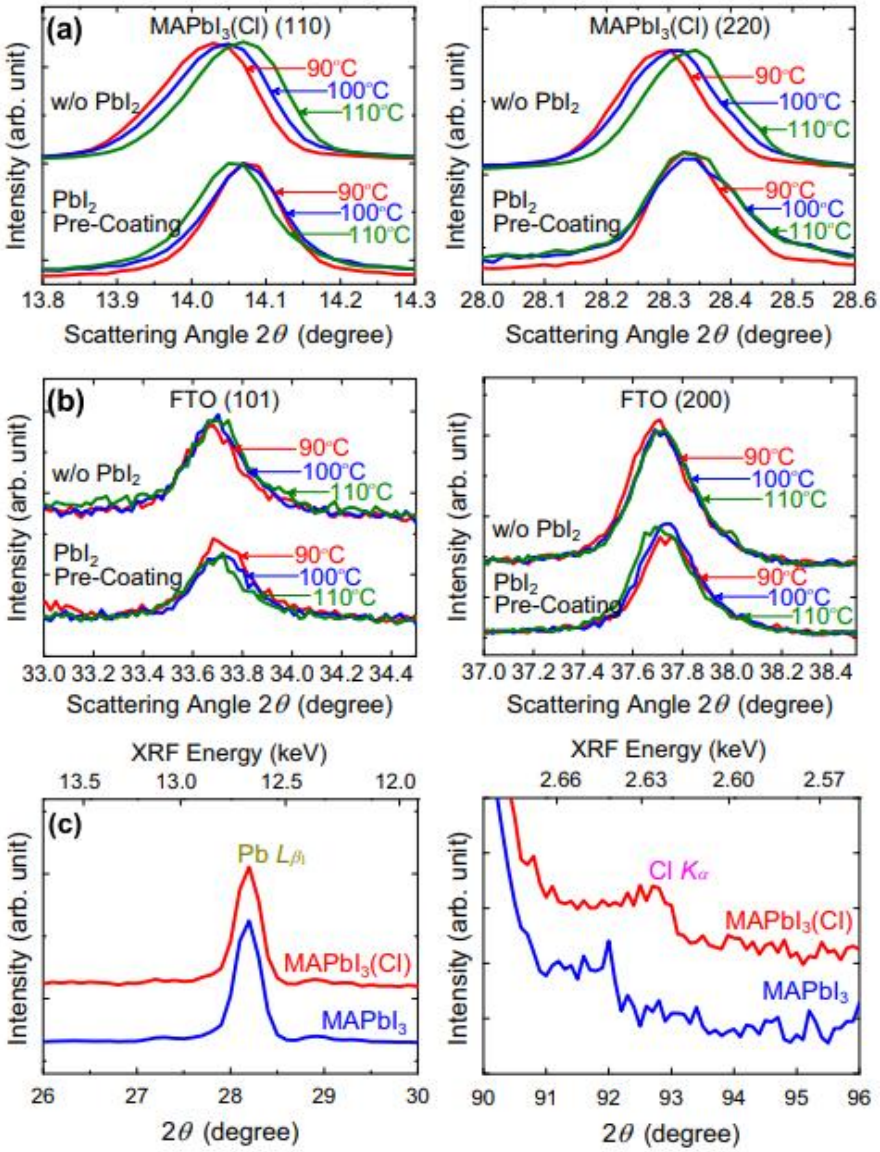

Fig. A1-3. (Color) X-ray diffraction and fluorescence of perovskite. (a) XRD of $MAPbI_3(Cl)$ without PbI_2 pre-coating (top) and with PbI_2 pre-coating (bottom) at different annealing temperatures (from 90°C to 110°C). (b) The reference FTO peak at the identical condition. (c) XRF of Pb and Cl from $MAPbI_3(Cl)$ and $MAPbI_3$ (synthesized with the PbI_2 precoating).

Conductive AFM (*c*AFM) analysis was performed to compare the optoelectronic properties of $MAPbI_3(Cl)$ and $MAPbI_3$. The *c*AFM has been widely used to measure the local photocurrents in various light-harvesting polycrystalline films, and the experimental setup is illustrated in Fig. A1-4. As shown in Figs. A1-4(a) and (b), the photocurrents from $MAPbI_3$ film were uniform from grain to grain (up to 1.36 nA). However, in $MAPbI_3(Cl)$, the photocurrents were inhomogeneously distributed over the film, varying extensively from grain to grain and with the increased average value (maximum up to 60 nA) than the $MAPbI_3$ phase. The origin of inhomogeneous distribution of photocurrents in $MAPbI_3(Cl)$ cannot be attributed to the inhomogeneous distribution of film heights because no distinguishable relationships between photocurrent and film height were observed, as summarized in Fig. A1-5(a). Moreover, photocurrents were compared at similar grains for the validity: no relationships between the grain sizes and photocurrents were observed, as shown in Fig. A1-5(b). Different crystallographic orientation can also be ruled out because of its highly preferred texture of (110) orientation [48].

The large photocurrents from $MAPbI_3(Cl)$ grains can be attributed to its small work function compared to $MAPbI_3$, or the decrease of the defects and consequently the reduced recombination of charge carriers [21,38,49]. To clarify the origin of the recombination decrease, scanning noise microscopy was further utilized to examine the chlorine effect in the perovskite phase [50]. As shown in the noise-spectra comparison between $MAPbI_3(Cl)$ and $MAPbI_3$ grains (Fig. A1-6), current-normalized power spectral density of photocurrent (S/I^2) showed the $1/f$ behavior, and the noise level in $MAPbI_3(Cl)$ was lower compared to that of $MAPbI_3$ [51]. One of the noise sources is the defects causing the fluctuations in the charge carrier density or the mobility [52]. Generation and recombination processes of charge carriers by many traps with distribution of

characteristic lifetimes yield a $1/f$ noise in semiconductors [53]. The mobility scattering by the local electric-field modification around the ionic defects such as vacancies or interstitials can also generate the noise in the current [54]. The grain boundaries have many broken bonds and thereby these may be the major causes of the noise [55]. However, the grain-boundary effect can be excluded in this experiment because the photocurrent was measured at each grain (Fig. A1-4(c)) reflecting the bulk properties, and in addition, the comparison at the grain boundary is obscure since the grain boundary itself affects the electronic properties [35-37]. For the comparison of electronic properties at the grain interior, several measurements were performed at different points, and the reduced noise levels for the mixed-halide perovskite were commonly observed. Relatively broad distribution of noise level was observed for the mixed-halide perovskite, compared with the approximately identical noise levels for triiodide perovskite. The possible cause for the noise reduction in the mixed-halide perovskite is the diminished defects. Decrease of the recombination sites can lead to high optoelectronic responses [47,56-58]. Moreover, non-uniformly distributed chlorine in $MAPbI_3(Cl)$ causes the dispersion of the photocurrents and broad distribution of noise level [25,49]. Theoretical predictions that the Cl doping reduces the electron-hole recombination further support the high optoelectronic responses in $MAPbI_3(Cl)$ [59,60].

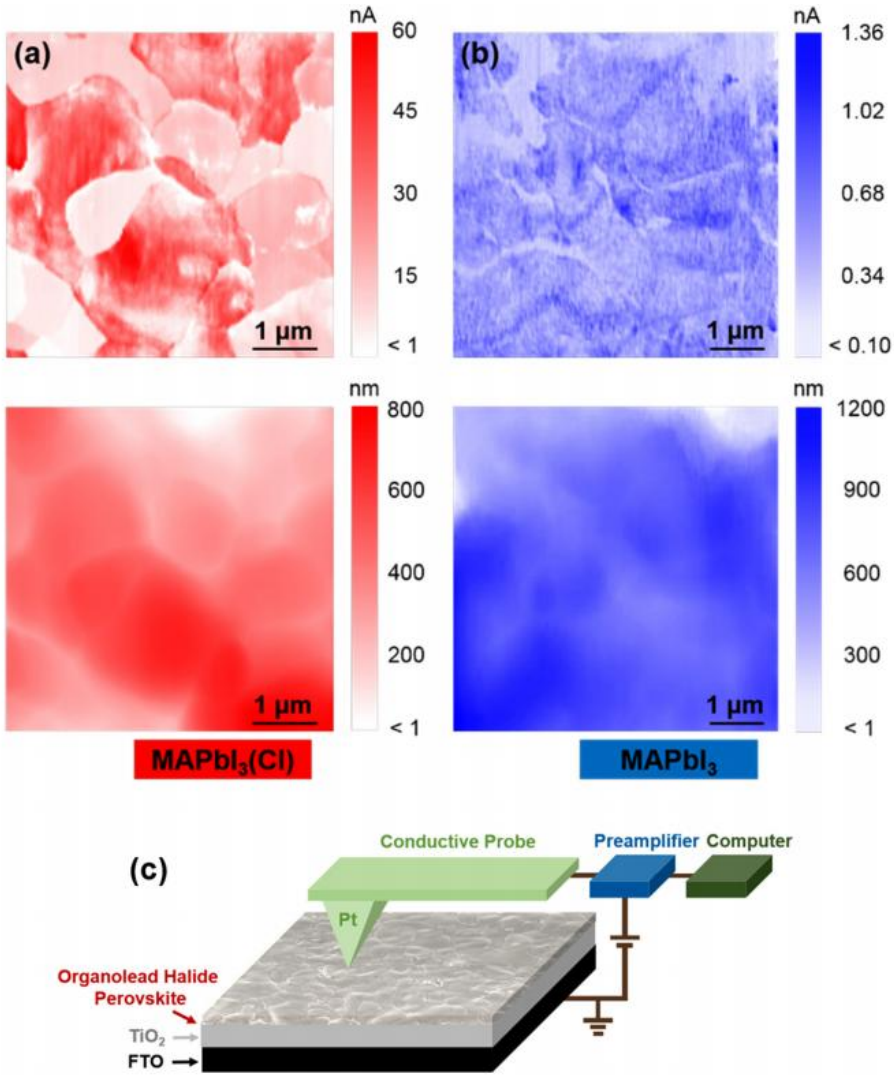

Fig. A1-4. (Color) Photocurrent and topography of $MAPbI_3(Cl)$ or $MAPbI_3$ under 10 mW cm^2 light exposure obtained from the conductive atomic force microscopy (*c*AFM). (a, b) Photocurrent and topography images of $MAPbI_3(Cl)$ and $MAPbI_3$ using the AFM. (c) Experimental setup of *c*AFM for the photocurrent measurement from the polycrystalline perovskite film.

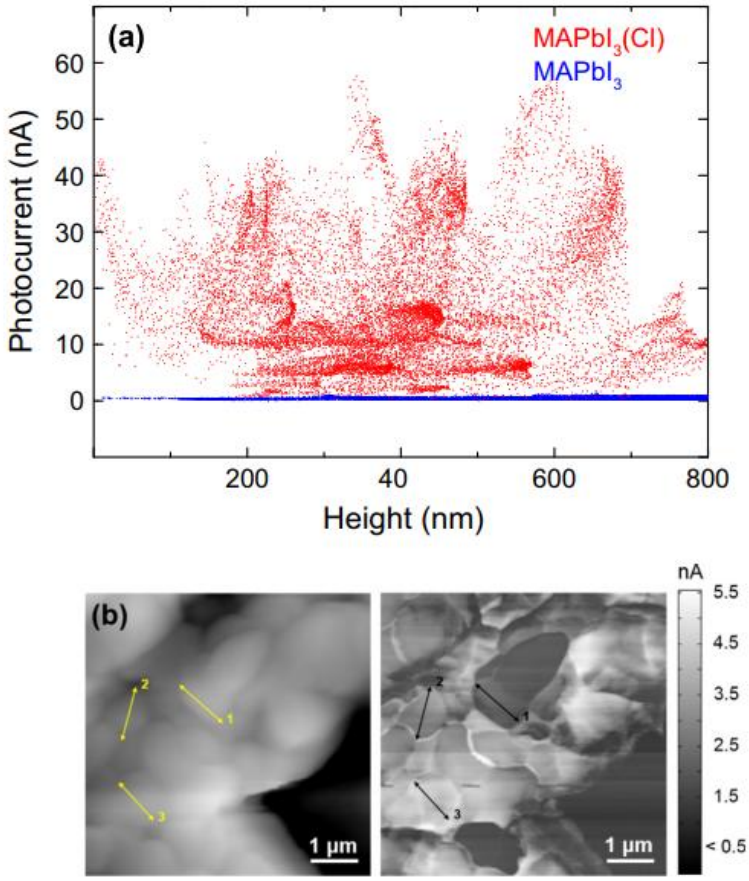

Fig. A1-5. (Color) Photocurrent distribution and the dependence on the film height or grain size of perovskite. (a) Photocurrent distribution on the height of the perovskite film: $MAPbI_3(Cl)$ (red) or $MAPbI_3$ (blue). (b) Photocurrent dependence on the grain size of $MAPbI_3(Cl)$ perovskite. Yellow arrows of 1.2 μm (left image from AFM topography), and the corresponding grains with black arrows (photocurrent from *c*AFM in the right image). Distinctive photocurrents are clear between similar sizes of lateral grains labelling from 1 to 3.

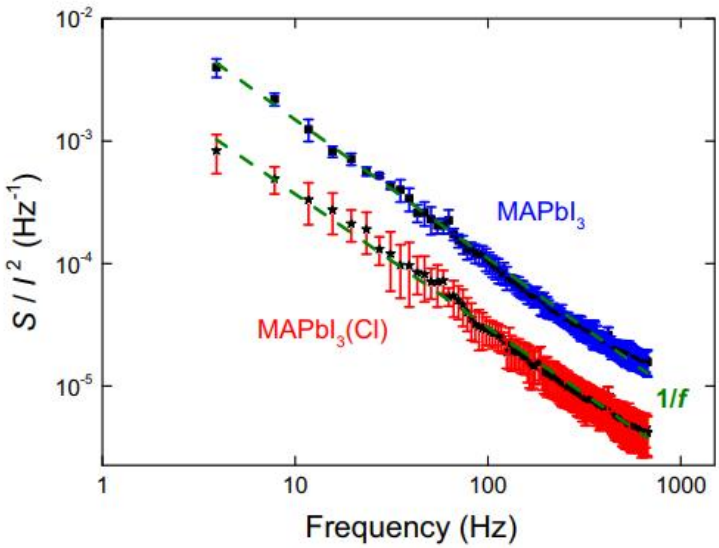

Fig. A1-6. (Color) Current-normalized power spectral density (PSD), compared between $MAPbI_3(Cl)$ (red) and $MAPbI_3$ (blue). Both perovskites from different precursors showed the PSD behavior which was inversely proportional to the frequency (green fitting line) with the low level of the noise for Cl-mediated perovskite. (Measurements were performed at different grains and plotted with the standard deviation.).

A.1.4. Conclusions

In this work, chlorine-mediated $CH_3NH_3PbI_3(Cl)$ grain evolution was explored from the equilibrium shift between lead-halide complex and the solvent in the precursor, and the evidences for the chlorine incorporation in the perovskite phase were further characterized by x-ray fluorescence and diffraction. Experimental observations of the Cl doping in the bulk are expected to lead to the high photocurrents from the reduced electron-hole recombination. Thereby, the optoelectronic properties were compared between $CH_3NH_3PbI_3(Cl)$ and $CH_3NH_3PbI_3$ grains using conductive AFM, and high photocurrents from the $CH_3NH_3PbI_3(Cl)$ grains were observed with non-uniform distribution from grain to grain, which was a different aspect compared to $CH_3NH_3PbI_3$. The origin of high optoelectronic response was additionally discussed, and the photocurrent noise which comes from the defects in the material was analyzed as a straightforward way to identify the recombination reduction in the $CH_3NH_3PbI_3(Cl)$ grains. Combining the microstructural characterizations with *c*AFM and noise analyses, inhomogeneously distributed chlorine in the perovskite was confirmed to diminish the recombination centers resulting high photocurrents. As a future work, photophysical properties with the nanostructures of perovskite will be further characterized.

A.1.5. References

1. M.A. Green, K. Emery, Y. Hishikawa, W. Warta, E.D. Dunlop, *Prog. Photovolt.: Res. Appl.* **23** (2015) 805-812.
2. S. Lee, J.C. Flanagan, J. Kang, J. Kim, M. Shim, B. Park, *Sci. Rep.* **5** (2015) 17472.
3. B. Shin, O. Gunawan, Y. Zhu, N.A. Bojarczuk, S.J. Chey, S. Guha, Prog. Photovolt.
4. V. Tunuguntla, W.-C. Chen, P.-H. Shih, I. Shown, Y.-R. Lin, J.-S. Hwang, C.-H. Lee, L.-C. Chen, K.-H. Chen, *J. Mater. Chem. A* **3** (2015) 15324-15330.
5. H.H. Park, R. Heasley, L. Sun, V. Steinmann, R. Jaramillo, K. Hartman, R. Chakraborty, P. Sinsermsuksakul, D. Chua, T. Buonassisi, R.G. Gordon, *Prog. Photovolt.* **23** (2015) 901-908.
6. N.K. Noel, A. Abate, S.D. Stranks, E.S. Parrott, V.M. Burlakov, A. Goriely, H. J. Snaith, *ACS Nano* **8** (2014) 9815-9821.
7. A. Abate, M. Saliba, D.J. Hollman, S.D. Stranks, K. Wojciechowski, R. Avolio, G. Grancini, A. Petrozza, H.J. Snaith, *Nano Lett.* **14** (2014) 3247-3254.
8. Y. Shao, Z. Xiao, C. Bi, Y. Yuan, J. Huang, *Nat. Commun.* **5** (2014) 5784.
9. N.J. Jeon, J.H. Noh, Y.C. Kim, W.S. Yang, S. Ryu, S.I. Seok, *Nat. Mater.* **13** (2014) 897-903.
10. M.R. Leyden, L.K. Ono, S.R. Raga, Y. Kato, S. Wang, Y. Qi, *J. Mater. Chem. A* **2** (2014) 18742-18745.
11. C. Liu, J. Fan, X. Zhang, Y. Shen, L. Yang, Y. Mai, *ACS Appl. Mater. Interfaces* **7** (2015) 9066-9071.
12. D. Wang, Z. Liu, Z. Zhou, H. Zhu, Y. Zhou, C. Huang, Z. Wang, H. Xu, Y. Jin, B. Fan, S. Pang, G. Cui, *Chem. Mater.* **26** (2014) 7145-7150.

13. Z. Xiao, C. Bi, Y. Shao, Q. Dong, Q. Wang, Y. Yuan, C. Wang, Y. Gao, J. Huang, *Energy Environ. Sci.* **7** (2014) 2619-2623.

14. Y. Ogomi, A. Morita, S. Tsukamoto, T. Saitho, N. Fujikawa, Q. Shen, T. Toyoda, K. Yoshino, S.S. Pandey, T. Ma, S. Hayase, *J. Phys. Chem. Lett.* **5** (2014) 1004-1011.

15. G.E. Eperon, S.D. Stranks, C. Menelaou, M.B. Johnston, L.M. Herz, H.J. Snaith, *Energy Environ. Sci.* **7** (2014) 982-988.

16. F. Hao, C.C. Stoumpos, D.H. Cao, R.P.H. Chang, M.G. Kanatzidis, *Nat. Photonics* **8** (2014) 489-494.

17. A. Mihi, C. Zhang, P.V. Braun, *Angew. Chem.* **123** (2011) 5830-5833.

18. H. Zhou, Q. Chen, G. Li, S. Luo, T.-b. Song, H.-S. Duan, Z. Hong, J. You, Y. Liu, Y. Yang, *Science* **345** (2014) 542-546.

19. Q. Dong, Y. Yuan, Y. Shao, Y. Fang, Q. Wang, J. Huang, *Energy Environ. Sci.* **8** (2015) 2464-2470.

20. Y. Li, W. Sun, W. Yan, S. Ye, H. Peng, Z. Liu, Z. Bian, C. Huang, *Adv. Funct. Mater.* **25** (2015) 4867-4873.

21. W.-J. Yin, H. Chen, T. Shi, S.-H. Wei, Y. Yan, *Adv. Electron. Mater.* **1** (2015) 1500044.

22. E. Mosconi, E. Ronca, F.D. Angelis, *J. Phys. Chem. Lett.* **5** (2014) 2619-2625.

23. V.L. Pool, A. Gold-Parker, M.D. McGehee, M.F. Toney, *Chem. Mater.* **27** (2015) 7240-7243.

24. J.A. McLeod, Z. Wu, B. Sun, L. Liu, *Nanoscale* **8** (2016) 6361-6368.

25. D.E. Starr, G. Sadoughi, E. Handick, R.G. Wilks, J.H. Alsmeier, L. Kohler, M. Gorgoi, H.J. Snaith, M. Bar, *Energy Environ. Sci.* **8** (2015) 1609-1615.

26. K.G. Stamplecoskie, J.S. Mansera, P.V. Kamat, *Energy Environ. Sci.* **8** (2015) 208-

215.

27. K. Yan, M. Long, T. Zhang, Z. Wei, H. Chen, S. Yang, J. Xu, *J. Am. Chem. Soc.* **137** (2015) 4460-4468.

28. Y. Tidhar, E. Edri, H. Weissman, D. Zohar, G. Hodes, D. Cahen, B. Rybtchinski, S. Kirmayer, *J. Am. Chem. Soc.* **136** (2014) 13249-13256.

29. S.T. Williams, F. Zuo, C.-C. Chueh, C.-Y. Liao, P.-W. Liang, A.K.-Y. Jen, *ACS Nano* **8** (2014) 10640-10654.

30. J.J. Gutierrez-Sevillano, S. Ahmad, S. Calero, J.A. Anta, *Phys. Chem. Chem. Phys.* **17** (2015) 22770-22777.

31. C.-S. Jiang, R. Noufi, J.A. AbuShama, K. Ramanathan, H.R. Moutinho, J. Pankow, M.M. Al-Jassim, *Appl. Phys. Lett.* **84** (2004) 3477-3479.

32. J.B. Li, V. Chawla, B.M. Clemens, *Adv. Mater.* **24** (2012) 720-723.

33. I. Visoly-Fisher, S.R. Cohen, A. Ruzin, D. Cahen, *Adv. Mater.* **16** (2004) 879-883.

34. D. Josell, R. Debnath, J.Y. Ha, J. Guyer, M.A. Sahiner, C.J. Reehil, W.A. Manners, N.V. Nguyen, *ACS Appl. Mater. Interfaces* **6** (2014) 15972-15979.

35. J.S. Yun, A. Ho-Baillie, S. Huang, S.H. Woo, Y. Heo, J. Seidel, F. Huang, Y.- B. Cheng, M.A. Green, *J. Phys. Chem. Lett.* **6** (2015) 875-880.

36. J.-J. Li, J.-Y. Ma, Q.-Q. Ge, J.-S. Hu, D. Wang, L.-J. Wan, *ACS Appl. Mater. Interfaces* **7** (2015) 28518-28523.

37. G.Y. Kim, S.H. Oh, B.P. Nguyen, W. Jo, B.J. Kim, D.G. Lee, H.S. Jung, *J. Phys. Chem. Lett.* **6** (2015) 2355-2362.

38. Q. Chen, H. Zhou, Y. Fang, A.Z. Stieg, T.-B. Song, H.-H. Wang, X. Xu, Y. Liu, S. Lu, J. You, P. Sun, J. McKay, M.S. Goorsky, Y. Yang, *Nat. Commun.* **6** (2015) 7269.

39. A. Sengupta, B. Jiang, K.C. Mandal, J.Z. Zhang, *J. Phys. Chem. B* **103** (1999) 3128-

3137.

40. Y. Zhao, K. Zhu, *J. Phys. Chem. C* **118** (2014) 9412-9418.

41. H. Li, S. Li, Y. Wang, H. Sarvari, P. Zhang, M. Wang, Z. Chen, *Sol. Energy* **126** (2016) 243-251.

42. S. Yang, Y.C. Zheng, Y. Hou, X. Chen, Y. Chen, Y. Wang, H. Zhao, H.G. Yang, *Chem. Mater.* **26** (2014) 6705-6710.

43. H. Yu, F. Wang, F. Xie, W. Li, J. Chen, N. Zhao, *Adv. Funct. Mater.* **24** (2014) 7102-7108.

44. J.F. Moulder, W.F. Stickle, P.E. Sobol, K.D. Bomben, Handbook of X-ray Photoelectron Spectroscopy, Perkin-Elmer Corporation,, Waltham, MA, 1992.

45. S. Dharani, H.A. Dewi, R.R. Prabhakar, T. Baikie, C. Shi, D. Yonghua, N. Mathews, P.P. Boix, S.G. Mhaisalkar, *Nanoscale* **6** (2014) 13854-13860.

46. J. You, Z. Hong, Y.M. Yang, Q. Chen, M. Cai, T.-B. Song, C.-C. Chen, S. Lu, Y. Liu, H. Zhou, Y. Yang, *ACS Nano* **8** (2014) 1674-1680.

47. E.L. Unger, A.R. Bowring, C.J. Tassone, V.L. Pool, A. Gold-Parker, R. Cheacharoen, K.H. Stone, E.T. Hoke, M.F. Toney, M.D. McGehee, *Chem. Mater.* **26** (2014) 7158-7165.

48. M. Kawamura, T. Yamada, N. Suyama, A. Yamada, M. Konagai*, Jpn. J. Appl. Phys.* **49** (2010) 052301.

49. D.W. deQuilettes, S.M. Vorpahl, S.D. Stranks, H. Nagaoka, G.E. Eperon, M. E. Ziffer, H.J. Snaith, D.S. Ginger, *Science* **348** (2015) 683-686.

50. M.G. Sung, H. Lee, K. Heo, K.-E. Byun, T. Kim, D.H. Seo, S. Seo, S. Hong, *ACS Nano* **5** (2011) , 8620-8628.

51. R. Dong, Y. Fang, J. Chae, J. Dai, Z. Xiao, Q. Dong, Y. Yuan, A. Centrone, X.C.

Zeng, J. Huang, *Adv. Mater.* **27** (2015) 1912-1918.

52. A.K. Raychaudhuri, *Curr. Opin. Solid State Mater.* **6** (2002) 67-85.
53. F.N. Hooge, *IEEE Trans. Electron Devices* **41** (1994) 1926-1935.
54. J. Pelz, J. Clarke, *Phys. Rev. B* **36** (1987) 4478-4482.
55. A.H. Verbruggen, R.H. Koch, C.P. Umbach, *Phys. Rev. B* **35** (1987) 5864-5867.
56. B. Yang, O. Dyck, J. Poplawsky, J. Keum, A. Puretzky, S. Das, I. Ivanov, C. Rouleau, G. Duscher, D. Geohegan, K. Xiao, *J. Am. Chem. Soc.* **137** (2015) 9210-9213.
57. H. Choi, J. Kim, C. Nahm, C. Kim, S. Nam, J. Kang, B. Lee, T. Hwang, S. Kang, D. J. Choi, Y.-H. Kim, B. Park, *Nano Energy* **2** (2013) 1218-1224.
58. J. Kim, H. Choi, C. Nahm, C. Kim, S. Nam, S. Kang, D.-R. Jung, J.I. Kim, J. Kang, B. Park, *J. Power Sources* **220** (2012) 108-113.
59. J. Liu, O.V. Prezhdo, *J. Phys. Chem. Lett.* **6** (2015) 4463-4469.
60. R. Long, J. Liu, O.V. Prezhdo, *J. Am. Chem. Soc.* **138** (2016) 3884-3890.

Appendix 2. List of Publications and Presentations

A.2.1. Publications (International)

1. **Taehyun Hwang**, Alan Jiwan Yun, Jinhyun Kim, Duckhyung Cho, Sangyeon Kim, Seunghun Hong, and Byungwoo Park,* "Electronic Traps and its Correlations to Perovskite Solar-Cell Performance via Compositional and Thermal-Annealing Controls," *ACS Appl. Mater. Interfaces* (submitted).
2. **Taehyun Hwang**, Byungho Lee, Jinhyun Kim, Alan Jiwan Yun, Bumjin Gil, and Byungwoo Park,* "Electronic Trap Modulation of Perovskite Surface by MACl Post-Treatment for the Efficient Photovoltaic Performance," *Adv. Mater. Interfaces* (submitted).
3. **Taehyun Hwang**,‡ Byungho Lee,‡ Jinhyun Kim,‡ Sangheon Lee,‡ Bumjin Gil, Alan Jiwan Yun, and Byungwoo Park,* "From Nanostructural Evolution to Dynamic Interplay of Constituents: Perspectives for Perovskite Solar Cells," *Adv. Mater.* **30**, 1704208 (2018). [Inside Front Cover]
4. **Taehyun Hwang**,‡ Sangheon Lee,‡ Jinhyun Kim, Jaewon Kim, Chunjoong Kim, Byungha Shin, and Byungwoo Park,* "Tailoring the Mesoscopic TiO_2 Layer: Concomitant Parameters for Enabling High Performance Perovskite Solar Cells," *Nanoscale Res. Lett.* **12**, 57 (2017).
5. **Taehyun Hwang**, Duckhyung Cho, Jinhyun Kim, Jaewon Kim, Sangheon Lee, Byungho Lee, Kyung Hwan Kim, Seunghun Hong, Chunjoong Kim, and Byungwoo Park,* "Investigation of Chlorine-Mediated Microstructural Evolution of $CH_3NH_3PbI_3(Cl)$ Grains for High Optoelectronic Responses," *Nano Energy* **25**, 91 (2016).

6. Byungho Lee, **Taehyun Hwang**, Sangheon Lee, Byungha Shin,* and Byungwoo Park,* "Microstructural Evolution of Hybrid Perovskites Promoted by Chlorine and its Impact on the Performance of Solar Cell," *Sci. Rep.* (submitted).
7. Jinhyun Kim, **Taehyun Hwang**, Byungho Lee, Sangheon Lee, Kimin Park, Helen Hejin Park, and Byungwoo Park,* "An Aromatic Diamine Molecule as the A-Site Solute for Highly Durable and Efficient Perovskite Solar Cells," *Small Methods* 1800361 (2018).
8. Duckhyung Cho, **Taehyun Hwang**, Dong-guk Cho, Byungwoo Park,* and Seunghoon Hong,* "Photoconductive Noise Microscopy Revealing Quantitative Effect of Localized Electronic Traps on the Perovskite-Based Solar Cell Performance," *Nano Energy* **43**, 29 (2018).
9. Sun-Tae Hwang, **Taehyun Hwang**, Sangheon Lee, Bumjin Gil, and Byungwoo Park,* "Selective Rear Contact for $Ga_{0.5}In_{0.5}P$- and GaAs- Based Solar Cells," *Sol. Energ. Mat. Sol. C.* **182**, 348 (2018).
10. Jinhyun Kim, **Taehyun Hwang**, Sangheon Lee, Byungho Lee, Jaewon Kim, Jaewook Kim, Bumjin Gil, and Byungwoo Park,* "Synergetic Effect of Double-Step Blocking Layer for the Perovskite Solar Cell," *J. Appl. Phys.* **122**, 145106 (2017).
11. Jinhyun Kim, **Taehyun Hwang**, Sangheon Lee, Byungho Lee, Jaewon Kim, Gil Su Jang, Seunghoon Nam, and Byungwoo Park,* "Solvent and Intermediate Phase as Boosters for the Perovskite Transformation and Solar Cell Performance," *Sci. Rep.* **6**, 25648 (2016).
12. Woojin Lee, **Taehyun Hwang**, Sangheon Lee, Seung-Yoon Lee, Joonhyeon Kang, Byungho Lee, Jinhyun Kim, Taeho Moon,* and Byungwoo Park,* "Organic-Acid Texturing of Transparent Electrodes Toward Broadband Light Trapping in Thin-Film

Solar Cells," Nano Energy **17**, 180 (2015).

13. Hongsik Choi, **Taehyun Hwang**, Sangheon Lee, Seunghoon Nam, Joonhyeon Kang, Byungho Lee, and Byungwoo Park,* "The Construction of Tandem Dye-Sensitized Solar Cells from Chemically-Derived Nanoporous Photoelectrodes," J. Power Sources **274**, 937 (2015).
14. Seung-Yoon Lee, **Taehyun Hwang**, Woojin Lee, Sangheon Lee, Hongsik Choi, Seh-Won Ahn, Heon-Min Lee, and Byungwoo Park,* "Oxygen-Controlled Seed Layer in DC Sputter-Deposited ZnO:Al Substrate for Si Thin-Film Solar Cells," IEEE J. Photovolt. **5**, 473 (2015).
15. Seung-Yoon Lee, **Taehyun Hwang**, Sangheon Lee, Woojin Lee, Byungho Lee, Jinhyun Kim, Soohyun Kim, Hyun Lee, Heon-Min Lee, and Byungwoo Park,* "Nanoroughness Control of Al-Doped ZnO for High Efficiency Si Thin-Film Solar Cells," Curr. Appl. Phys. **15**, 1353 (2015).
16. Kimin Park,+ Jaewon Kim,+ Sungun Wi,+ Sangheon Lee, **Taehyun Hwang**, Jaewook Kim, Joonhyeon Kang, Jonn-Phil Choi, Seunghoon Nam,* and Byungwoo Park,* "Optimum Morphology of Mixed-Olivine Mesocrystals for Li-Ion Battery," Inorg. Chem. **57**, 5999 (2018).
17. Hyungsub Woo, Sungun Wi, Jaewon Kim, Jinhyun Kim, Sangheon Lee, **Taehyun Hwang**, Joonhyeon Kang, Jaewook Kim, Kimin Park, Bumjin Gil, Seunghoon Nam,* and Byungwoo Park,* "Complementary Surface Modification by Disordered Carbon and Reduced Graphene Oxide on SnO_2 Hollow Spheres as an Anode for Li-Ion Battery," Carbon **129**, 342 (2018).
18. Sangheon Lee,+ Joseph C. Flanagan,+ Byungho Lee, **Taehyun Hwang**, Jaewook Kim, Bumjin Gil, Moonsub Shim,* and Byungwoo Park,* "Route to Improving

Photovoltaics Based on CdSe/$CdSe_xTe_{1-x}$ Type-II Heterojunction Nanorods: The Effect of Morphology and Cosensitization on Carrier Recombination and Transport," *ACS Appl. Mater. Interfaces* **9**, 31931 (2017).

19. Sungun Wi,[+] Jungjin Park,[+] Sangheon Lee, Joonhyeon Kang, **Taehyun Hwang**, Kug-Seung Lee, Han-Koo Lee, Seunghoon Nam, Chunjoong Kim,[*] Yung-Eun Sung,[*] and Byungwoo Park,[*] "Synchrotron-Based X-Ray Absorption Spectroscopy for the Electronic Structure of $Li_xMn_{0.8}Fe_{0.2}PO_4$ Mesocrystal in Li^+ Batteries," *Nano Energy* **31**, 495 (2017).
20. Byungho Lee, Sangheon Lee, Duckhyung Cho, Jinhyun Kim, **Taehyun Hwang**, Kyung Hwan Kim, Seunghun Hong,[*] Taeho Moon,[*] and Byungwoo Park,[*] "Evaluating the Optoelectronic Quality of Hybrid Perovskites by Conductive Atomic Force Microscopy with Noise Spectroscopy," *ACS Appl. Mater. Interfaces* **8**, 30985 (2016).
21. Sun-Tae Hwang, Soohyun Kim, Hyeunseok Cheun, Hyun Lee, Byungho Lee, **Taehyun Hwang**, Sangheon Lee, Wonki Yoon, Heon-Min Lee, and Byungwoo Park,[*] "Bandgap Grading and $Al_{0.3}Ga_{0.7}As$ Heterojunction Emitter for Highly Efficient GaAs-Based Solar Cells," *Sol. Energ. Mat. Sol. C.* **155**, 264 (2016).

22. Woojin Lee, Suji Kang, **Taehyun Hwang**, Kunsu Kim, Hyungsub Woo, Byungho Lee, Jaewon Kim, Jinhyun Kim, and Byungwoo Park,[*] "Facile Conversion Synthesis of Densely-Formed Branched ZnO-Nanowire Arrays for Quantum-Dot-Sensitized Solar Cells," *Electrochim. Acta* **167**, 194 (2015).
23. Yuhong Oh,[+] Seunghoon Nam,[+] Sungun Wi, Joonhyeon Kang, **Taehyun Hwang**, Sangheon Lee, Helen Hejin Park, Jordi Cabana, Chunjoong Kim,[*] and Byungwoo

Park,* "Effective Wrapping of Graphene on Individual $Li_4Ti_5O_{12}$ Grains for High-Rate Li-Ion Batteries," *J. Mater. Chem. A* **2**, 2023 (2014). **[Inside Back Cover]**

24. Jae Ik Kim, Woojin Lee, **Taehyun Hwang**, Jongmin Kim, Seung-Yoon Lee, Suji Kang, Hongsik Choi, Saeromi Hong, Helen Hejin Park, Taeho Moon,* and Byungwoo Park,* "Quantitative Analyses of Damp-Heat-Induced Degradation in Transparent Conducting Oxides," *Sol. Energ. Mat. Sol. C.* **122**, 282 (2014).
25. Byungho Lee,+ Jae Ik Kim,+ Sangheon Lee, **Taehyun Hwang**, Seunghoon Nam, Hongsik Choi, Kunsu Kim, Jaewon Kim, and Byungwoo Park,* "Oriented Hierarchical Porous TiO_2 Nanowires on Ti Substrate: Evolution of Nanostructures for Dye-Sensitized Solar Cells," *Electrochim. Acta* **145**, 231 (2014).
26. Chohui Kim, Hongsik Choi, Jae Ik Kim, Sangheon Lee, Jinhyun Kim, Woojin Lee, **Taehyun Hwang**, Suji Kang, Taeho Moon,* and Byungwoo Park,* "Improving Scattering Layer through Mixture of Nanoporous Spheres and Nanoparticles in ZnO-Based Dye-Sensitized Solar Cells," *Nanoscale Res. Lett.* **9**, 295 (2014).
27. Joonhyeon Kang, Seunghoon Nam, Yuhong Oh, Hongsik Choi, Sungun Wi, Byungho Lee, **Taehyun Hwang**, Saeromi Hong, and Byungwoo Park,* "Electronic Effect in Methanol Dehydrogenation on Pt Surfaces: Potential Control during Methanol Electrooxidation," *J. Phys. Chem. Lett.* **4**, 2931 (2013).
28. Jongmin Kim, Hongsik Choi, Changwoo Nahm, Chohui Kim, Jae Ik Kim, Woojin Lee, Suji Kang, Byungho Lee, **Taehyun Hwang**, Helen Hejin Park, and Byungwoo Park,* "Graded Bandgap Structure for PbS/CdS/ZnS Quantum-Dot-Sensitized Solar Cells with a $Pb_xCd_{1-x}S$ Interlayer," *Appl. Phys. Lett.* **102**, 183901 (2013).
29. Changwoo Nahm, Hongsik Choi, Jongmin Kim, Sujin Byun, Suji Kang, **Taehyun Hwang**, Helen Hejin Park, Jaejung Ko,* and Byungwoo Park,* "A Simple Template-

Free 'Sputtering Deposition and Selective Etching' Process for Nanoporous Thin Films and Its Application to Dye-Sensitized Solar Cells," *Nanotechnology* **24**, 365604 (2013).

30. Hongsik Choi, Jongmin Kim, Changwoo Nahm, Chohui Kim, Seunghoon Nam, Joonhyeon Kang, Byungho Lee, **Taehyun Hwang**, Suji Kang, Dong Joo Choi, Young-Ho Kim,* and Byungwoo Park,* "The Role of ZnO-Coating-Layer Thickness on the Recombination in CdS Quantum-Dot-Sensitized Solar Cells," *Nano Energy* **2**, 1218 (2013).
31. Hongsik Choi, Changwoo Nahm, Jongmin Kim, Chohui Kim, Suji Kang, **Taehyun Hwang**, and Byungwoo Park,* "Review Paper: Toward Highly Efficient Quantum-Dot- and Dye- Sensitized Solar Cells," *Curr. Appl. Phys.* **13**, S2 (2013).
32. Changwoo Nahm,+ Dae-Ryoung Jung,+ Jongmin Kim, Seunghoon Nam, Hongsik Choi, Saeromi Hong, **Taehyun Hwang**, Taeho Moon,* and Byungwoo Park,* "Photoluminescence Enhancement by Surface-Plasmon Resonance: Recombination-Rate Theory and Experiments," *Appl. Phys. Express* **6**, 52001 (2013).
33. Seung-Yoon Lee, Woojin Lee, Changwoo Nahm, Jongmin Kim, Sujin Byun, **Taehyun Hwang**, Byung-Kee Lee, Young Il Jang, Sungeun Lee, Heon-Min Lee, and Byungwoo Park,* "Nanostructural Analysis of ZnO:Al Thin Films for Carrier-Transport Mechanisms," *Curr. Appl. Phys.* **13**, 775 (2013).

A.2.2. Presentations (International)

1. Alan Jiwan Yun,[+] Jinhyun Kim,[+] **Taehyun Hwang**, and Byungwoo Park, "Origins of Efficient Perovskite Solar cells with Low-Temperature Processed SnO_2 Electron Transport Layer," *International Conference on Electronic Materials and Nanotechnology for Green Environment (ENGE2018).* Jeju, Korea, November 12-14, 2018.
2. **Taehyun Hwang**, Byungho Lee, Sangheon Lee, Jinhyun Kim, Bumjin Gil, Alan Jiwan Yun, and Byungwoo Park, "Unraveling the Origins that Enable Efficient Perovskite Solar Cells: Influence of Thermal Annealing via Temporal Evaluation," *Materials Research Society (MRS) Spring Meeting.* Phoenix, AZ, April 2-6, 2018. **[Poster by Taehyun Hwang]**
3. Jinhyun Kim, **Taehyun Hwang**, Byungho Lee, Sangheon Lee, Bumjin Gil, Kimin Park, and Byungwoo Park, "Imidazole as a Cation-Dopant for Stable and Efficient Perovskite Solar Cells," *Materials Research Society (MRS) Spring Meeting.* Phoenix, AZ, April 2-6, 2018.
4. Jinhyun Kim, **Taehyun Hwang**, Sangheon Lee, Byungho Lee, Jaewon Kim, and Byungwoo Park, "Organometallic Perovskite Synthesis for Efficient and Stable Perovskite Solar Cells," *Materials Research Society (MRS) Fall Meeting.* Boston, MA, November 26-December 2, 2016.
5. Jinhyun Kim, **Taehyun Hwang**, Sangheon Lee, Byungho Lee, Jaewon Kim, and Byungwoo Park, "Organometallic Perovskite Synthesis for Efficient and Stable Perovskite Solar Cells," *International Conference on Electronic Materials and Nanotechnology for Green Environment (ENGE2016).* Jeju, Korea, November 6-9,

2016.

6. **Taehyun Hwang**, Duckhyung Cho, Jinhyun Kim, Jaewon Kim, Sangheon Lee, Byungho Lee, Kyung Hwan Kim, Seunghun Hong, and Byungwoo Park, "Investigation of Chlorine-Mediated Microstructural Evolution of $CH_3NH_3PbI_3(Cl)$ for Enabling High Performance Solar Cell," *International Conference on Electronic Materials and Nanotechnology for Green Environment (ENGE2016).* Jeju, Korea, November 6-9, 2016. **[Oral by Taehyun Hwang]**
7. Hongsik Choi, Sangheon Lee, **Taehyun Hwang**, Seunghoon Nam, Joonhyeon Kang, Byungho Lee, and Byungwoo Park, "The Construction of Tandem Dye-Sensitized Solar Cells from Chemically-Derived Nanoporous Photoelectrodes," *Materials Research Society (MRS) Spring Meeting.* San Francisco, CA, April 2015.
8. Woojin Lee, **Taehyun Hwang**, Seung-Yoon Lee, Joonhyeon Kang, Taeho Moon, and Byungwoo Park, "Organic-Acid Texturing of Transparent Electrodes Toward Broadband Light Trapping in Thin-Film Solar Cells," *Materials Research Society (MRS) Spring Meeting.* San Francisco, CA, April 2015.
9. Hongsik Choi, **Taehyun Hwang**, Sangheon Lee, Seunghoon Nam, Joonhyeon Kang, Byungho Lee, and Byungwoo Park, "The Construction of Tandem Dye-Sensitized Solar Cells from Chemically-Derived Nanoporous Photoelectrodes," *International Conference on Electronic Materials and Nanotechnology for Green Environment (ENGE2014).* Jeju, Korea, November 16-19, 2014.
10. Woojin Lee, **Taehyun Hwang**, Seung-Yoon Lee, Joonhyeon Kang, Taeho Moon, and Byungwoo Park, "Organic-Acid Texturing of Transparent Electrodes Toward Broadband Light Trapping in Thin-Film Solar Cells," *International Conference on Electronic Materials and Nanotechnology for Green Environment (ENGE2014).* Jeju,

Korea, November 16-19, 2014.

11. Byungho Lee, Jae Ik Kim, Sangheon Lee, **Taehyun Hwang**, Seunghoon Nam, Kunsu Kim, Jaewon Kim, and Byungwoo Park, "Oriented Hierarchical Porous TiO_2 Nanowires on Ti Substrate: Evolution of Nanostructures for Dye-Sensitized Solar Cells," *International Conference on Electronic Materials and Nanotechnology for Green Environment (ENGE2014).* Jeju, Korea, November 16-19, 2014.
12. Hongsik Choi, Changwoo Nahm, Seunghoon Nam, Byungho Lee, **Taehyun Hwang**, Sangheon Lee, and Byungwoo Park, "Nanoporous NiO Thin Films Prepared by Selective Etching for the *p*-Type Dye-Sensitized Solar Cells," *Materials Research Society (MRS) Fall Meeting.* Boston, MA, December 2013.
13. Seunghoon Nam, Sungun Wi, Yuhong Oh, Saeromi Hong, Hyungsub Woo, Jaewon Kim, Sangheon Lee, **Taehyun Hwang**, Hongsik Choi, and Byungwoo Park, "Porous Graphene as a Smart Strategy for Wrapping SnO_2," *Materials Research Society (MRS) Fall Meeting.* Boston, MA, December 2013.
14. Jae Ik Kim, Woojin Lee, **Taehyun Hwang**, Seung-Yoon Lee, Suji Kang, Hongsik Choi, Saeromi Hong, Taeho Moon, and Byungwoo Park, "Quantitative Understanding of Damp-Heat-Induced Degradation in Transparent Conducting Oxides," *Materials Research Society (MRS) Fall Meeting.* Boston, MA, December 2013.
15. Yuhong Oh, Seunghoon Nam, Sungun Wi, Joonhyeon Kang, **Taehyun Hwang**, Sangheon Lee, Jordi Cabana, Chunjoong Kim, and Byungwoo Park, "Inexpensive Wrapping of Graphene on Individual $Li_4Ti_5O_{12}$ Grains for Superior-Rate Li-Ion Batteries," *Materials Research Society (MRS) Fall Meeting.* Boston, MA, December 2013.
16. Yuhong Oh, Seunghoon Nam, Sungun Wi, Joonhyeon Kang, **Taehyun Hwang**,

Sangheon Lee, and Byungwoo Park, "Inexpensive Wrapping of Graphene on Individual $Li_4Ti_5O_{12}$ Grains for Superior-Rate Li-Ion Batteries," *The 9th Tsinghua University - University of Tokyo - Seoul National University Student Workshop.* Seoul, Korea, October 9-12, 2013.

17. Jae Ik Kim, Woojin Lee, Jongmin Kim, Seung-Yoon Lee, Suji Kang, **Taehyun Hwang**, Taeho Moon, and Byungwoo Park, "The Stability and Degradation Mechanisms of ZnO:Al Thin Films in Damp-Heat Environment, *The 13th Korea - Japan Student Symposium (Seoul National University - Tohoku University).* Seoul, Korea, November 7-9, 2012.

국문초록

현대사회에서 전기에너지 수요는 급증하고 있지만 그 공급은 천연가스, 원자력 에너지, 화석 연료 및 원유 등에 의존하고 있다. 그 결과 온실가스 배출 및 방사성 폐기물 등 부차적인 문제가 지구 온난화, 오염, 기후변화, 그리고 사회 갈등의 문제 등을 야기하고 있다. 한정된 자원의 효율적 이용 및 후속 세대를 위한 책임있는 에너지 사용을 위해 새로운 에너지원에 대한 관심이 늘어나고 있으며, 그 중 지속가능하고 친환경적인 에너지원의 수요 및 이의 이용이 증가하고 있다. 태양에너지는 태양열/태양광 발전, 광촉매를 이용한 화합물의 생산 등 다양한 에너지변환소자에 이용될 수 있다는 측면에서 각광받고 있으며, 그 중 태양광을 이용한 발전량을 증대시키기 위해 다양한 정책논의가 이루어지고 있다. 태양전지는 태양광 발전소자로서 흡수한 광자를 통해 생성된 전하로부터 전기를 생산한다. 빛 에너지 조사면적에 비례하여 발전량이 늘어난다는 특징을 가지며, 낮은 생산비용 및 값싼 재료로부터 높은 광전변환효율을 실현하는 것이 효율적인 이용의 핵심이겠다.

태양전지에 적용될 수 있는 물질 중 최근에 높은 주목을 받은 것들 중 하나는 유-무기 하이브리드 납-할라이드 페로브스카이트이다 (이하 하이브리드 페로브스카이트). 하이브리드 페로브스카이트는 높은 광흡수계수, 자유 전하의 생성, 높은 전하이동도 및 낮은 전하재결합 등 태양전지로 이용하기에 적합한 우수한 광물리적 성질을 가지고 있다. 또한 기존의 박막 태양전지와는 달리 용액공정으로 고품질 박막 및 고성능 태양전지 제조가 가능하며, 전구체 용액을 조절하여 미세구조의 제어가 용이하다는 점은 광학, 전기, 광전기적 성질 제어를 통해 태양전지 외의 다양한 반도체 및

발광소자로의 응용을 실현한다. 이상의 소자들을 실생활에 적용하기 위해서는 해결해야 할 이슈들이 산적해 있으며, 그 중 대표적인 것은 페로브스카이트의 분해 및 불안정성이다. 하이브리드 페로브스카이트의 유기물 분자는 대기 중의 수분과 결합할 수 있고 대기 중의 산소분자는 페로브스카이트의 격자결함자리에 위치하여 물질 분해반응을 촉진할 수 있으며, 결국 태양전지 초기성능의 급격한 감소를 일으키게 된다. 소자의 완벽한 봉지화를 통해 외부입자의 확산을 억제하더라도 빛에 의한 불안정성이 존재하며, 공통적으로 지목되고 있는 요인은 페로브스카이트 내부에 존재하는 격자 및 전기적 결함으로 외부 산소 및 수분과의 상호작용을 통해 분해반응을 일으킨다는 여러 메커니즘이 제시되고 있다. 이러한 사실은 페로브스카이트의 미세구조, 더 나아가 격자 레벨에서 결함 제어를 요구하게 된다. 즉, 페로브스카이트의 구조적/전기적 결함에 대한 깊이 있는 이해를 통해 효율향상 전략을 수립할 수 있으며, 결정화 및 공정의 제어가 결함에 미치는 영향을 분석함으로써 효율적인 미세구조 및 결함특성의 제어를 실현할 수 있고 이를 토대로 효율적인 태양전지 제작이 가능해질 것이다.

1 장에서는 태양전지의 작동원리 및 하이브리드 페로브스카이트에 대해 간단히 소개하고, 태양전지의 광전변환효율을 향상시키기 위한 페로브스카이트 미세구조 및 격자결함 제어에 관해 보고된 효과적인 전략들에 대해 살펴보았다. 페로브스카이트의 분해 및 불안정성에 있어 미세구조 및 결함이 관여하는 반응을 이해함으로써 페로브스카이트의 결정화 및 결정립 성장, 구조적 결함 감소의 중요성, 그리고 불안정성을 극복하기 위한 다양한 해결책을 제시할 수 있었다.

2 장에서는 페로브스카이트의 조성 및 결정화를 위한 열처리 조건의 차이가 박막 및 계면에서의 광전하 이동 및 재결합에 미치는 영향에 대해 분석을 진행, 태양전지의 특성향상을 위하여 페로브스카이트 조성별 차별화된 전략을 제시하였다. 가장 간단한 조성의 페로브스카이트 (이하 $MAPbI_3$)와 비슷한 밴드갭 에너지, 결정립 크기, 그리고 박막의 형상을 가져 유사한 태양전지 특성을 보일 것으로 기대되는 다중 원소가 혼합된 페로브스카이트 (이하 $(FA_{0.83}MA_{0.17})Pb(I_{0.83}Br_{0.17})_3$ 및 $(Cs_{0.10}FA_{0.75}MA_{0.15})Pb(I_{0.85}Br_{0.15})_3$) 로 태양전지를 제작하여 이들 사이의 비교분석을 실시하였다. 그 결과 세슘 및 복합 양이온/음이온으로 구성된 조성의 페로브스카이트가 타 조성 페로브스카이트에 비하여 높은 광전류와 낮은 전류의 노이즈를 보였으며, 노이즈에 대한 물리적 모델을 적용한 결과 복합 조성을 가지는 페로브스카이트 박막은 전기적 트랩의 농도가 낮았고 이는 더 높은 태양전지 개방전압을 뒷받침하였다. 또한 태양전지의 전기용량이 전기적 트랩의 에너지레벨 및 주파수로 결정된다는 이론적 모델을 적용하여 분석한 결과, 시간에 따른 태양전지의 특성변화와 전기적 트랩사이의 상관관계를 밝힐 수 있었다. 수 주의 시간이 지난 후에도 결정구조, 박막의 형상, 표면 조성이 초기 페로브스카이트 박막과 다르지 않았고 분해의 흔적인 불순물이 형성되지 않았다는 점은 점 결함 등 구조적 결함에서 기인하는 전기적 트랩이 태양전지 특성 변화의 원인일 수 있음을 뒷받침하였다. 그 결과 추가적인 태양전지 특성의 향상을 위해 결함형성의 억제를 통한 전기적 결함의 농도를 줄이는 것이 효과적임을 제시할 수 있었고, 계면에서의 효과적인 전하 추출의 필요성에 대해 뒷받침할 수 있었다.

3 장에서는 후처리 공정을 적용하여 페로브스카이트 박막의 표면 결함 농도를 줄이고 계면 특성의 향상을 도모하여 태양전지 성능향상을 실현하였다. 하이브리드 페로브스카이트가 극성의 유기분자를 포함하고 있다는 점과 이온 결합성을 가진다는 점은 극성 용매를 이용한 후처리 공정이 물질의 분해를 비롯한 결함 형성 등의 악영향을 미칠 수 있다는 점을 내포하였다. 이는 후처리 공정에 대한 안정성 확보를 요구하였으며, 이에 페로브스카이트 박막의 조성 및 미세구조 제어의 필요성이 강조되었다. 다중 원소로 혼합된 격자 결함이 적은 페로브스카이트의 조성이 후처리 공정 결과 박막 표면 및 계면에 있는 전기적 트랩을 효율적으로 줄일 수 있었고, 태양전지의 광전변환 효율향상을 실현할 수 있었다. 그 결과, 화학반응에 대해 강한 내구성을 가진 페로브스카이트가 높은 효율과 더불어 안정적인 성능을 보일 것으로 기대되었다.

주요어: 태양전지, 유-무기 복합 납-할라이드 페로브스카이트, 결정화, 용액 공정, 조성 제어, 후처리 공정, 결함 패시베이션, 전기적 트랩, 1/*f* 노이즈, 전기용량, 전하 재결합

학번: 2012-23934

감사의 글

대학원에 입학한 그 순간부터 지금 이 순간까지 지난 시간들이 주마등처럼 머릿속을 스쳐 지나갑니다. 학업, 연구, 프로젝트 및 연구실 업무 등 대학원 생활 동안 참 많은 일들이 있었습니다. 모든 일들이 새롭고 시행착오도 많이 있었습니다. 대학원 과정이 학업과 연구에 대한 치열한 고민의 시간이기도 했고, 연구를 비롯한 모든 것이 저에게는 도전이었고 힘든 순간도 많이 있었습니다만, 포기하지 않고 최선을 다한 것이 적어도 지금 이순간 보람을 느끼게 하지 않나 자평해 봅니다. 이는 저 혼자만의 힘이 아닌 교수님, 그리고 항상 제 옆에 있었던 연구실 선후배 동료들의 격려와 도움이 있었기에 가능했습니다. 이 글을 통해 짧게나마 감사의 표현을 전달하고자 합니다.

먼저 박사학위과정 동안 저를 지도해주신 박병우 교수님께 진심으로 감사드립니다. 연구실 생활 동안 교수님께서 조언해주신 하나하나 가슴에 새겨 연구자, 그리고 더 나아가 인생을 개척하는데에 있어 길라잡이로 삼도록 하겠습니다. 감사합니다.

선뜻 저의 학위심사를 허락해 주신 김진영 교수님께 진심으로 감사드립니다. 태양전지에 관한 교수님의 조언을 통해 제가 부족한 점과 더 나아가야 할 방향에 대해 고민해볼 수 있었습니다. 김상범 교수님께도 진심으로 감사의 말씀을 드립니다. 다양한 분야에 대한 교수님의 조언을 통해 연구에 대해 깊고 넓게 고찰해볼 수 있었습니다. 정현석 교수님께도 진심으로 감사의 말씀을 드립니다. 태양전지에 관한 교수님의 다양한 논문을 읽고 많은 깨달음을 얻을 수 있었고 연구 방향에 대해 고민해볼 수 있었습니다. 교수님을 박사학위 심사위원으로 모실 수 있어서 정말 감사했습니다. 문태호 교수님께도 진심으로

감사의 말씀을 드립니다. 교수님의 조언이 있었기에 새로운 분야에 도전할 수 있었고 그 열매를 맺을 수 있었습니다. 연구 외적으로도 교수님께서 해주신 조언을 가슴에 새기고 힘들 때마다 꺼내어 되새기고자 합니다. 김천중 교수님께도 진심으로 감사의 말씀을 드립니다. 재료공학에 있어 교수님의 다양한 경험과 지식에 항상 놀라고 재미있었으며 본받고 싶다는 생각을 많이 하였습니다. 앞으로도 교수님께 연구 뿐만이 아니라 다양한 분야에 대해서 조언을 구하겠습니다. 신병하 교수님 및 홍승훈 교수님께도 감사의 말씀을 드립니다. 다양한 분야에 대한 교수님의 조언을 통해 연구를 수행할 수 있었습니다. 진심어린 조언을 해주신 여러 교수님들께 다시 한번 감사의 말씀을 드립니다.

연구실 선배님과 후배님들에게도 감사의 말씀을 드리고 싶습니다. 처음 연구실에 들어와서 어색해할 때 유홍이형, 종민이형, 재익이형, 성언이형, 홍식이형이 퇴근 후 술 한잔 사주시며 많은 이야기를 해주며 챙겨주셨던 것이 연구실에 재미있게 적응할 수 있었던 것 같습니다. 승훈이형, 우진이형, 준현이형 등 형들과 함께 했던 축구경기는 비록 많이 이기지는 못했지만 공격이든 수비든 항상 든든했습니다. 카리스마 넘치지만 항상 친절하게 설명해주신 창우형, 진심 어린 조언을 아끼지 않으셨던 성준이형, 항상 밝은 긍정의 기운을 주신 초희누나, 열정을 느낄 수 있었던 수진누나, 동갑이라 어색했지만 그래도 나름 친했던 수지랑 새로미, 격려의 말을 많이 해주셨던 승윤이형과 정진이형, 가끔 재미있는 선태형 모두 감사드립니다. 가장 오랜 시간 함께한 병호는 비범한 그 능력이 그리울 것 같고, 덕후로서 모르는 게 없던 상헌이는 이제 개그감만 정복하면 될 것 같아. 지난 과거는 잊고 이제는 꽃길만 걸어야 할 형섭이, 카리스마 넘치면서도 부드러운 남자 재원이형, 연구와 패션 등 두

루두루 센스가 돋보이는 퍼듀 넘버원 진현이, 나가더니 꽃미남으로 돌아온 복기, 시작하면 끝을 보는 상남자 경환이, 중저음이 매력적이고 스웩 넘치는 국한이, 개그 빼고 모르는게 없는 재욱이, 방장으로서 책임감이 느껴지지만 (호)불호 확실한 매력을 가진 기민, 앞으로 연구실을 이끌어 나가야 할 범진이, 지완이, 영현이, 그리고 인턴으로 있었던 힘쎈 정훈이, 정연희, 최제, 박재성, 안수빈, 손미나 등 모두에게 감사의 말씀을 드리며 같이 지낼 수 있어 연구실에서 추억 한 줄이 더 늘어날 수 있었습니다. 연구에 있어 많은 도움을 주신 덕형씨와 대학원 생활 동안 많은 의지가 되었던 재형이형 에게도 진심으로 감사의 말을 전합니다. 제가 받은 것 이상으로 돌려줄 수 있는 사람이 되도록 하겠습니다.

어린시절부터 언제나 힘이 되어 준 승진, 형진, 승현 우리 패밀리에게도 고마움을 전합니다. 특히 승진이에게는 특별한 인연을 선물해준 은혜를 못할 것이고, 행복하게 사는 모습이 너무 보기 좋다는 생각을 여기 적어봅니다. 항상 우리를 반갑게 맞이해준 나연이에게도 고맙다는 말을 같이 적어봅니다. 차기 은행장과 금융계 수장이 되어야 할 병식이와 대현이, 토론하다 싸우기도 하고 또 술한잔에 풀어지기도 하고 앞으로도 지금처럼 잘 싸우고 화해하고 재밌게 살자. 자수성가 사업가로 명성을 떨칠 지용이는 앞으로 잘 부탁하고, 광고계의 대부를 꿈꾸는 배돌이 성준이도 항상 응원한다. 서로 치고받고 하더라도 지금처럼 서로에게 힘이되고 힘든 시간 같이 이겨냈던 것처럼 앞으로로 잘 해봅시다. 항상 내 정신적 지주가 되어준 천재 진록이, 엔지니어를 뛰어넘어 진정한 인생의 가치를 찾아갈 우철이, 전공은 다르지만 동고동락 고민을 다 털어놓고 얘기할 수 있어 정말 큰 힘이 된 김쌍, 현썩, 깜동, 그리고 같은 길

을 걷는 신영이, 언제 만나더라도 즐겁고 힘이 되는 태규, 승엽, 은길, 인택, 규빈, 승민, 교원 6반 친구들이랑 이제 곧 아줌마가 될 윤지, 소정, 그리고 친구지만 존경스럽고 항상 도전정신이 넘치는 재우 등 소중한 친구들이 있어 힘이 되었습니다. 친구들 모두에게 고맙다는 말을 남기고 싶습니다.

마지막으로 항상 저를 믿고 사랑을 주신 부모님과 형, 가족들이 없었다면 지금의 제가 있을 수 없었습니다. 힘든 일이 있더라도 좌절하지 않고 최선을 다해 열심히 사는 모습 보여드려 감사함에 보답할 수 있는 아들이 되겠습니다. 앞으로도 우리 가족 모두 지금처럼 행복할 수 있도록 더 많이 사랑하고 또한 부모님께서 보여주신 지혜를 본받으며 살아가겠습니다. 존경하고 사랑합니다.

제 곁에 항상 있어준 사랑하는 김지인 양에게 진심 어린 고마움을 전하며 글을 마치겠습니다. 앞으로 함께 갈 길에 있어 항상 응원하고 사랑하겠습니다.

2019 년 1월

황태현 올림